Winter 1994

Characterization of radical formation and iron oxidation/ hydrolysis during iron deposition in ferritin

Yu Chen Barrett
University of New Hampshire, Durham

Order Number 9518476

Characterization of radical formation and iron oxidation/hydrolysis during iron deposition in ferritin

Barrett, Yu Chen, Ph.D.

University of New Hampshire, 1994

U·M·I
300 N. Zeeb Rd.
Ann Arbor, MI 48106

CHARACTERIZATION OF RADICAL FORMATION AND IRON OXIDATION/HYDROLYSIS DURING IRON DEPOSITION IN FERRITIN

BY

YU CHEN BARRETT
B.S., Beijing Polytechnic Institute, 1986
M.S., University of New Hampshire, 1989

DISSERTATION

Submitted to the University of New Hampshire
in Partial Fulfillment of
the Requirements for the Degree of

Doctor of Philosophy

in

Chemistry

December, 1994

This dissertation has been examined and approved.

N. Dennis Chasteen

Dissertation director, N. Dennis Chasteen
Professor of Chemistry

Sterling A. Tomellini,
Associate Professor of Chemistry

Christopher F. Bauer,
Associate Professor of Chemistry

Kenneth K. Andersen, Professor of Chemistry

Thomas M. Laue,
Associate Professor of Biochemistry

November 16, 1994

Date

DEDICATION

This dissertation is dedicated to my parents, Chengquan Chen and Rongjing Ma and my husband, James J. Chen Barrett.

ACKNOWLEDGEMENTS

I would like to express my sincere appreciation to my dissertation advisor, Professor N. D. Chasteen for his guidance, support and many helpful discussions throughout the years and his patience in the preparation of this dissertation. I would like to thank Drs. Pauline Harrison, Amyra Treffry, Paolo Arosio and Paolo Santambrogio for providing various ferritin mutants for this dissertation work. I owe my thanks to Mr. Robert Curry for assistance in interfacing the oxygen electrode to a PC and Mr. Robert Champlain for machining the reaction cell used in the kinetic study. I also like to acknowledge NIH grant R37 GM20194 for financially supporting my research.

I would also like to thank John Grady and Stephen Hattan for their friendship and valuable help during my stay at UNH. Special thanks go to my parents, Chengquan Chen and Rongjing Ma, my brothers, Lin Chen and Rong Chen for their love and support throughout the years. Above all, my deepest appreciation is for my husband James J. C. Barrett. His consistent love, understanding and encouragement are the inspiration of this work.

TABLE OF CONTENTS

LIST OF FIGURES

LIST OF TABLE

ABBREVIATIONS

BES	N,N-bis-(Hydroxyethyl)-2-aminoethane sulfonic acid
EDTA	ethylendiamine tetraacetate acid, disodium salt
epr	electron spin resonance
FTN	E-coli ferritin (conventional type)
HEPES	4-(2-hydroxyethyl)-1-piperazineethanesulfonic acid
HoSF	horse spleen ferritin
HoLF	recombinant horse L-chain ferritin
HuHF (rHF)	recombinant human H-chain ferritin
HuLF (rLF)	recombinant human L-chain ferritin
MES	2-(N-morpholino)ethanesulfonic acid
MOPS	3-(N-morpholino)propanesulfonic acid
NTA	nitrilotriacetate
PAGE	polyacrylamide gel electrophoresis
PBN	α-phenyl-N-t-butyl nitrone
SDS	sodium dodecyl sulfate
S-13	HuHF with the tryptophan mutated (K86Q, W93F)
TGA	thioglycolic acid
222	HuHF with the ferroxidase site mutated (E27A, E62K, H65G)

ABSTRACT

CHARACTERIZATION OF RADICAL FORMATION AND IRON OXIDATION/ HYDROLYSIS DURING IRON DEPOSITION IN FERRITIN

by

Yu Chen Barrett
University of New Hampshire, December, 1994

The functional roles of ferritin H and L subunits in ferrous iron oxidation and ferric iron hydrolytic polymerization were studied by combination of electrode oximetry and pH stat utilizing horse spleen and recombinant human H and L ferritins. Previous work has investigated ferrous ion oxidation kinetics, but no information on ferric core formation and its relationship to ferrous ion oxidation had been obtained. The kinetic pattern of iron oxidation/hydrolysis in H-chain homopolymer ferritin showed that the rate of iron hydrolysis is regulated by the rate of iron oxidation, and that both follow the iron ferroxidation pathway. In the early stage of the reaction with less than 10 Fe(II)/protein, it was observed that the stoichiometric ratio of proton release to ferrous iron consumption approaches zero, the ferrous iron to dioxygen ratio equals two and the kinetic ratio of proton release to dioxygen consumption approaches one. These results enable one to write a detailed mechanism for iron ferroxidation occurring in ferritins containing the

H-subunit. The L-chain homopolymer ferritin was also shown to facilitate iron oxidation, but iron deposition occurs by a mineral core surface mechanism as evidenced by the kinetic ratio of eight protons released per dioxygen consumed. These results suggest that the H-subunit serves as a ferrous iron oxidation source and the L-subunit acts as a ferric iron sink during iron incorporation into native heteropolymer ferritins.

Two types of ferritin radicals were observed by epr spectroscopy. One radical is a tyrosyl radical formed in the H-subunit only and is possibly generated from a superoxide intermediate produced during the one electron oxidation of iron(II). This radical gives a characteristic tyrosyl radical doublet with a g-factor of 2.0066 and a hyperfine splitting of 18 G. This radical is centered on a Tyr-34 as shown by measurements with site directed mutants. The other type of ferritin radical produced is a secondary radical derived from hydroxyl radical attack on ferritin. This radical is possibly formed on an iron binding site of the L-subunit. Neither of these ferritin radicals play an important role in iron ferroxidation. However, confinement of radical production to the inside of the ferritin shell could be a protective mechanism against iron toxicity.

CHAPTER I

INTRODUCTION

Iron and Ferritin

Iron, the second most common element in the Earth's crust, is involved in many important biological processes such as transporting, storing and activating molecular oxygen (Fontecave & Pierre, 1993; Crichton & Ward, 1992) and the growth of almost all living organisms (Theil, 1987). However, the soluble, hence bioavailable, form of iron, ferrous iron, is very reactive towards atmospheric oxygen. These reactions produce harmful oxygen radicals such as superoxide and hydroxyl radicals as well as insoluble and bioinaccessible ferric iron in the form of oxides and hydroxides (K_{sp} for $Fe(OH)_3 = 10^{-37}$, [Fe(III)] at pH 7 = 10^{-16} M) (Spiro & Saltman, 1969; Theil, 1987; Fontecave & Pierre, 1993). Thus, living organisms have developed two mechanisms against this reactivity. One mechanism is a protective mechanism against oxygen radical damage, in which enzymes are produced in life forms to dismutate superoxide and hydrogen peroxide (Halliwell & Gutteridge, 1985). Another mechanism is a ferric iron solubilization mechanism which is achieved by synthesizing high affinity chelators for ferric iron in living cells (Fontecave & Pierre, 1993). In

mammals, the ferric iron chelators are large proteins such as ferritin and transferrin (transferrin affinity constant, K_a for $Fe^{3+} = 10^{20}\ M^{-1}$, K_a for $Fe^{2+} = 10^{2}\ M^{-1}$) (Fontecave & Pierre, 1993). In the average human adult male with a total of 4 grams of iron, 25% of it is stored in ferritin and the degraded form of ferritin, hemosiderin, 67% of iron is in hemoglobin, 10% in myoglobin and 0.3% in transferrin (Crichton, 1973; Halliwell & Gutteridge, 1984). The synthesis of ferritin is not only influenced by normal development and hormone levels but also by the iron content in the body (Weir et al., 1984).

Ferritin Assembly

The ferritin molecule (M.W. 480,000) is a hollow spherical shell (O.D. 12.0 nm, I.D. 10.0 nm) composed of 24 sausage-like subunits with 4/3/2 symmetry as shown in Figure 1.1 (Ford et al., 1984; Clegg et al., 1980; Theil, 1987). The assembly of the ferritin coat, apoferritin, is thought to occur first by forming subunit dimers from each individual subunit with a hydrophobic side (shaded area) (Figure 1.2a) facing out. Two dimers are then oriented 90° to each other with one hydrophobic end half buried to form a groove on the inner surface of the protein shell (Ford et al., 1984; Rice et al., 1982; Theil, 1987). The hydrophobic end that joins two dimers is then merged with two other dimers (Figure 1.2b) to form one of six 4-fold channels

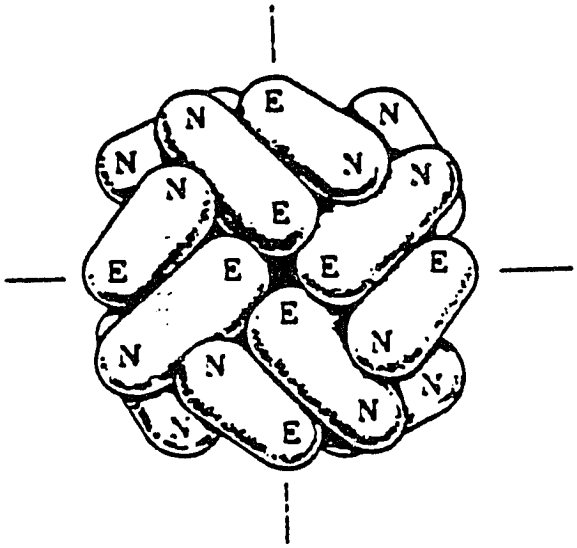

Figure 1.1: Schematic representation of horse spleen ferritin molecule viewed down the 4-fold axis. (Ford et al., 1984)

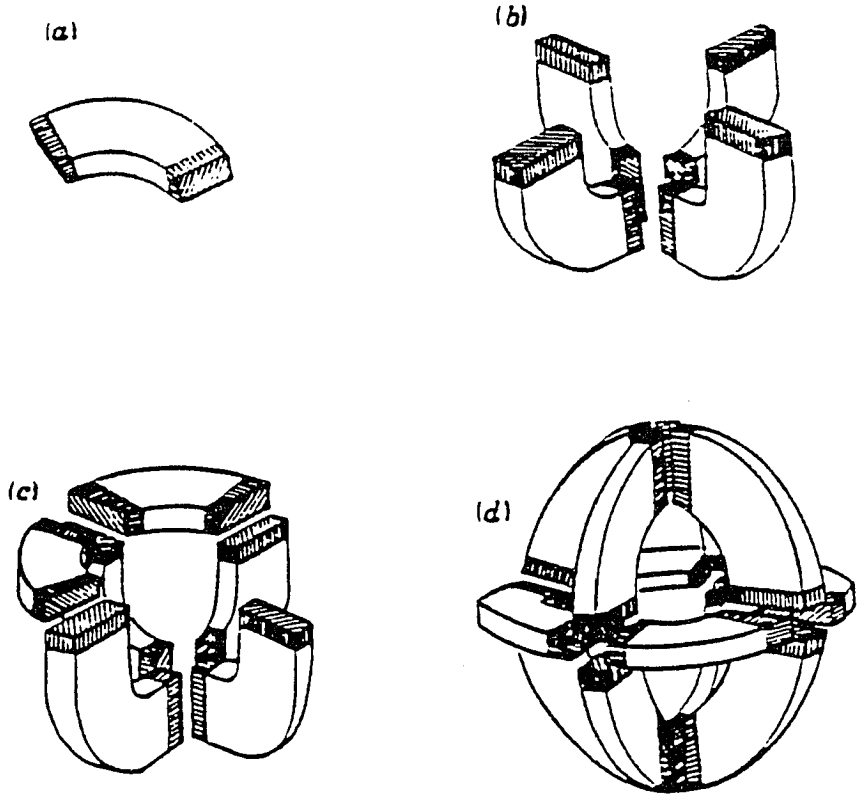

Figure 1.2: Schematic diagram of the assembly of ferritin coat.

(a) Formation of a subunit dimer with hydrophobic patches (shaded area) facing out.
(b) Formation of a 4-fold channel by four dimers with their hydrophobic ends joined together.
(c) Additional dimers form a 3-fold channel with majority of the hydrophobic areas buried.
(d) 24mer form a apoferritin molecule with all hydrophobic ends covered. (Ford et al.1984)

lined with twelve leucine residues showing hydrophobic characteristics (Ford et al., 1984; Rice et al., 1982; Theil, 1987) (Figure 1.3a). Additional dimers then bring the rest of the hydrophobic ends together (Figure 1.2c) to form one of eight 3-fold hydrophilic channels lined with three aspartic acid, three glutamic acid, six serine with three cysteine and six histidine residues nearby (Andrews et al., 1992; Rice et al., 1982; Theil, 1987) (Figure 1.3b). All channels have a funnel shape with the larger diameter end facing the outside of the molecule and the narrow end, diameter of ~3 - 5 Å, towards the cavity (Rice et al., 1982; Andrews et al., 1992). The 24mer is eventually folded together with all the hydrophobic residues buried along the 4-fold axes (Figure 1.2d).

Formation of Iron Core

Formation of the iron core, a crystalline hydrous iron ferric oxide phosphate complex ($FeOOH_8 \cdot FeO \cdot OPO_3$ for horse spleen ferritin) of 60 - 70 Å diameter, is a self-catalyzing process which occurs after the assembly of the apoferritin shell (Ford et al., 1984; Lawson et al., 1989; Theil, 1987; Harrison et al., 1986). The amount of iron that can be stored in the core of a ferritin molecule is thought to approach ~4500 iron atoms with an average iron loading of 2300 atoms (Ford et al., 1984; Watt et al., 1985). The ferric core structure in ferritin is independent of buffer

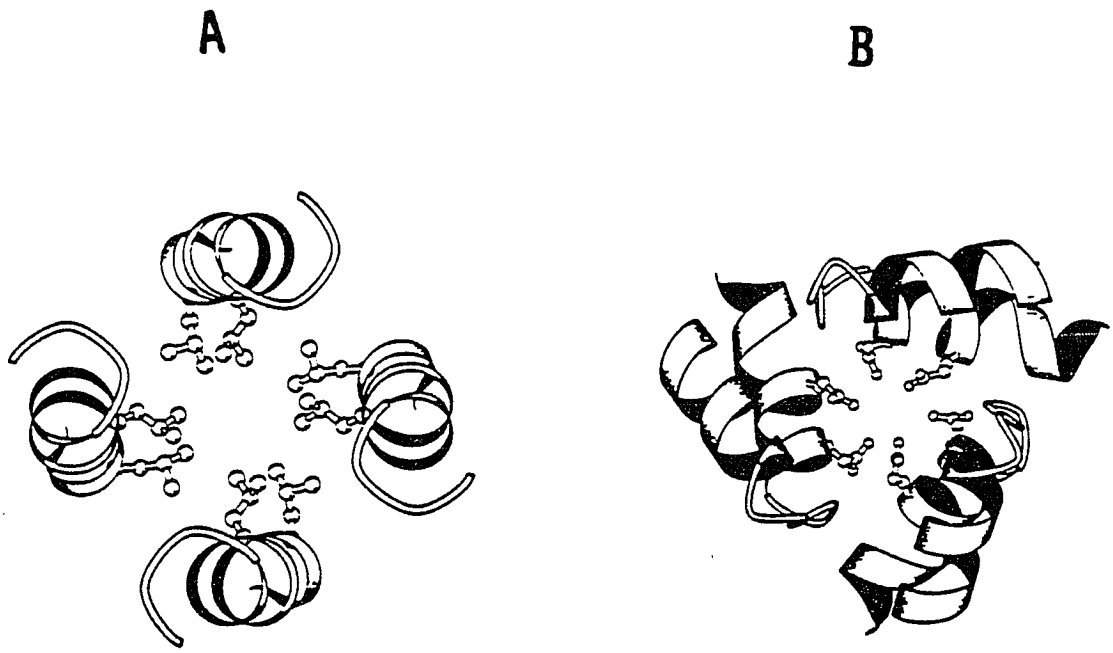

Figure 1.3: Ribbon diagram of (A) the hydrophobic 4-fold channel, (B) the hydrophilic 3-fold channel. (Feig & Lippard, 1993)

ions, in contrast to the hydrous ferric oxide core without ferritin present (Theil et al., 1983). Iron core formation can be accomplished *in vitro* by adding ferrous iron directly to apoferritin in the presence of oxygen or other oxidants. Addition of ferric ions directly to apoferritin to reconstitute ferritin has been unsuccessful, suggesting that iron is stored in the ferric form but transported in the ferrous form (Theil, 1987; Ford et al., 1984). Release of the iron from the ferritin core also requires the reduction of ferric iron to ferrous iron, the latter is then stabilized by additional ferrous chelators (Theil et al., 1983).

The ferritin shell, especially the building blocks of the shell subunits, play essential roles in both iron deposition within the shell and release of iron from the core (Andrews et al., 1992; Theil et al., 1983), as discussed in detail below. The 3 and 4-fold channels of the ferritin coat, however, do not appear to be as functionally important as they were originally predicted to be (Feig & Lippard, 1993), even though the 3-fold channels have been shown to serve as entry points for iron transport into the ferritin cavity (Treffry et al., 1993).

The Role of Phosphate

In addition to the predominantly ferric hydrous oxide, a small amount of phosphate (1 - 1.5%) has also been

detected in the iron core micelle (Crichton, 1973). Ferritin cores reconstituted with and without the presence of phosphate give the same X-ray or electron diffraction pattern, suggesting that the phosphate is located on the surface and/or in the disordered region of the iron core (Theil et al., 1983). Magnesium citrate can only precipitate 60% of the phosphorus from the ferritin core, suggesting that the phosphate is probably also tightly bound in the core interior where it cannot be reached by magnesium citrate (Theil et al., 1983). The interaction of phosphate with the iron of the core has been demonstrated by Mössbauer studies showing that the ferric core size is reduced from 60 Å to 48 Å in the presence of phosphate (Theil et al., 1983; Crichton, 1973). In addition, the iron/phosphate ratio has been found to be higher when the iron content in the core is lower. All these changes in iron core composition from the presence of phosphate may be the reason for the kinetic differences observed in the process of iron deposition and release in ferritin (Cheng & Chasteen, 1991; Heqing et al., 1993; Watt et al., 1992).

Ferritin Subunits

Recent studies have shown that subunits of two types, L (light) type subunit with M.W. of 19,000 and H (heavy) type subunit with M.W. of 21,000, play special roles in iron deposition in ferritin (Andrews et al., 1992; Levi et al.,

1992; Arosio et al., 1978; Clegg et al., 1980). These two types of subunits are genetically and functionally distinct, although approximately 55% of the 174 amino acid residues in the L subunit share sequence identity with the 183 amino acid residues in the H subunit (Andrews et al., 1992; Levi et al., 1992). It has been suggested that the L-subunit may be superior to the H-subunit at promoting iron core formation, while the H-type is more efficient for the metabolically active function of iron oxidation than the L type (Cozzi et al., 1990; Levi et al., 1992; Andrews et al., 1992; Harrison, 1986). The H and L subunit composition differs between ferritins in different tissues, which may reflect functional differences between subunit types. For example, the metabolically more active horse heart ferritin has 90% H subunit and 10% L subunit while the higher iron content, thus the iron storing, horse spleen ferritin has only 16% of H and 84% L subunit ratio (Cozzi et al., 1990; Harrison, 1986). Ferritin from the same tissue of different animals may also contain different H and L subunit composition. One example is sheep spleen ferritin having 62% H and 38% L subunit compared to 16% H and 84% L in horse spleen ferritin (Mertz & Theil, 1983).

The difference in H and L subunit ratio also changes the protein surface charge due to the difference in amino acid composition of two subunits (Andrews et al., 1992). In general, each subunit has more acidic residues than basic,

thus the isoelectric focusing point (pI) of a ferritin molecule is between 4.5 - 5.5 (*e.g.* horse spleen ferritin has pI of 4.5) (Theil, 1987; Harrison, 1986).

The detailed structure of each subunit has been studied by high resolution X-ray crystallography (Ford et al., 1984; Theil, 1987). Four long α helices, A (horse spleen ferritin residue numbering, 10 - 39), B (45 - 72), C (92 - 120) and D (124 - 155), a short α helix, E (160 - 169) and a loop, L (73 - 91) have been identified as shown in Figure 1.4 (Rice et al., 1982; Ford et al., 1984). Helix pairs A, B and C, D are connected by short turns in an anti-parallel fashion while B and C are connected by the loop, L. The four helices form a helix bundle with the side chains interacting with each other to form a hydrophobic core extending the full length of the bundle, ~3.5 nm (Ford et al., 1984; Rice et al., 1982). A narrow channel of 1.0 Å has been observed to pass through the inner and outer surfaces of the H-subunit and connect to the active site for Fe(III) oxidation. The channel has been postulated to serve as a possible intra subunit transportation tunnel for iron and oxygen (Lawson et al., 1991). This channel, however, is blocked by a salt bridge in the L subunit, which may account for some of the functional difference between the H and L subunits.

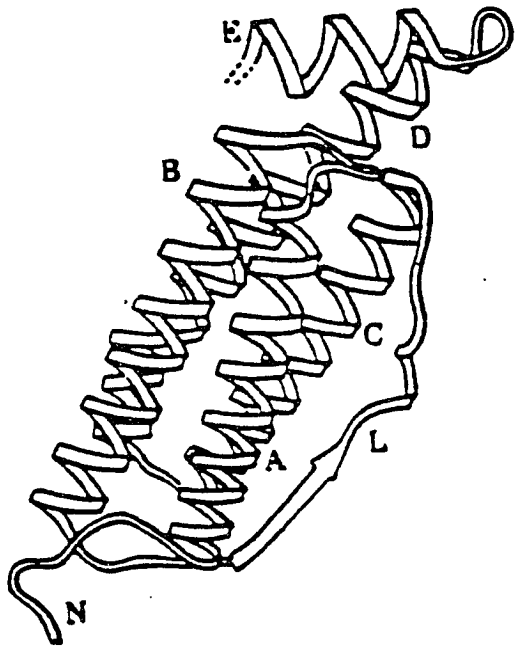

Figure 1.4: Ribbon diagram of the alpha carbon backbone of an individual subunit. (Ford et al., 1984)

Active Sites of Ferritin

In addition to the intra-subunit channel, several important or potentially important functional sites for iron incorporation in ferritin have been identified within the H-subunit helix bundle by X-ray crystallography and site directed mutagenesis (Lawson et al., 1991; Lawson et al., 1989). An essential iron complexation and oxidation site, the ferroxidase site, site A (Figure 1.5), consisting of Glu-27, Glu-62 and His-65, has been located ~7-10 Å from the inner surface (Treffry et al., 1992; Crichton et al., 1980). This site has been shown to be responsible for initial iron oxidation and is possibly the Fe(III) source for the ferrihydrite core formation in H ferritin (Levi et al., 1992; Andrews et al., 1992). It has also been suggested that the ferroxidase site in the H subunit may serve as the Fe(III) source for L ferritin when both ferritins are present in the same solution (Levi et al., 1992; Andrews et al., 1992). A nearby iron binding site, the intermediate site B which involves Glu-61, Glu-62 and Glu-107, has also been located ~3 Å from site A (Lawson et al., 1991; Treffry et al., 1992) (Figure 1.5), which has been suggested as the location of Fe(II) - Fe(III) intermediate mixed-valence μ-oxo-dimer (Andrews et al., 1992; Treffry et al., 1992; Hempstead et al., 1994; Hanna et al., 1991b). Another amino acid residue, Tyr-34, linked to the Glu-107 of site B through hydrogen bonds, is thought to be responsible for the

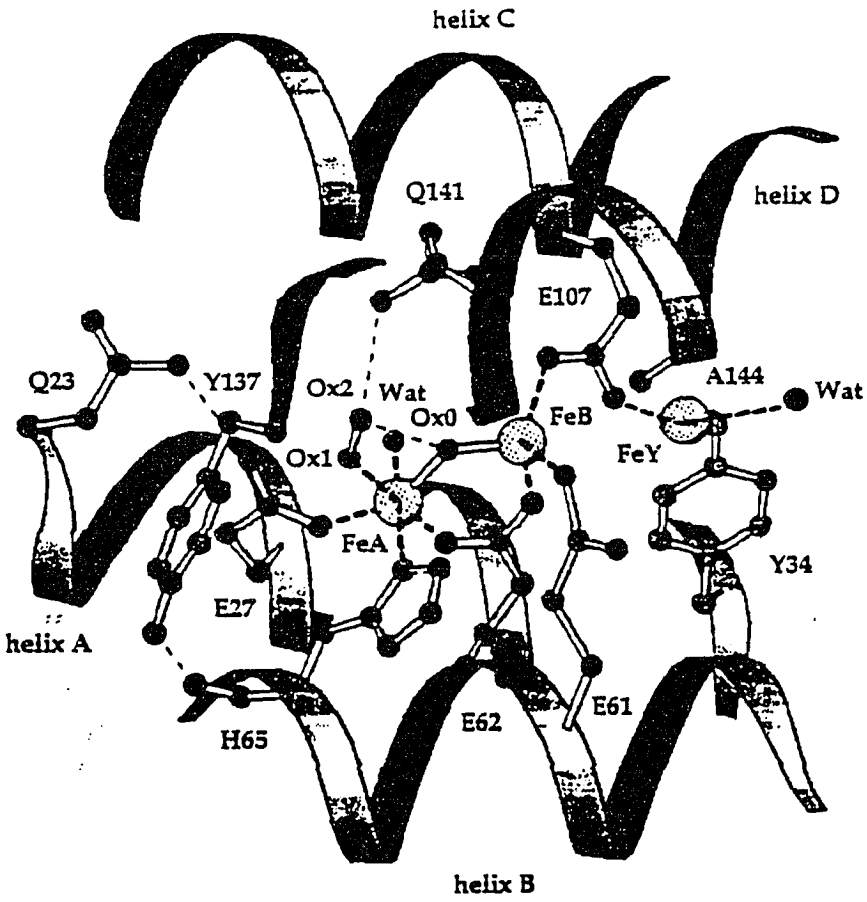

Figure 1.5: Identification of possible location for iron binding sites A, B and Y. (Feig & Lippard, 1993)

recent discovery of an Fe(III)-tyrosine complex (site Y) in both bull frog and human H-chain ferritin (Figure 1.5) (Waldo et al., 1993; Waldo & Theil, 1993; Bauminger et al., 1993; Guiles et al., 1990). Iron oxidation at this site is claimed to be the fastest step in the iron deposition process within ferritin (Waldo & Theil, 1993).

Unlike the above sites which are conserved on the H-subunit only (Treffry et al., 1992; Andrews et al., 1992), another iron binding site, the nucleation site, site C, consisting of Glu-61, Glu-64 and Glu-67 residues, is found in both the H and L subunits. This site has been proposed to initiate the nucleation of the ferric iron which has migrated from site A and B (Lawson et al., 1991). In addition, kinetic studies using site directed mutants have suggested that the nucleation site has some iron oxidation catalytic ability as well (Sun et al., 1993).

Metal Binding Site in Ferritin

The discovery of a cluster of iron binding sites on the H-subunit is of great importance for understanding iron deposition in ferritin as described above. Unfortunately, the direct observation of iron binding in ferritin has not been possible until recently (Theil et al., 1983; Hempstead et al., 1994). Thus, other metal ions, whose binding sites in ferritin may be detected in electron density maps, have been frequently used to probe the number and the location of

the putative iron binding sites through competitive binding studies with iron (Clegg et al., 1980; Weir et al., 1984; Harrison, 1986). So far, three Tb^{3+} sites have been located inside the H-subunit, which led to the discovery of ferroxidase site A, the intermediate site B and the nucleation site C (Lawson et al., 1991; Feig & Lippard, 1993) (Figure 1.5). Two other Tb^{3+} sites have also been observed at the outer rim of the 3-fold channel, near the subunit interface and liganded by three Asp-131 and three Glu-134 residues. Mutation of these residues has identified the 3-fold channel as an iron entry point (Chasteen & Theil, 1982; Weir et al., 1984; Treffry et al., 1993). Besides the terbium binding sites, two types of zinc binding sites have also been located, with one near the outer rim of the 3-fold channel and the other one at the ferroxidase site (Treffry et al., 1993; Crichton & Ward, 1992; Sun & Chasteen, 1992; Harrison, 1986).

Two types of VO^{2+} binding to ferritin have also been observed, one site involves a nitrogen ligand as shown by ENDOR and ESSEM studies (Gerfen et al., 1991; Hanna et al., 1991a), which was later established as His-118 (Chasteen et. al, unpublished results). The other VO^{2+} binding site was postulated to be in the 3-fold channel based on the titration of the VO^{2+} EPR signal (Wardeska et al., 1986; Chasteen & Theil, 1982), however, measurements with site-directed mutants have shown this not to be the case

(Chasteen, et. al., unpublished result). In addition, Cd^{2+} and UO_2^{2+} have also been observed to bind to ferritin. The postulated binding sites of the various metals are summarized in Table 1.1.

Mechanism of Iron Deposition in Ferritin

With the help of the recent discovery of functional binding sites for iron, some of the steps for iron deposition in ferritin are now understood. These steps include: Fe(II) enters the cavity through a 3-fold channel to the inside of an H subunit where it binds at the ferroxidase site A and is catalytically oxidized to Fe(III) by molecular oxygen (Lawson et al., 1989; Andrews et al., 1992; Levi et al., 1992; Treffry et al., 1993). The rate of the iron oxidation has been shown to be 1st order with respect to the protein concentration and displays saturation kinetics with regard to Fe(II) and O_2, indicating that ferritin acts as a true ferroxidase enzyme (Sun & Chasteen, 1992; Bakker & Boyer, 1986). The stoichiometry of the iron oxidation is two iron atoms oxidized per oxygen molecule consumed (Figure 1.6) (Xu & Chasteen, 1991; Sun & Chasteen, 1992). The reaction is described by equation 1.1 with H_2O_2 being the final product of dioxygen reduction.

$$2Fe^{2+} + O_2 + 4H_2O \rightarrow 2FeOOH_{core} + H_2O_2 + 4H^+ \qquad (1.1)$$

Table 1.1: The location and amino acid ligands for metal binding in horse spleen ferritin (Harrison, 1986)

No	*Ligands*	*Metals*	*Location*
1	Asp127, Asp127′ Asp127″	Cd^{2+}, Zn^{2+}	3-fold channel (inside)
2	Glu130, Glu130′ Glu130″, $3H_2O$	Cd^{2+}, Zn^{2+}	3-fold channel (outside)
3	Asp127, Asp127′, Asp127″, Glu130, Glu130′, Glu130″	Tb^{3+}	3-fold channel (middle)
4	Glu57, Glu60	Tb^{3+}	Cavity surface, on B helix
5	Glu57 (Glu136) H_2O	UO_2^{2+}	Cavity surface, between B and D helices
6	Glu63 (Arg59)	UO_2^{2+}	Cavity surface, between B and B′

Brackets denote residues not conserved in all known sequences. Other ligands are conserved. Prefixes ′ and ″ denote residues from neighbouring, symmetry related subunits.

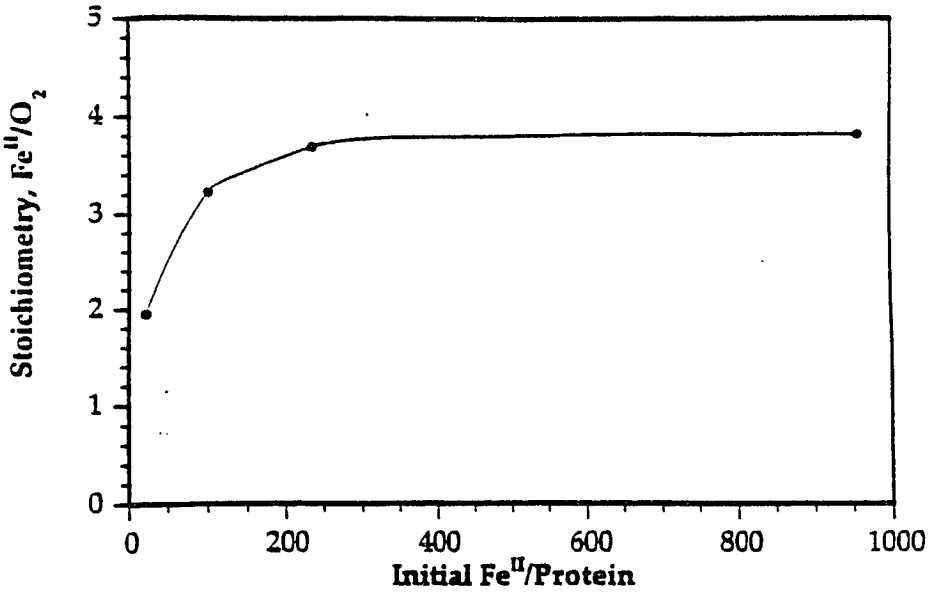

Figure 1.6: Stoichiometry of iron(II) oxidation as a function of initial iron loading to apo horse spleen ferritin. (Xu & Chasteen, 1991)

The Fe(III) produced at site A is then shifted to the intermediate site B where the μ-oxo-bridged Fe(II)-Fe(III) dimer, the precursor of the Fe(III)-Fe(III) dimer, is formed between site A and B or at least partly formed at site A and B (Treffry et al., 1992; Hanna et al., 1991b; Treffry et al., 1993; Hempstead et al., 1994). The Fe(III) from the Fe(III)-Fe(III) dimer then dissociates and migrates to the center of the protein shell with the help of the Glu-61 from the nucleation site C, to form an iron ferrihydrite core with no specific attachment to the protein (Treffry et al., 1992; Bakker & Boyer, 1986; Lawson et al., 1991; Feig & Lippard, 1993). The mechanism above follows the protein catalysis model of Crichton & Roman, 1978. Further Fe(II) deposition then occurs directly on the mineral surface where the Fe(II) is oxidized with a stoichiometry of four iron(II) per dioxygen consumed (Figure 1.6) (Xu & Chasteen, 1991). This Fe^{2+} oxidation reaction is described by equation 1.2 with H_2O as the final product of the dioxygen reduction (Crichton & Ward, 1992; Sun & Chasteen, 1992; Xu & Chasteen, 1991).

$$4Fe^{2+} + O_2 + 6H_2O \rightarrow 4FeOOH_{core} + 8H^+ \qquad (1.2)$$

This iron oxidation pathway follows the crystal growth model in which the rate of core formation is controlled by the availability of the mineral surface (Figure 1.7) (Clegg et

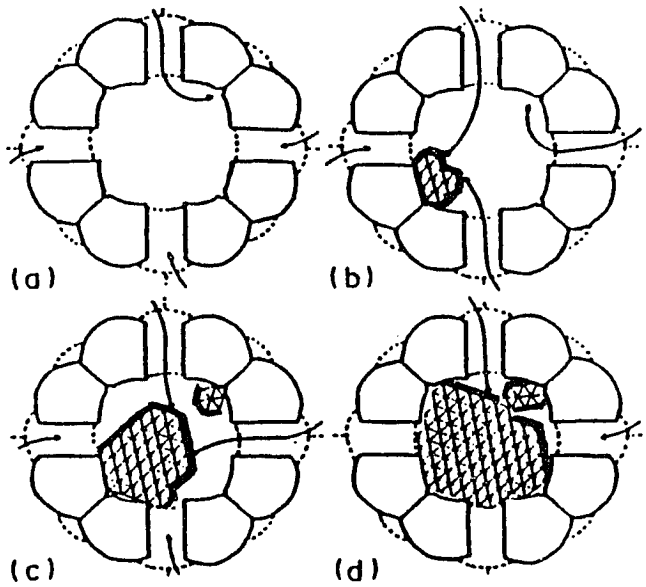

Figure 1.7: The "crystal growth" model for ferritin formation. The rate of iron core formation is mineral surface area dependent. The available mineral surface (thick line) for incoming FeOOH increases from (A) to (C) and decreases from (C) to (D). (Clegg et al., 1980)

al., 1980; Macara et al., 1973).

Radical Formation

Superoxide and hydrogen peroxide are continuously generated under non-pathological conditions in an aerobic cell (Fontecave & Pierre, 1993). The concentration of these active species are very low due to the constant conversion of these species to water by superoxide dismutase, catalase and other enzymes. Oxygen toxicity, which has been suspected to cause many biological irregularities such as inflammatory diseases, Parkinson disease, iron overload syndrome and aging (Fontecave & Pierre, 1993), are thought to arise from the conversion of superoxide and hydrogen peroxide to the highly reactive hydroxyl radical by iron under aerobic conditions. Hydroxyl radical is so reactive that it is scavenged by the neighboring amino acid residues instantly causing protein fragmentation and cross linking (Davies et al., 1991). Hydroxyl radical is formed in the iron catalyzed Harbor Weiss process (Reactions 1.3 to 1.5) (Graf et al., 1984).

$$Fe^{2+} + O_2 \rightarrow Fe^{3+} + O_2^- \quad (1.3)$$

$$2O_2^- + 2H^+ \rightarrow H_2O_2 + O_2 \quad (1.4)$$

$$Fe^{2+} + H_2O_2 \rightarrow Fe^{3+} + {}^{\cdot}OH + OH^- \quad (1.5)$$

It has been suggested, that iron ions which are

attached to proteins such as ferritin are not involved in the promotion of hydroxyl radical production outside the protein (Halliwell & Gutteridge, 1988). However, hydroxyl radicals may be produced inside the protein, attacking the protein itself, presumably on or near the iron binding site (Fontecave & Pierre, 1993). The oxidative stress on the iron protein can cause liberation of iron ions which promote hydroxyl radical formation (Davies et al., 1991; Halliwell & Gutteridge, 1988). Hemoglobin has been shown to degrade in the presence of H_2O_2, presumably due to the site specific $\cdot OH$ attack, resulting in iron release (Halliwell & Gutteridge, 1988; Crichton & Ward, 1992).

Recent kinetic studies have shown the production of hydrogen peroxide inside ferritin, presumably at the ferroxidase site, during the initial stages of iron deposition, especially at low iron loading increments (equation 1.1) (Sun & Chasteen, 1992). Further observations have shown that the amino acid composition of ferritins is changed during the iron loading process with the basic amino acid residues lysine and histidine being depleted, resulting in a lower protein isoelectric focusing point (De Silva et al., 1992). Ferritin radicals have also been observed previously by EPR spectroscopy and one radical has been identified as a hydroxyl derived radical (Grady et al., 1989). Therefore, it is important to understand the consequences of radical formation in ferritin and its damage

to the protein.

To date, the actual steps of iron deposition responsible for radical formation in ferritin and the roles that the protein radical may or may not play during the iron oxidation process remain unclear. The relationship between the iron oxidation and the mineralization process has yet to be studied. The functions of H and L subunits, the pathways and kinetics of the iron deposition in different ferritins are the main interest of current ferritin research.

In Chapter II, the kinetics studies of iron loading in horse spleen and recombinant human H and L ferritins were conducted in which a combination of oxygen electrode and pH stat apparatus was utilized to simultaneously monitor the iron oxidation and hydrolysis reactions. Information on relationships between Fe(II) oxidation, dioxygen reduction and proton release are obtained, which enrich the mechanism that describing initial iron oxidative deposition in the human H-chain and the horse spleen ferritins. The human L-ferritin is also shown to have the ability to facilitate iron oxidation. The iron oxidation pathway in L-chain ferritin predominantly follows the iron mineral surface oxidation/hydrolysis pattern while ferroxidation is the principle iron oxidation passage in the H-chain ferritin.

In Chapter III, two different ferritin radicals have been observed in native horse spleen, recombinant horse L and recombinant human H-chain ferritins (Grady et al.,

1989). One radical formed in human H ferritin during iron(II) oxidation by dioxygen has been shown not to be a •OH-derived radical. Rather, it appears to be a Tyr-34 radical. Another radical, observed in both horse and recombinant human ferritin, has been shown to be a secondary radical derived from Fenton chemistry. Both radicals are produced in very low yields and do not appear to play important roles in iron ferroxidation.

CHAPTER II

OXIDATION AND HYDROLYSIS KINETICS OF HORSE SPLEEN AND RECOMBINANT HUMAN H AND L CHAIN FERRITIN

Introduction

Coexistence of H and L subunits in the same protein molecule appears to be biologically favored since no native homopolymer H or L ferritins are found in mammals (Andrews et al., 1992; Levi et al., 1992) partly because H and L subunits are functionally distinct even though they share 55% amino acid sequence identity (Theil et al., 1983). The H subunit is known to be superior in rapidly oxidizing Fe(II) to Fe(III) on an iron binding site, the ferroxidase site consisting of Glu-27, Tyr-34, Glu-62, His-65, Glu-107 and Gln-141 (Lawson et al., 1989; Lawson et al., 1991; Hempstead et al., 1994). Two other iron binding sites, the putative intermediate site (Glu-61, Glu-62, Glu-107) and the nucleation site (Glu-61, Glu-64, Glu-67) have also been identified on the H subunit and are thought to be involved in the nucleation of the iron core (Treffry et al., 1992; Lawson et al., 1991). No ferroxidase site has been located on the L-subunit, but the nucleation site important for initiating iron core formation is conserved there (Levi et al., 1992; Bauminger et al., 1991; Andrews et al., 1992), which may account for the L subunit being better at converting Fe(III) species to core nuclei (Levi et al.,

1992).

The impact of iron active sites on core size, core species distribution and core crystallinity have been studied by Mössbauer spectrometry and X-ray diffraction (Wade et al., 1991; Bauminger et al., 1991; Bauminger et al., 1993). Mutation of the H-subunit ferroxidase site has been shown to increase the size of the ferric core so that it resembles that of recombinant L-chain ferritin (HuLF) (Wade et al., 1991). The mutation of both ferroxidase and nucleation sites has been found to nearly eliminate the crystal core formation completely, suggesting essential roles for these active sites in iron core formation (Wade et al., 1991).

A recent study has shown that iron is transferred intermolecularly from the recombinant H-chain ferritin (HuHF) to the L-chain ferritin (HuLF) with the H homopolymer serving as a ferric iron source through catalytic oxidation of Fe(III) (Levi et al., 1992; Andrews et al., 1992; Bauminger et al., 1992). Thus, the important roles that recombinant homopolymer H and L proteins as well as native heteropolymers, such as horse spleen ferritin (HoSF, 16% H and 84% L), play in iron oxidation and mineralization are of great interest.

The iron oxidation kinetics of HuHF and HoSF have been studied extensively (Xu & Chasteen, 1991; Sun & Chasteen, 1992; Sun et al., 1993). A one electron iron oxidation has been identified as the dominant reaction occurring on the ferroxidase site with the postulated intermediate product

being superoxide. The initial iron deposition mechanism (mechanism I) is described in equations 2.1 - 2.3 (Sun & Chasteen, 1992; Grady et al., 1989).

$$Fe^{2+} + O_2 + P \rightarrow Fe^{2+}(O_2)P \quad (2.1)$$

$$Fe^{2+}(O_2)P \rightarrow Fe^{3+}P + O_2^- \quad (2.2)$$

$$Fe^{3+}P + 2H_2O \rightarrow FeOOH_{core} + P + 3H^+ \quad (2.3)$$

The fate of the superoxide is described by reaction 2.4.

$$2O_2^- + 2H^+ \rightarrow H_2O_2 + O_2 \quad (2.4)$$

In this iron oxidation pathway, ferritin serves as an enzyme for iron oxidation in accord with the protein catalysis model (Xu & Chasteen, 1991; Crichton & Roman, 1978). The overall reaction, which is the sum of reactions 2.1 through 2.4, is summarized by equation 2.5.

$$2Fe^{2+} + O_2 + 4H_2O \rightarrow 2FeOOH_{core} + H_2O_2 + 4H^+ \quad (2.5)$$

However, the superoxide formation has not been observed directly either by the effect of superoxide dismutase on the rate of oxidation or by superoxide radical spin trapping experiments (Sun & Chasteen, 1992; Grady et al., 1989; Chapter III). Hence a second mechanism (Mechanism II) was proposed as

described in equations 2.6 - 2.8, where the superoxide anion remains associated with the iron binding site and therefore is not detectable by the above techniques. Either Mechanism I or II is consistent with the net oxidation and hydrolysis reaction 2.5 and with the observed kinetics (Sun & Chasteen, 1992; Sun et al., 1993).

$$Fe^{2+} + O_2 + P \rightarrow Fe^{2+}(O_2)P \quad (2.1)$$

$$Fe^{2+}(O_2)P \rightarrow Fe^{3+}(O_2^{-})P \quad (2.6)$$

$$Fe^{3+}(O_2^{-})P + Fe^{2+} \rightarrow Fe^{3+}(O_2^{2-})PFe^{3+} \quad (2.7)$$

$$Fe^{3+}(O_2^{2-})Pfe^{3+} + 4H_2O \rightarrow 2FeOOH_{core} + P + H_2O_2 + 4H^{+} \quad (2.8)$$

When the amount of iron loaded into ferritin increases above a certain level (*e.g.* above 50 Fe(II)/protein in HoSF), iron oxidation follows a different pathway, with 4 Fe(II) being oxidized per O_2 consumed and H_2O as a final product of dioxygen reduction being described by equation 2.9 (Xu & Chasteen, 1991). This reaction occurs directly on the surface of the ferric mineral core, following the crystal growth model for core formation (Harrison et al., 1986; Clegg et al., 1980).

$$4Fe^{2+} + O_2 + 6H_2O \rightarrow 4FeOOH_{core} + 8H^{+} \quad (2.9)$$

The stoichiometries of the various iron oxidation reactions in the ferritins containing H subunit have been

studied extensively; however, questions about the initial steps of iron oxidation and mineralization, the intermediate steps of dioxygen reduction in H-chain ferritin, and the kinetics of iron deposition in L-chain ferritin have remained unanswered. In this study, a system that combines both electrode oximetry and Ph stat to simultaneously monitor iron oxidation and proton release kinetics has been employed. Recombinant homopolymer H and L subunit ferritins as well as a native ferritin, horse spleen ferritin, have been studied to further define the functionality of each subunit type in the mechanism of iron deposition. The results show that the H-subunit of a ferritin catalyzes an initial iron oxidation at a protein active site, following a ferroxidation pathway with superoxide being the likely product of dioxygen reduction. The L-subunit also facilitate iron oxidation, but the iron deposition in L-chain ferritin occurs by a mineral surface oxidation/hydrolysis reaction.

Materials and Methods

Horse spleen ferritin, 3x crystallized, cadmium free, was purchased from Boehringer-Mannheim. Recombinant human H and L ferritins were supplied by Dr. Paolo Arosio and coworkers at the University of Milan. Apoferritin was prepared by reduction with dithionite (Bauminger et al., 1991). The concentrations of apoferritins were determined by the BioRad assay which is based on the differential absorbance change of

a dye, Coomassie Brillian Blue G250, at 595 nm in response to protein concentrations.

Ferrous sulfate and sodium sulfate were purchased from Baker Scientific Inc. Monobasic and dibasic phosphates were obtained from Fisher Scientific Inc. and MOPS buffer from Research Organics. Sodium hydrosulfite (dithionite, technical grade), sodium acetate, sodium chloride, terbium chloride, 2-chloro-2-methyl propane (t-butyl chloride) and 2,2-dipyridyl were purchased from Aldrich. All chemicals were reagent grade or purer unless otherwise stated.

Reaction rates of iron oxidation and hydrolysis were monitored simultaneously in a specially designed reaction cell fitted with an oxygen electrode (MI 730), a pH electrode (Customized), a reference electrode (MI 402, Microelectrodes, Inc.), a NaOH delivery lead from the pH stat apparatus (Radiometer America, Inc., autoburette, ABU80; titrator, TTT80 and pH meter, PHM 82) and a syringe needle immersed in the 480 μl protein solution. The system was tested using the pseudo first order hydrolysis reaction of t-butyl chloride in water. A 0.007 M stock solution of t-butyl chloride in acetone was added to a solution containing 0.1 M Na_2SO_4 at 20 °C. As the reaction proceeded, the pH was maintained at pH 7.0 by autotitration with 5.00 mM NaOH using the pH stat apparatus, the reaction being: t-butyl-Cl + H_2O → t-butyl-OH + HCl. A rate constant k of 0.025 s^{-1} $\pm$ 0.005 was obtained based on the rate law $d[H^+]/dt = k\ [\text{t-butyl-Cl}]_o$, which is in good

agreement with the published values of 0.020 - 0.037 s^{-1} (Adams et al., 1994). The oxygen consumption rate was tested by measuring the rates of oxidation of 0.1 - 0.4 mM Fe(II) in 4 mM NTA, 0.15 M NaCl solution at pH 6.30, 20 °C. A rate law of $-d[O_2]/dt = k[FeNTA][O_2]$ was obtained with a k value of 58 $M^{-1}s^{-1}$ for the rate constant, in reasonable agreement of the published value of 80 $M^{-1}s^{-1}$ at the higher temperature of 25 °C (Kurimura et al., 1968).

All iron oxidation reactions were conducted at pH 7.0 and 20 °C unless otherwise stated. The oxygen-saturated solution (21% O_2 atmosphere) of weakly buffered protein in 0.5 mM MOPS, 0.15 N NaCl, pH 7.0, was added to the reaction cell without an air head-space or trapped air bubbles. The solution was rapidly stirred with a micro spin bar to ensure the complete mixing of the NaOH delivered by the pH stat. The reaction was initiated by the addition of freshly prepared $FeSO_4$ stock solution (pH 3.7). A 80486 based computer with an ADA 2000 board (Real Time Devices, Inc.) was used to acquire data from both the oxygen meter and the Ph stat system. A proportional band setting of 0.1 was used in the pH stat. The oxygen consumption and the proton release rate were recorded as the oxygen percentage decrease and microliters of NaOH delivered over time, respectively.

The appropriate calculations for the concentrations of oxygen consumption and proton release were performed after data acquisition using the software Origin (Microcal

Scientific, Inc.). The initial rates of iron oxidation and iron hydrolysis were obtained from the linear A_1 term of a 3rd order polynomial curve fitted to the data following 85 - 95% completion of the reaction, namely $Y = A_0 + A_1t + A_2t^2 + A_3t^3$ and $dY/dt = A_1 + 2A_2t + 3A_3t^2$. At $t = 0$, $(dY/dt)_0$ equals A_1, where t is time in seconds and Y is either the oxygen concentration or the delivered NaOH concentration in the solution of the sample. An initial sharp increase in NaOH added, as indicated by the arrow in Figure 2.1, in the first 10 seconds of the hydrolysis curve is excluded from the curve fitting procedure since it is due to the initial rapid lowering of pH of the protein solution from free acid present in the added $FeSO_4$ stock solution. The stoichiometric ratios, $Fe(II)/O_2$ and $H^+/Fe(II)$, were calculated from the concentrations of O_2 consumed and H^+ produced at completion of the reaction and from the initial concentration of ferrous sulfate in the solution.

The rates of iron oxidation and hydrolysis in HuLF were calculated as the average rates between the first and the second minute of the reaction to avoid the effect of the initial sharp pH drop upon addition of $FeSO_4$. This procedure works well because of the slow oxidation and hydrolysis rates observed with HuLF.

Terbium inhibition experiments were performed by incubating 36 and 72 μM of $TbCl_3$ solution (pH 4) with 3 μM apoferritin in 0.5 mM MOPS and 0.15 N NaCl solution, pH 7.0,

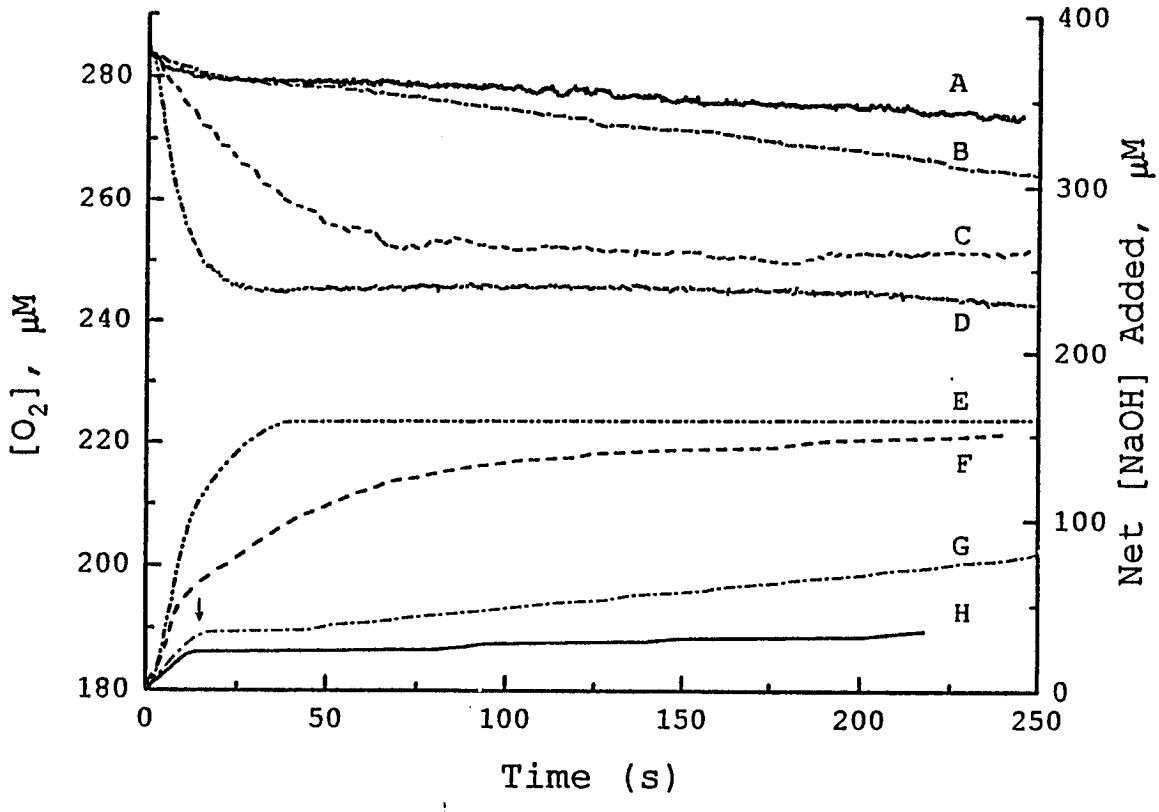

Figure 2.1: Oxygen consumption (A, B, C, D) and proton release (Measured as 10.1 mM NaOH added) (E, F, G, H) *versus* time for Fe(II) oxidation and hydrolysis reactions in the absence of protein (A, H) and in the presence of HuLF (B, G), HoSF (C, F) and HuHF (D, E). Conditions: [HuLF] = 3 μM, [HoSF] = 3 μM, [HuHF] = 2.5 μM, [Fe(II)] = 150 μM for buffer, HuLF and HoSF, [Fe(II)] = 83 μM for HuHF, in 0.15 M NaCl and 0.5 mM MOPS titrated with initial $[O_2]_0$ = 0.28 mM at fixed pH = 7.00, 20 °C (File names: A & H, 03220194, B & G 08220994; C & F, 03230194; D & E, 080894)

for at least 2 hours prior to the addition of ferrous iron to ensure the maximum inhibition by the terbium (Chasteen & Theil, 1982).

Ferritins (3 μM) with 250, 500, 750 and 1000 Fe(III) core contents were prepared by gradually adding ferrous iron to an air saturated apoferritin solution with no buffer over the course of 10 minutes while simultaneously adding 0.01 - 0.02 N NaOH to maintain the pH between 6.5 and 7.0.

When the iron oxidation and hydrolysis rates were studied below pH 6.5, 0.5 mM MES buffer was used as the weak buffer to stabilize the pH readings instead of the 0.5 mM MOPS used in the pH range from 6.5 to 8.0. The influence of phosphate on the rates of iron oxidation and hydrolysis was examined by reactions involving 146 μM $FeSO_4$ in an air-saturated 3 μM HoSF solution (Fe(II)/protein = 49) in the presence of 83 - 584 μM phosphate buffer, pH 7.0.

Results

Kinetics of Iron Oxidative Deposition in HoSF and HuHF

Figure 2.1 shows the oxygen consumption (A, B, C, D) and proton release (E, F, G, H) reaction profiles as a function of time in the presence of different ferritins at an Fe(II)/protein ratio of 50 for HoSF and HuLF and 34 for HuHF. Ferrous iron is added to a slightly buffered NaCl solution in the absence of protein (A, H) or in the presence of HuLF (B, G), HoSF (C, F) and HuHF (D, E). It can be seen that the

iron(II) oxidation and hydrolysis reactions are facilitated by all ferritins with the reaction rates ranked in the order of HuHF > HoSF > HuLF > Buffer. The kinetic curves are of a similar form for both oxygen consumption and proton release indicating that the rates of Fe(III) hydrolysis in HuHF (E) and HoSF (F) are limited by the rates of Fe(II) oxidation. The oxidation/hydrolysis kinetics with HuLF are different from those of the H-subunit containing ferritins as will be discussed in detail later in this chapter.

The oxygen consumption and proton release curves plateau at ~100 s for HoSF (C, F) and at ~40 s for HuHF (D, E), where iron oxidation is complete. The stoichiometric ratios of $Fe(II)/O_2$ = 2.3 and 2.2, $H^+/Fe(II)$ = 1.8 and 1.9 and H^+/O_2 = 4.1 and 4.2 were obtained for HoSF and HuHF, respectively. These results are in agreement with the predicted values of 2.0, 2.0 and 4.0, respectively, from reaction 2.5 for low iron loading into the protein (Xu & Chasteen, 1991; Sun & Chasteen, 1992).

Saturation kinetics in both HoSF (Figure 2.2a) and HuHF (Figure 2.2b) are observed when oxygen consumption and proton release rates are plotted as a function of iron concentration. The corresponding double reciprocal plots reveal linear relationships (Figure 2.2c, 2.2d), indicating that Fe(II) acts as a substrate for both ferritins. The apparent Michaelis constants, K_m, and turnover numbers, k_{cat}, obtained from the oxygen consumption data (Figure 2.2c, 2.2d insets) are $K_{m,Fe,HoSF}$

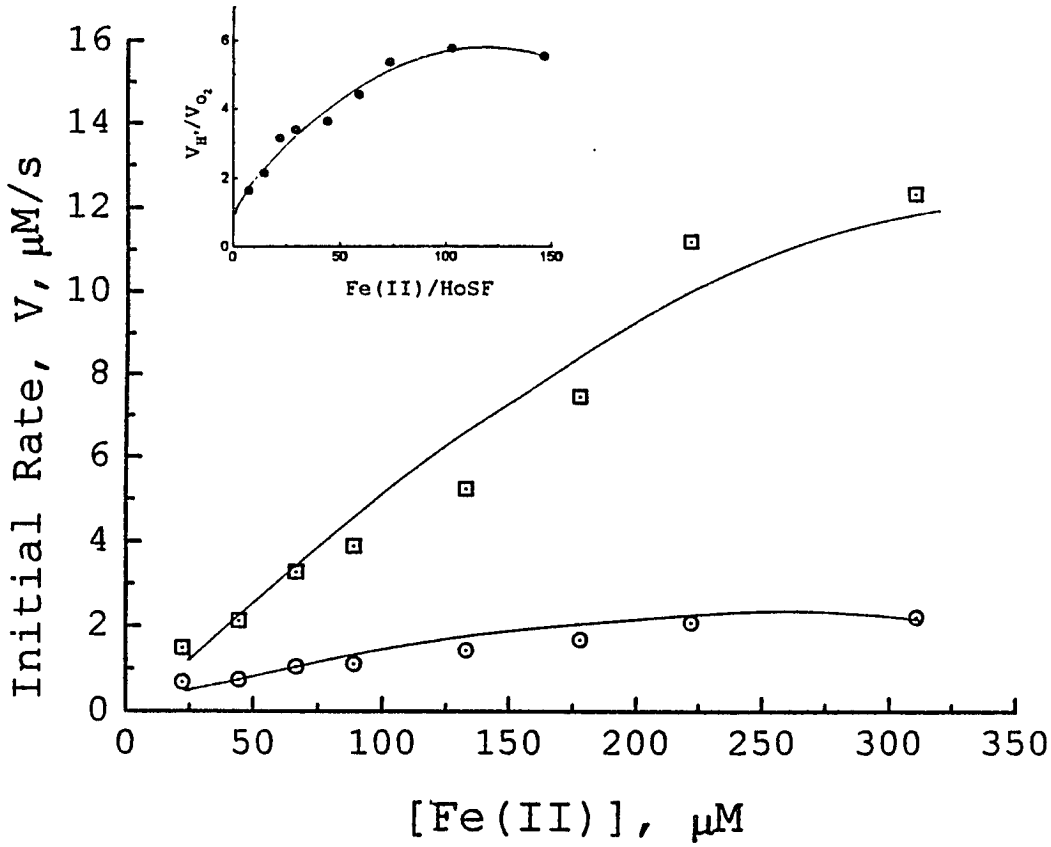

Figure 2.2a: Initial rates of oxidation (⊙) and hydrolysis (⊡) as a function of Fe(II) concentration in HoSF. Conditions: [HoSF] = 3 μM in 0.15 M NaCl and 0.5 mM MOPS, $[NaOH]_{stock}$ = 10.1 mM, $[O_2]_0$ = 0.28 mM, pH 6.98, 20 °C (File name: 032394.org) **Inset:** Ratio of initial rates of iron hydrolysis and oxidation as a function of the iron loading in HoSF.

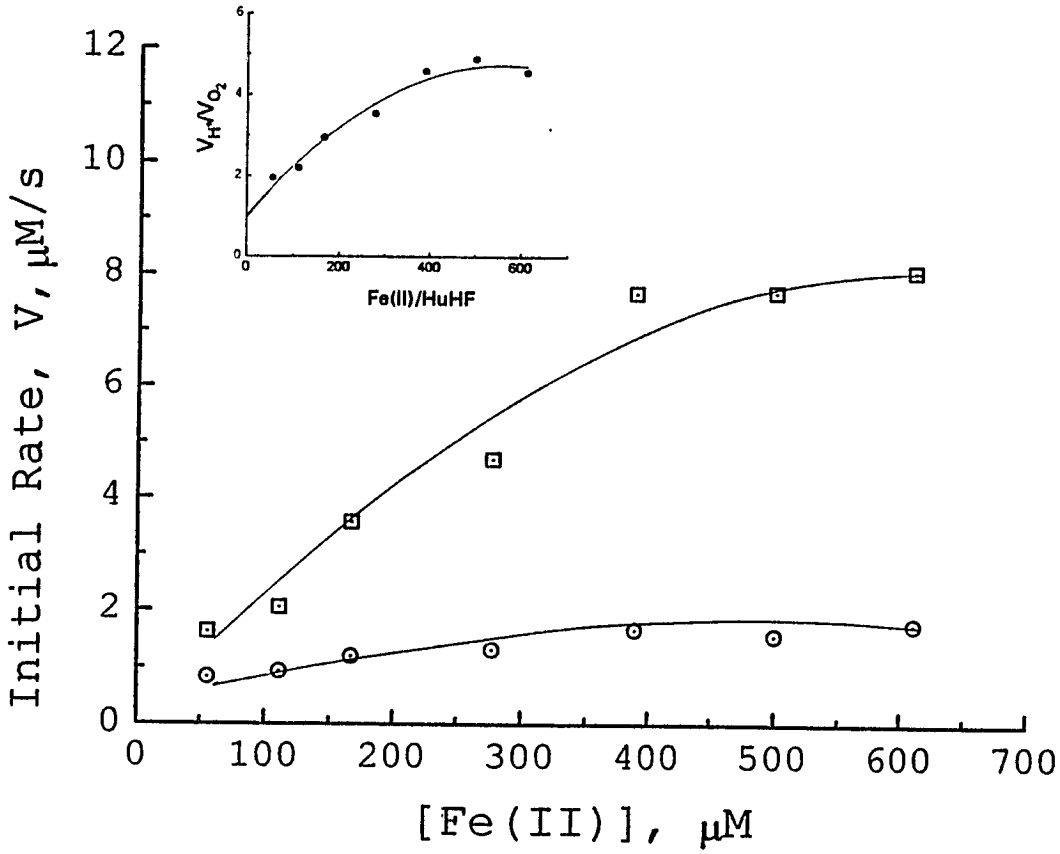

Figure 2.2b: Initial rates of oxidation (⊙) and hydrolysis (⊡) as a function of Fe(II) concentration in HuHF. Conditions: [HuHF] = 0.38 μM in 0.15 M NaCl and 0.5 mM MOPS, $[NaOH]_{stock}$ = 5.02 mM, $[O_2]_0$ = 0.28 mM, pH 7.00, 20 °C (File name: 080394.org) **Inset:** Initial rate ratio of iron hydrolysis and oxidation as a function of the iron loading to HuHF.

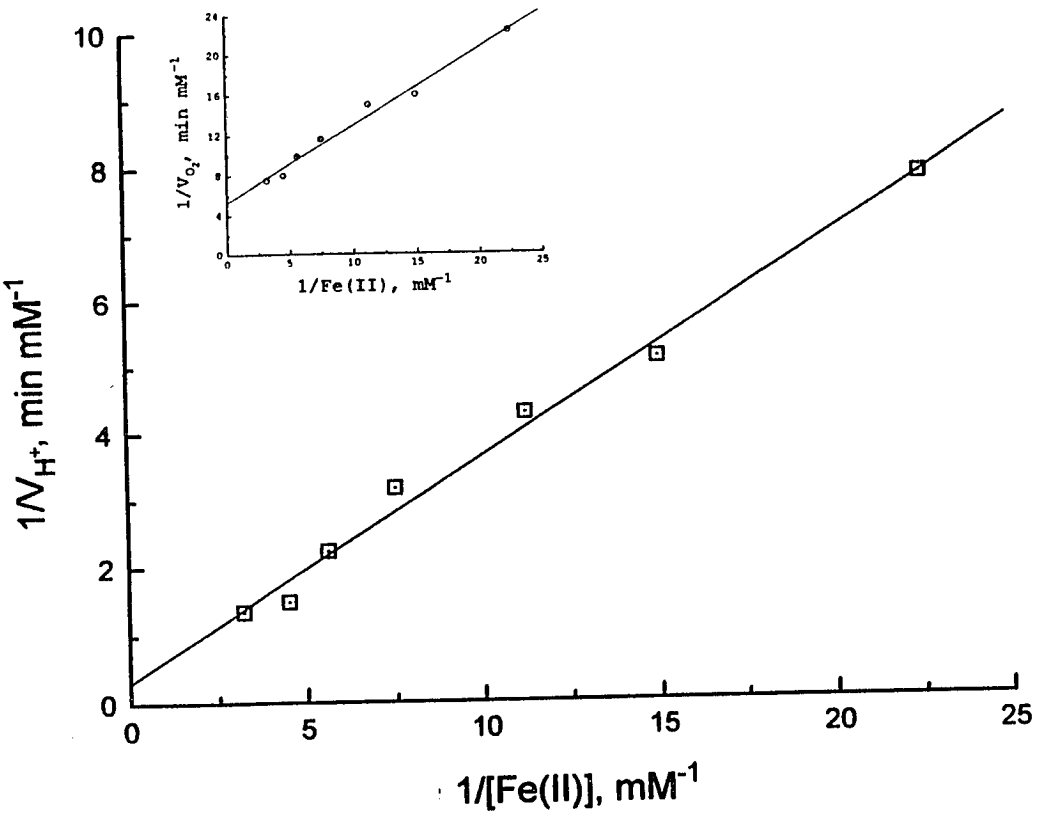

Figure 2.2c: Lineweaver-Burk plots of reciprocal proton release and oxygen consumption (inset) rates *vs.* 1/Fe(II) concentration in HoSF with least-squares straight line fit shown (File name: 032394.org).

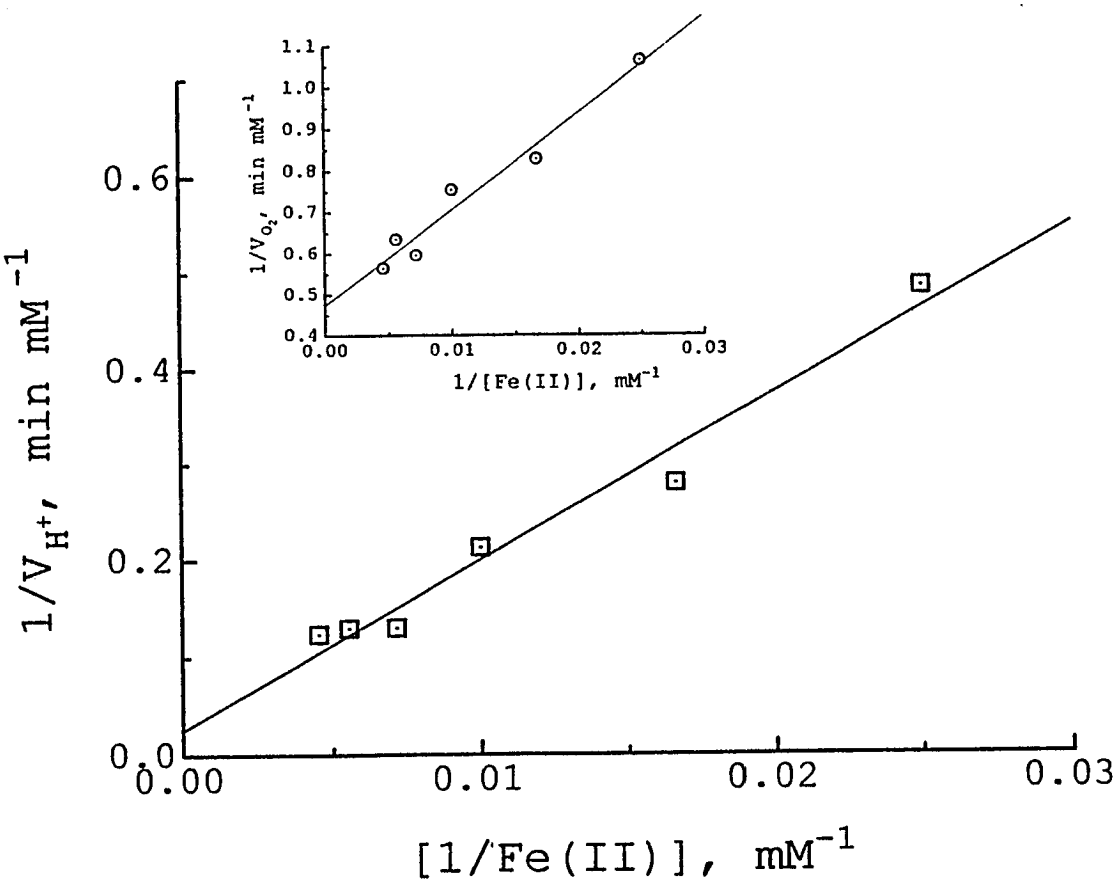

Figure 2.2d: Lineweaver-Burk plots of reciprocal proton release and oxygen consumption (inset) rates *vs.* 1/Fe(II) concentration in HuHF with least-squares straight line fit shown (File name: 080394.org).

= 0.143 ± 0.017 mM, $K_{m,Fe,HuHF}$ = 0.049 ± 0.006 mM, $k_{cat,HoSF}$ = 67 ± 7 min^{-1} and $k_{cat,HuHF}$ = 333 ± 22 min^{-1} (95% confidence level). From the proton release data (Figure 2.2c, 2.2d), $K_{m,Fe,HoSF}$ = 1.06 ± 0.61 mM, $K_{m,Fe,HuHF}$ = 0.673 ± 0.520 mM, $k_{cat,\ HoSF}$ = 1061 ± 610 min^{-1} and $k_{cat,\ HuHF}$ = 6060 ± 4720 min^{-1} were obtained.

The net stoichiometric ratios of Fe(II)/O_2 (curve A) and H^+/Fe(II) (curve B) obtained at completion of the reaction as a function of iron loading to HoSF are shown in Figure 2.3. Values of 1.9 ± 0.2 Fe(II) oxidized per oxygen consumed and 0.6 ± 0.1 H^+ produced per Fe(II) oxidized are obtained at the low Fe(II)/HoSF ratios of 3 to 8. The ratios of Fe(II)/O_2 and H^+/Fe(II) increase with increasing iron loading in ferritin and approach 4 and 2, respectively, at Fe(II)/HoSF ratios greater than 70.

The above stoichiometric relationships between H^+ production and O_2 and Fe^{2+} consumption agree with the net iron oxidation/hydrolysis reaction given by equation 2.5 at low iron loading of the protein and equation 2.9 at high iron loading. However, information on intermediate steps in the reaction is not obtainable from stoichiometric ratios at completion of the reaction. Since this experimental setup has the advantage over other kinetic methods in its ability to monitor oxidation and hydrolysis rates simultaneously, the ratio of initial rates, V_{H+}/V_{O2}, was therefore employed to probe the stoichiometric relationship between H^+ and O_2 during each part of the reaction. Values of V_{H+}/V_{O2} ranging from 1.7

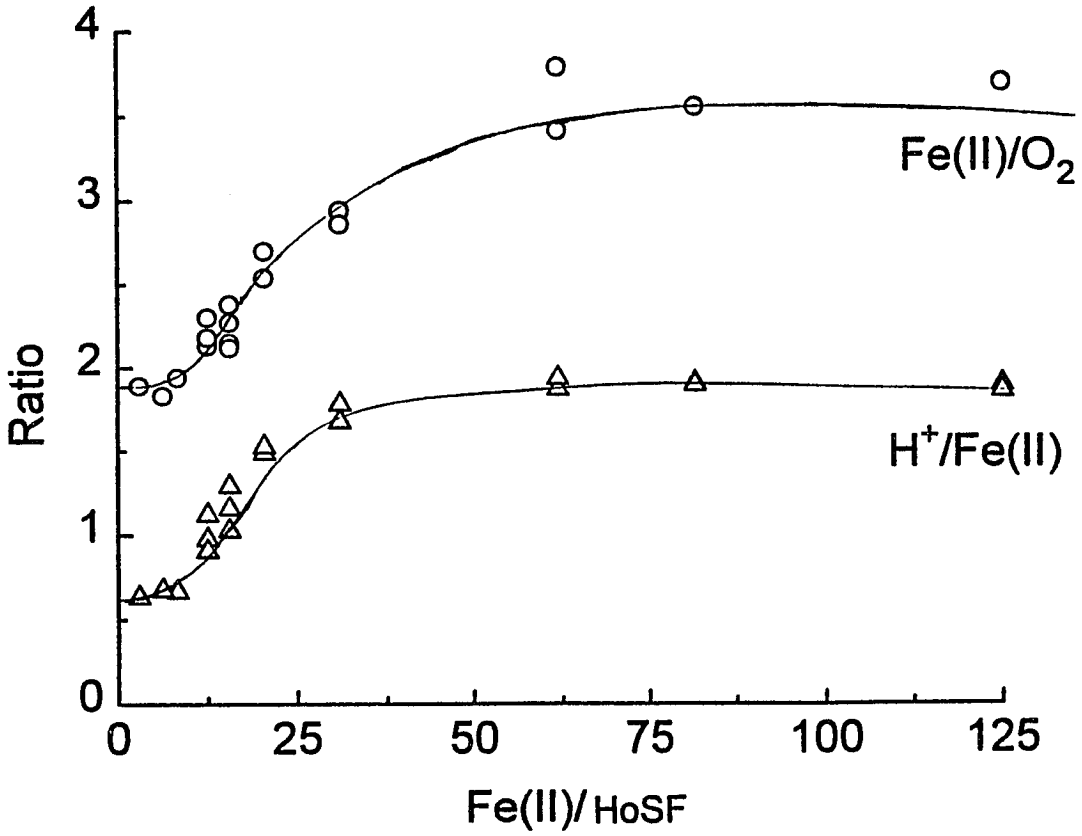

Figure 2.3: Stoichiometries of Fe(II)/oxygen uptake (○) and proton release/Fe(II) concentration (△) as a function of Fe(II) loading in HoSF. Conditions: [Fe(II)] = 125 μM in 0.5 mM MOPS and 0.15N NaCl solution, [HoSF] = 0.25 - 10.0 μM, $[O_2]_0$ = 0.28 mM, $[NaOH]_{stock}$ = 7.60 mM, pH 7.00, 20 °C (File name: 051994.org)

to 5.9 and 1.9 to 5.0 were observed at Fe(II)/HoSF ratios of 10 - 500 (Figure 2.2a, inset) and Fe(II)/HuHF ratios of 50 - 600 (Figure 2.2b, inset), respectively. Values of V_{H+}/V_{O2} = 0.97 ± 0.22 and 1.07 ± 0.28 were obtained at Fe(II)/protein = 0 for HoSF and HuHF, respectively, from extrapolations of the 2nd order polynomial fit to the data shown in Figure 2.2a and 2.2b insets to zero iron concentration. These results imply a stoichiometry of H^+/O_2 = 1 during the initial step of dioxygen reduction at low iron loading of ferritin and a H^+/O_2 ratio of ~6 at high iron loading. Thus, at least two iron oxidation pathways appear to be contributing to the kinetic relationship between oxygen consumption and proton production, depending upon the stage of iron deposition in ferritin, in accord with the existence of protein ferroxidase and mineral surface pathways for iron oxidation observed previously (Sun & Chasteen, 1992; Mayer et al., 1983).

From the stoichiometric and kinetic relationships between Fe^{2+}, O_2, H^+, V_{H+} and V_{O2}, an intermediate step of iron oxidation and dioxygen reduction is thus postulated in equations 2.10 - 2.11 where superoxide is the product of the one electron oxidation of Fe(II).

Fe(II) and dioxygen binding:

$$Fe^{2+} + O_2 + P^z \rightarrow [Fe^{2+}(O_2)P^z]^{z+2} \qquad (2.1)$$

Fe(II) oxidation at the protein active site:

$$[Fe^{2+}(O_2)P^z]^{z+2} \rightarrow [Fe^{3+}O_2^{\cdot-}P^z]^{z+2} \qquad (2.6)$$

Fe(III) hydrolysis at the protein active site:

$$[Fe^{3+}O_2^{\cdot-}P^z]^{z+2} + H_2O \rightarrow [Fe^{3+}(OH)^-P^z]^{z+2} + O_2^{\cdot-} + H^+ \quad (2.10)$$

Fe(III) core formation:

$$[Fe(OH)P^z]^{z+2} + H_2O \rightarrow FeOOH_{core} + P^z + 2H^+ \quad (2.11)$$

Here P represents the protein and Z is the net charge of the protein complex. Reaction 2.1 corresponds to Fe(II) and dioxygen binding to the ferroxidase site of the protein. The Fe(II) bound on the protein is then oxidized by O_2 producing $O_2^{\cdot-}$ and Fe(III) as shown in reaction 2.6. The newly formed Fe(III) then hydrolyzes to release $O_2^{\cdot-}$ and H^+ as given in reaction 2.10. The partially hydrolyzed ferric iron complex from reaction 2.10 then undergoes further hydrolysis and migrates to form the iron core, thus freeing the protein active site for more incoming iron (reaction 2.11).

According to this mechanism, at very low iron loading of the protein (Fe(II)/protein < 8 Fe(II)/HoSF), only Fe(II) oxidation and Fe(III) partial hydrolysis at the protein ferroxidase site is expected with no ferrihydrite core formation, which predicts the stoichiometric relationships of 1 H^+/Fe^{2+} and 1 Fe^{2+}/O_2 according to reactions 2.1, 2.6 and 2.10. These values are different from the values of 0.6 H^+/Fe^{2+} and 1.9 Fe^{2+}/O_2 observed in Figure 2.3. The rationalization is that 1 mole of superoxide formed in equation 2.10 must undergo dismutation (equation 2.4), which consumes 1 mole of proton and produces 1/2 mole of oxygen,

resulting in the net concentration ratios of ~0 H^+/Fe^{2+} and ~2 Fe^{2+}/O_2. The 0.6 H^+/Fe observed may be due to the ferrous iron binding to HoSF as observed by Jacobs et al. (1989b). When iron loading of the protein increases from 10 to 60 Fe(II)/HoSF, formation of the mineral core is anticipated to proceed as described in equation 2.11. The overall reaction for equations 2.1, 2.6, 2.10 and 2.11 is given in equation 2.5, representing the iron ferroxidation pathway. Consequently, the mineral surface iron oxidation pathway (equation 2.9) is also expected to take place at this iron loading capacity, resulting in the stoichiometric ratios of $Fe(II)/O_2$ and $H^+/Fe(II)$ changing from 2 to 4 and 1 to 2, respectively, as observed. When the amount of iron deposition in ferritin increases to more than 70 Fe(II)/HoSF, the Fe^{2+}/O_2, H^+/Fe^{2+} and V_{H+}/V_{O2} ratios approach 4, 2 and 6, respectively (Figure 2.2a, 2.2b, 2.3), suggesting that the iron oxidation is predominantly a mineral surface reaction (equation 2.9) at the iron core.

Figures 2.4A and 2.4B show the rates of iron oxidation and hydrolysis as a function of HoSF and HuHF concentrations, respectively. Plots of V_{H+}/V_{O2} *vs.* iron loading in the range of 25 - 500 Fe(II)/ferritin are displayed in the insets with V_{H+}/V_{O2} values extending from 2.2 to 6.4 for HoSF and 2.9 to 4.1 for HuHF. These results imply that at high iron loading into ferritin (Fe(II)/protein > 500), the iron oxidation is dominated by the mineral surface reaction in HoSF and by the

ferroxidation in HuHF. This finding is consistent with the previous observation when the protein concentrations were held constant but iron concentration varied (Figure 2.2a & 2.2b).

The initial oxidation rate with respect to both HoSF (Figure 2.5, curve B) and HuHF (Figure 2.5, curve D) concentrations are shown to be simple 1st order reactions from the slopes (0.98 ± 0.04 and 0.95 ± 0.04, respectively) of the logarithm plots. A first order hydrolysis reaction (0.89 ± 0.03, Figure 2.5C) with respect to HuHF is also observed in accord with the idea that Fe(III) hydrolysis is controlled by the Fe(II) oxidation rate on the protein. Proton release in horse spleen ferritin, however, showed an apparent reaction order of 0.59 ± 0.04 (Figure 2.5A), possibly because the stoichiometry of the reaction changes between 4 H^+/O_2 in equation 2.5 and 8 H^+/O_2 in equation 2.9 in the Fe(II) loading range of 15 to 250 Fe(II)/HoSF at the HoSF concentrations of the experiment (Figure 2.2a & 2.4a).

Iron Deposition in HuLF

Figure 2.6 shows the effect of four different HuLF concentrations at a fixed Fe(II) concentration on both ferrous ion oxidation (top) and ferric ion hydrolysis (bottom). Iron autoxidation is observed in the absence of HuLF (curve a) and at an Fe(II)/HuLF ratio of 875 (curves b) while the HuLF was seen to accelerate iron oxidation at Fe(II)/HuLF ratios of 300 or less (curves c, d & e). Hydrolysis appears to be limited

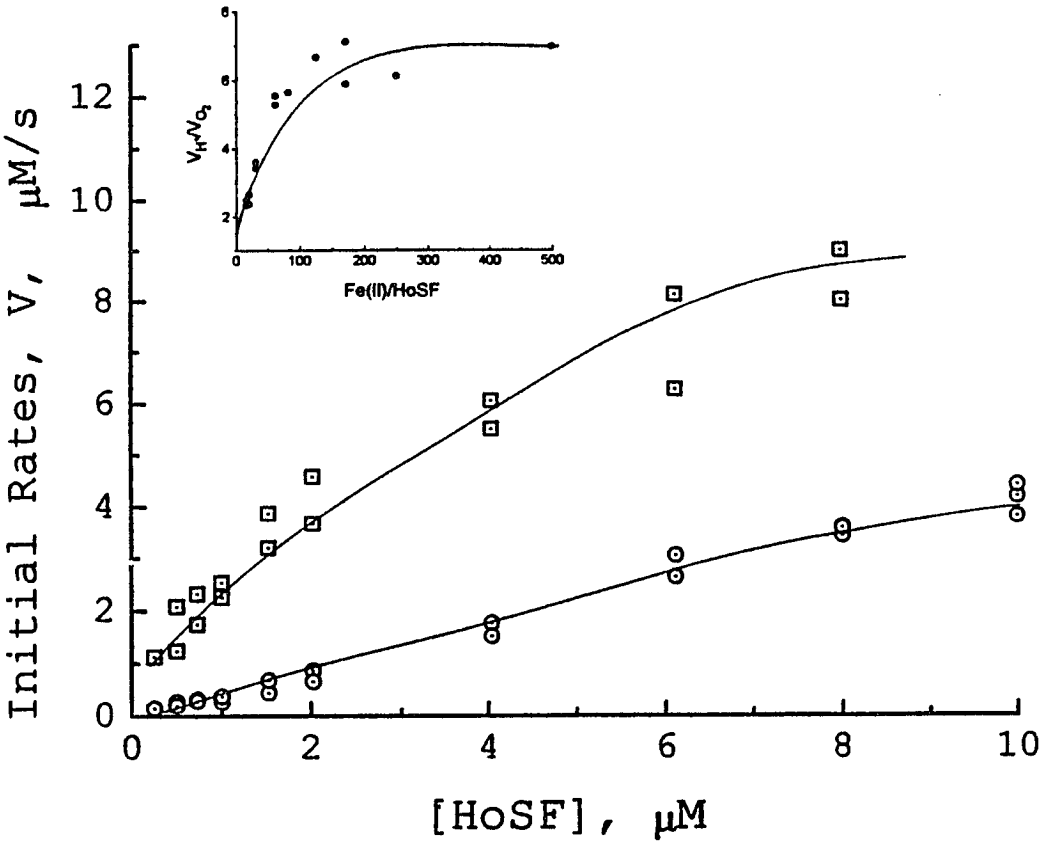

Figure 2.4a: Initial rates of iron oxidation (⊙) and hydrolysis (⊡) as a function of HoSF concentration. Conditions are the same as given Figure 2.3 (File name: 051994.org) **Inset:** Ratio of initial rates of hydrolysis and oxidation as a function of iron loading to HoSF.

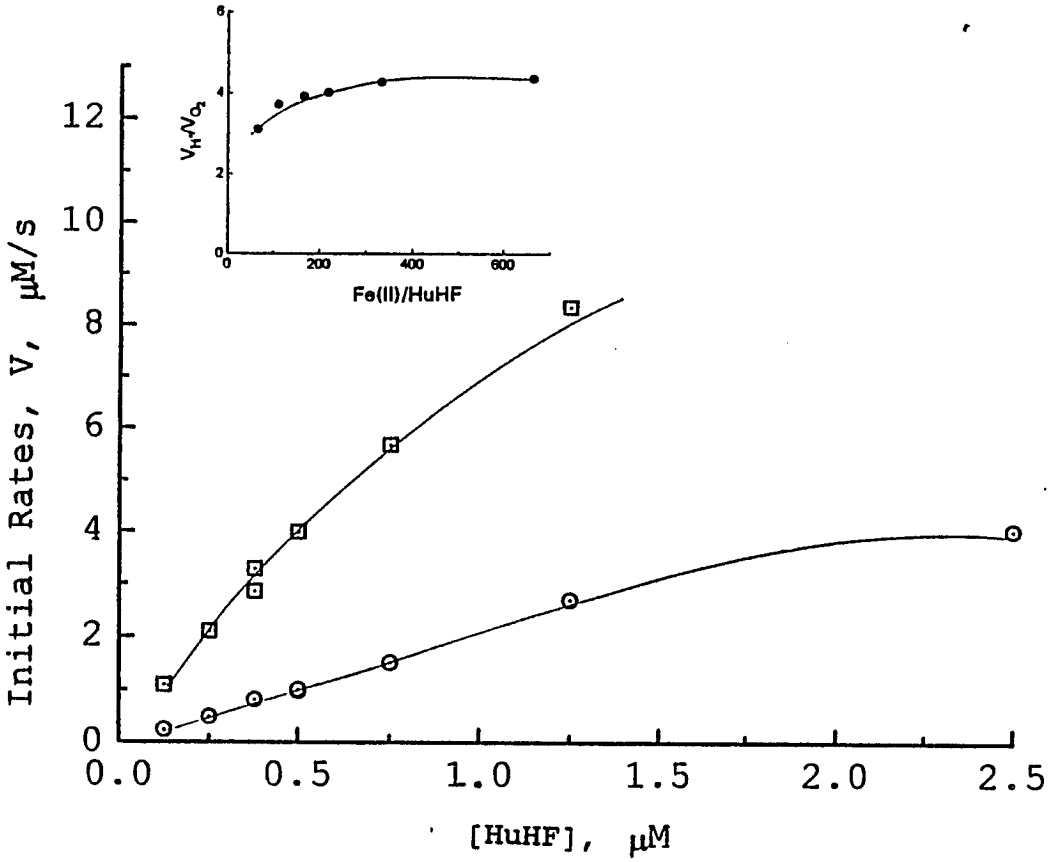

Figure 2.4b: Ratio of initial rates of iron oxidation (⊙) and hydrolysis (⊡) as a function of HuHF concentration. Conditions: [Fe(II)] = 83 μM in 0.5 mM MOPS and 0.15N NaCl solution, $[O_2]_0$ = 0.28 mM, $[NaOH]_{stock}$ = 4.99 mM, pH 7.00, 20 °C (File name: 080894.org) **Inset:** Ratio of initial rates of iron oxidation and hydrolysis as a function of iron loading in HuHF.

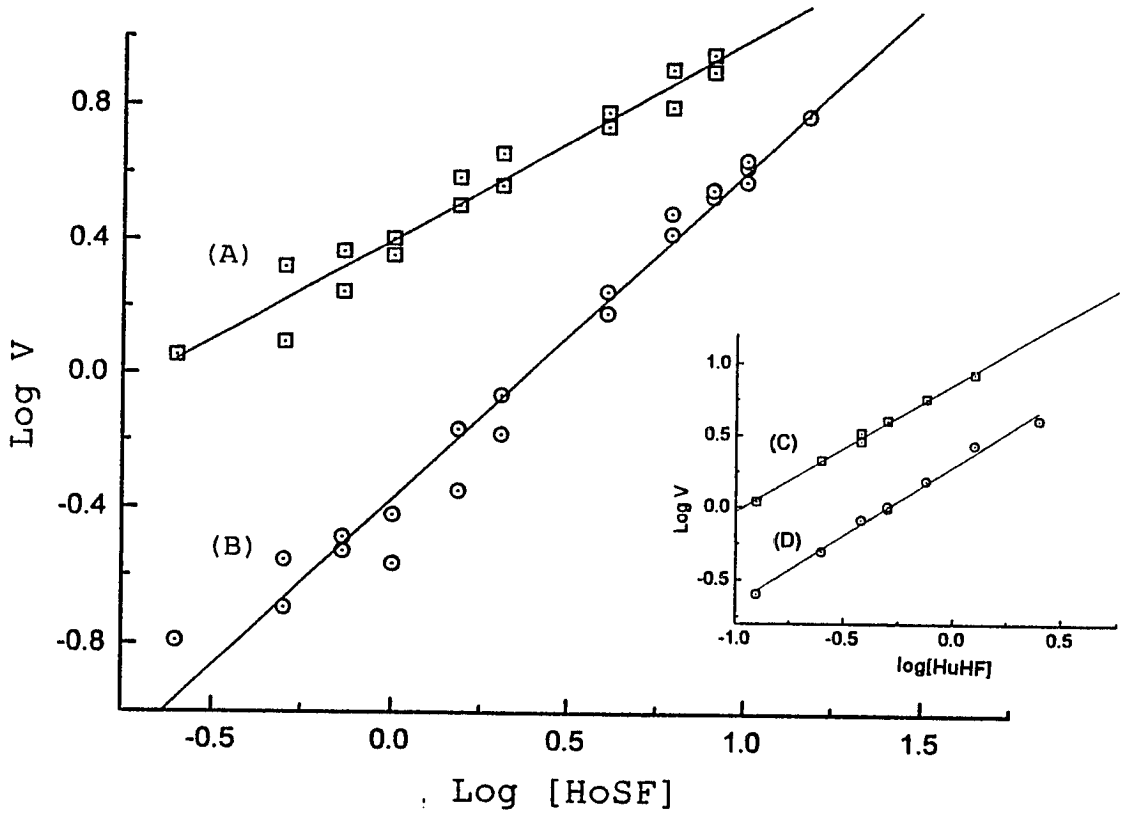

Figure 2.5: A first order (slope = 0.98 ± 0.04) reaction of iron oxidation (A) and a fraction order reaction (slope = 0.59 ± 0.04) of hydrolysis (B) with respect to HoSF concentration. Conditions are the same as Figure 2.4a (File name: 051994.org) **Inset:** First order (0.95 ± 0.04) reactions of iron oxidation (C) and hydrolysis (0.89 ± 0.03) (D) with respect to HuHF concentration. Conditions are the same as given in Figure 2.4b (File name: 080894.org)

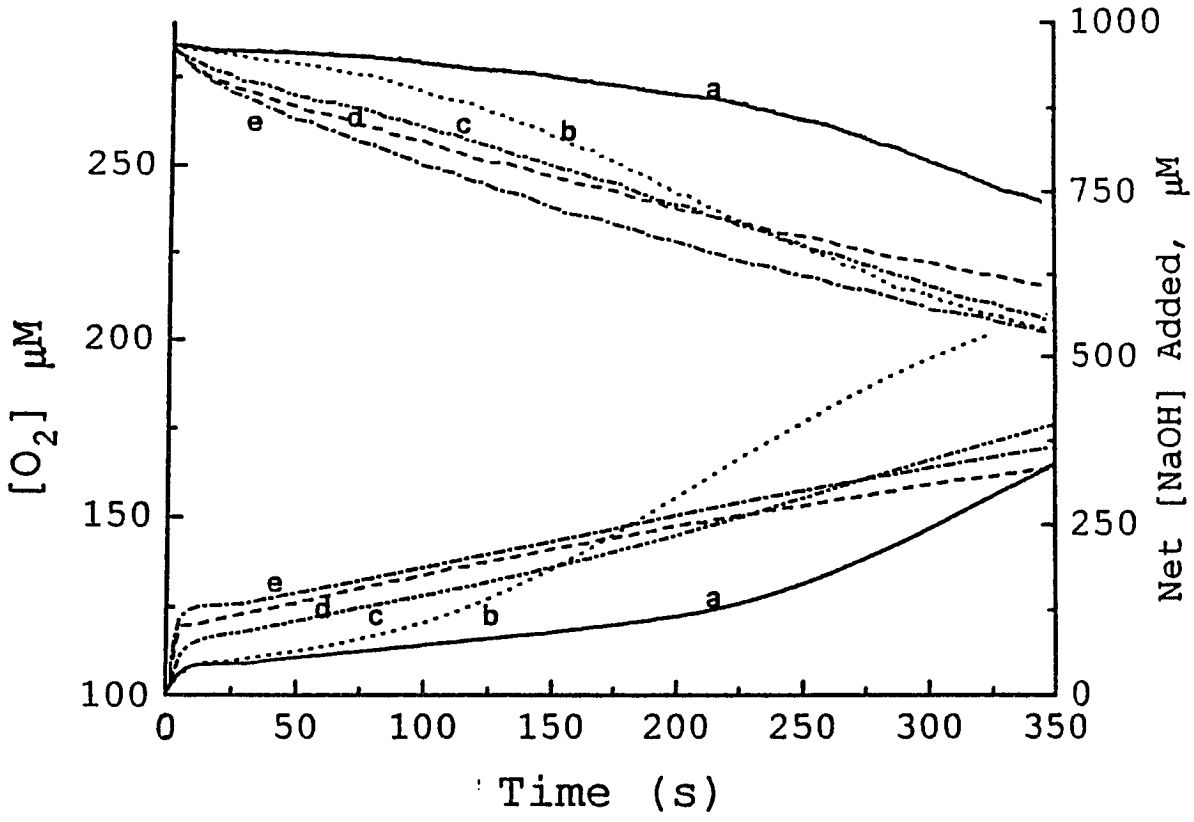

Figure 2.6: Oxygen consumption as a function of time in the absence (a) and in the presence of HuLF (b - e). Conditions: [Fe(II)] = 430 μM in 0.15 M NaCl and 0.5 mM MOPS, pH = 7.00, Fe(II)/HuLF = 875 (b), 300 (c), 150 (d) and 100 (e), [NaOH] = 9.96 mM, $[O_2]_0$ = 0.28 mM, 20 °C (File names: original data, 08100894, 08100594; 08100494; 0810794, Final plot, 091994.org)

by oxidation in all instances as the general shape of the corresponding oxidation and hydrolysis curves are the same.

The initial proton production within the first 10 - 15 seconds of the reaction shown in the bottom part of the Figure 2.6 is seen to increase proportionally with the HuLF concentration. Therefore, a more complete study using HuLF concentrations of 1 - 4 μM and iron loadings of 25 - 400 Fe/protein was undertaken to examine the initial release of protons, after subtracting the pH drop caused by free acid in $FeSO_4$ (Figure 2.7). A release of 8 - 10 protons is observed at an iron concentration of less than 40 Fe(II)/protein, which then increases with higher iron loading. At 200 Fe(II)/HuLF, the number of protons released reaches a plateau at ~32 H^+/HuLF. Anaerobic additions of Fe(II) to HuLF also generated the same amount of H^+/HuLF in the first 15 seconds of the reaction, suggesting that the initial production of protons originates from the ferrous iron binding to HuLF apoprotein prior to iron oxidation. The 32 H^+/HuLF produced is difficult to interpret, however, it may indicate that the ferrous binding to HuLF occurs at the twenty four individual subunits as well as at the eight 3-fold channels.

Interestingly, a study of Fe(II) oxidation in HuLF at iron loadings of 40 - 50 Fe(II)/HuLF showed very slow Fe(III) hydrolysis (Figure 2.8A, bottom) compared to Fe(II) oxidation (Figure 2.8A, top). When iron loading increases to 100 Fe(II)/HuLF or more, hydrolysis becomes significant and the

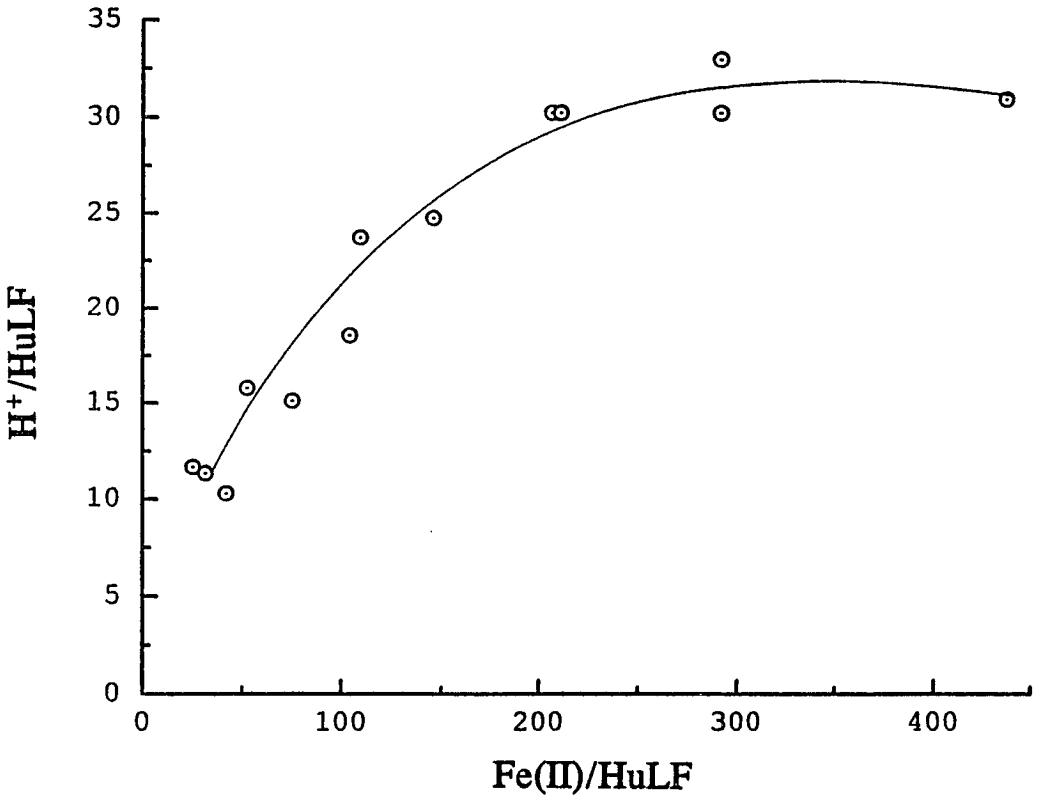

Figure 2.7: Initial protons released as a function of iron loading in HuLF at completion of the reaction. Conditions: [HuLF] = 1 - 4 μM, [Fe(II)] = 62 - 620 μM in 0.15 N NaCl and 0.5 mM MOPS, pH 7.00, 20°C. File name: HrLF.org

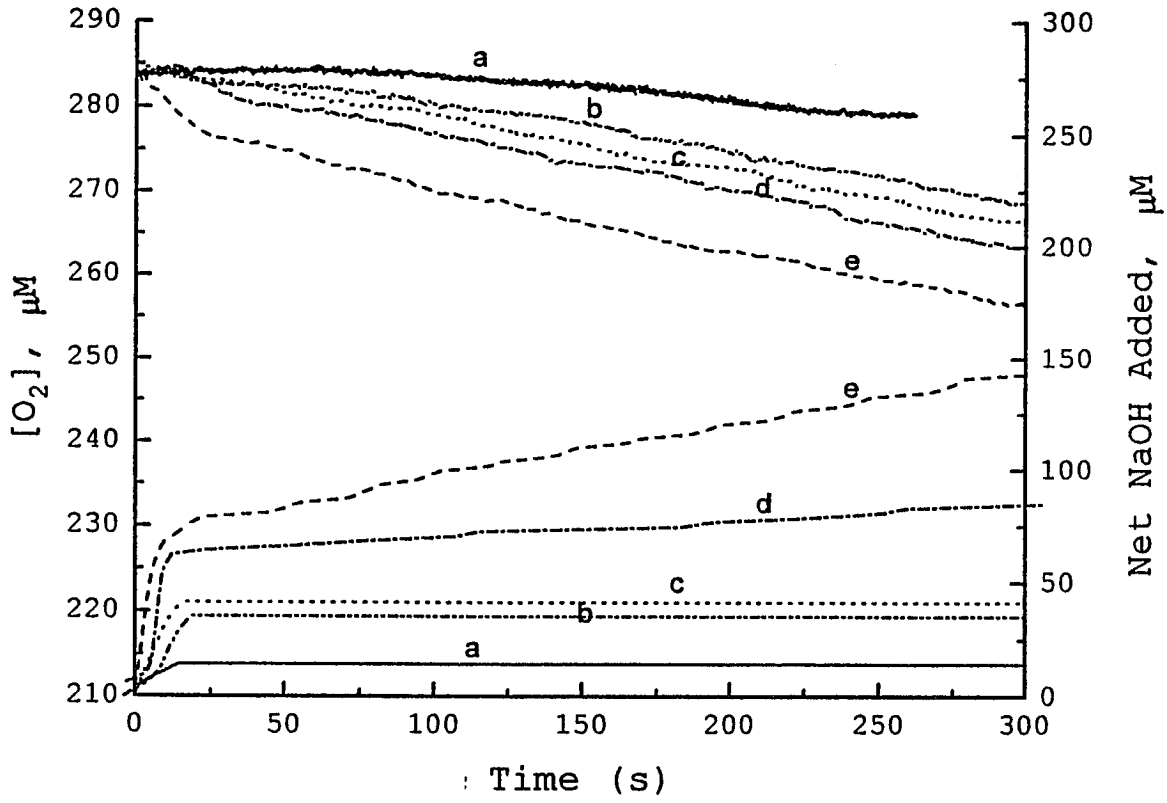

Figure 2.8a: Oxygen consumption and proton release as a function of time with (b - e) and without the presence of HuLF (a). Conditions are the same as Fig 6 except: [HuLF] = 3.0 μM, Fe(II)/HuLF = 25 (b), 41 (c), 75 (d) and 100 (e). (File names: original data, 08220694, 08100194; 08220994; 0810294, final plot, 092094.org)

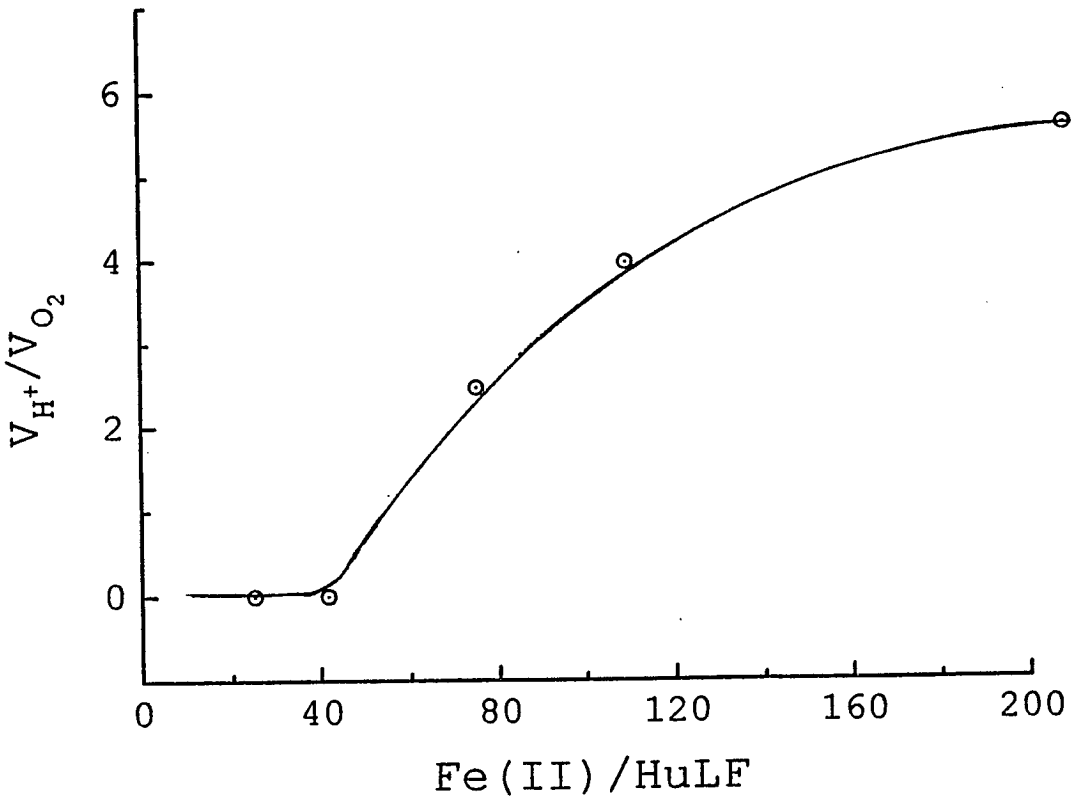

Figure 2.8b: Ratio of reaction rates of iron oxidation and hydrolysis as a function of iron loading into HuLF. Conditions are the same as given in Fig 2.8a. (File names: 081094.org)

ratio of V_{H+}/V_{O2} approaches ~6 (Figure 2.8B), following the mineral surface reaction. The data suggest that two types of iron oxidation occur in HuLF. It is possible that the initial 40 - 50 Fe(II)/HuLF, corresponding to 2 Fe(II)/subunit, are bound and oxidized at the protein sites but not hydrolyzed while subsequent Fe(II) oxidation takes place directly at the surface of the previously formed Fe(III) cluster.

The Effect of Fe(III) core

The effect of Fe(III) core on the Fe(II) oxidation kinetics has been examined previously (Sun & Chasteen, 1992). The presence of a preexisting iron core was observed to accelerate the iron oxidation in HoSF only at iron loading increments of 50 Fe(II)/protein or more, a situation where the ferroxidase pathway is kinetically saturated. An experiment was therefore conducted to investigate the influence of the presence of an iron core on the rate of iron hydrolysis using Fe(II)/protein ratios of 28 and 82 (Figure 2.9). Acceleration of the hydrolysis rate (Figure 2.9, inset) is evident with both iron increments even though increasing core size at 28 Fe/protein decreases the iron oxidation rate slightly. It is possible that iron mineral surface oxidation has taken place even at Fe/HoSF of 50. But it was only detected through the rate of proton release, because the increase in proton production in iron mineral surface oxidation ($8H^+/O_2$, equation 2.9) compared to iron ferroxidation ($4H^+/O_2$, equation 2.5) may

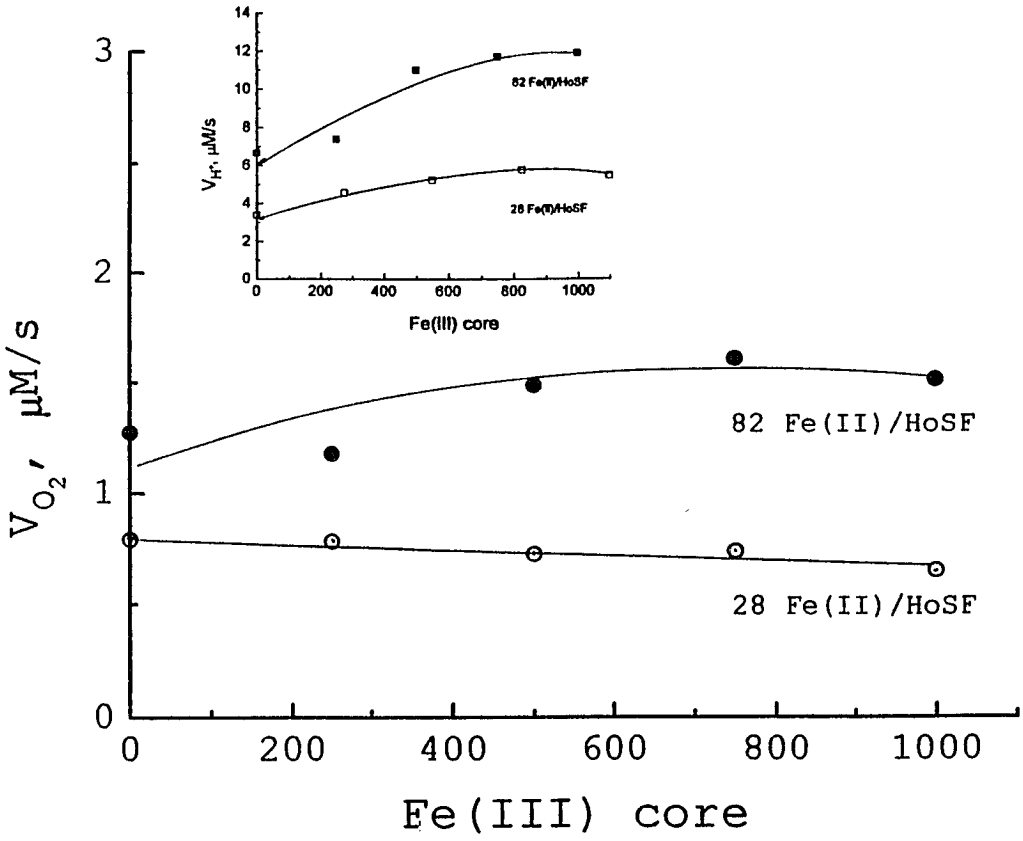

Figure 2.9: Effects of Fe(III) core size on initial iron oxidation (⊙) and hydrolysis (inset, (□)) rates in HoSF with 28 (open) and 82 (solid) Fe(II) increments. Conditions [HoSF] = 3 µM, [NaOH] = 10.0 mM in 0.15 N NaCl and 0.5 mM MOPS pH = 7.00, 20°C. (File name: 050694.org)

sensitize the detection for iron hydrolysis. A change from iron oxidation at the ferroxidase site to mineral surface sites is observed at both iron/protein ratios as evidenced by the increasing V_{H+}/V_{O2} ratio from 4 to 8 with increasing iron core size (Figure 2.10).

The influence of the iron core on the kinetics of HuLF was also investigated with 50 Fe(II)/HuLF added to the samples containing different ferric cores. Figure 2.11 shows that the rate increases for both oxidation (curve A) and hydrolysis (curve B), while the V_{H+}/V_{O2} ratio of approximately 8 remains unchanged (inset), suggesting that the mineral surface reaction is the dominant reaction throughout the core formation process. Here dioxygen is reduced to water (equation 2.9).

Terbium Inhibition

Terbium(III) has often been used as a probe to investigate the iron binding sites of ferritin, resulting in the discovery of the ferroxidase, intermediate and nucleation sites (Treffry et al., 1977; Chasteen & Theil, 1982; Wardeska et al., 1986; Lawson et al., 1991; Treffry et al., 1992). In order to further understand which site(s) is responsible for terbium inhibition of iron deposition in HoSF, three different concentrations of terbium (0, 12 and 24 Tb/protein) were used along with 10 - 70 Fe(II)/protein in a study of the reaction rate changes in iron oxidation and hydrolysis. Figure 2.12

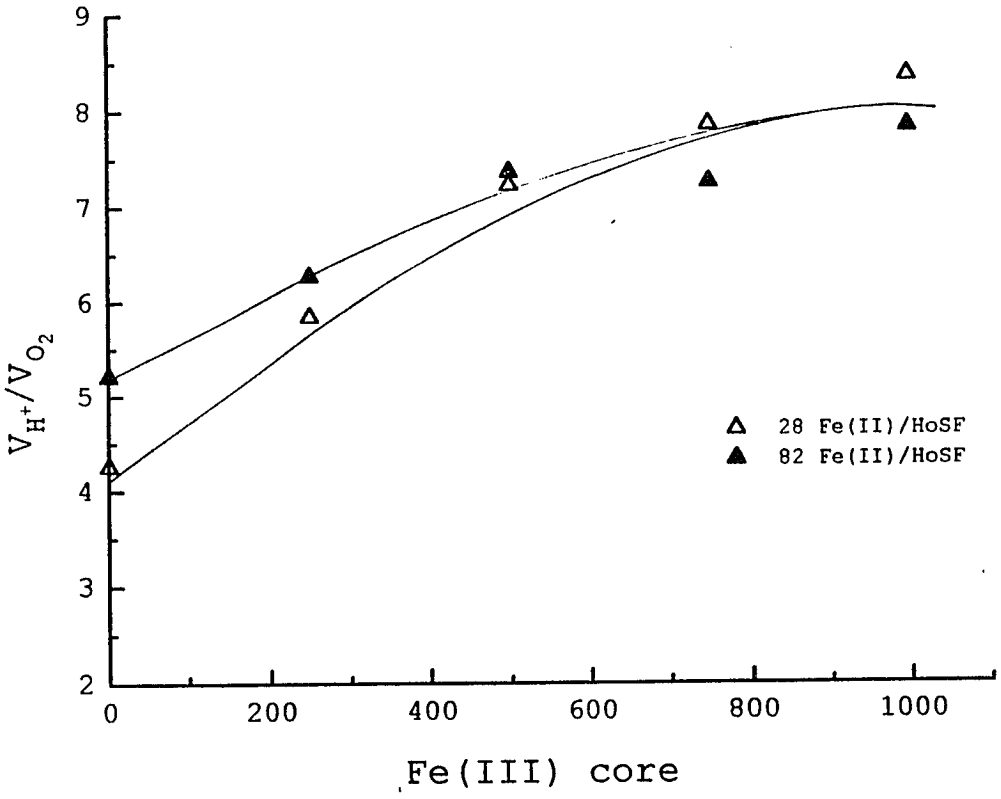

Figure 2.10: Ratio of initial hydrolysis and oxidation rates as a function of ferric core size in HoSF, where the 28 (△) and 82 (▲) Fe(II) increments. Conditions are the same as Figure 2.9. (File name: 050494.org)

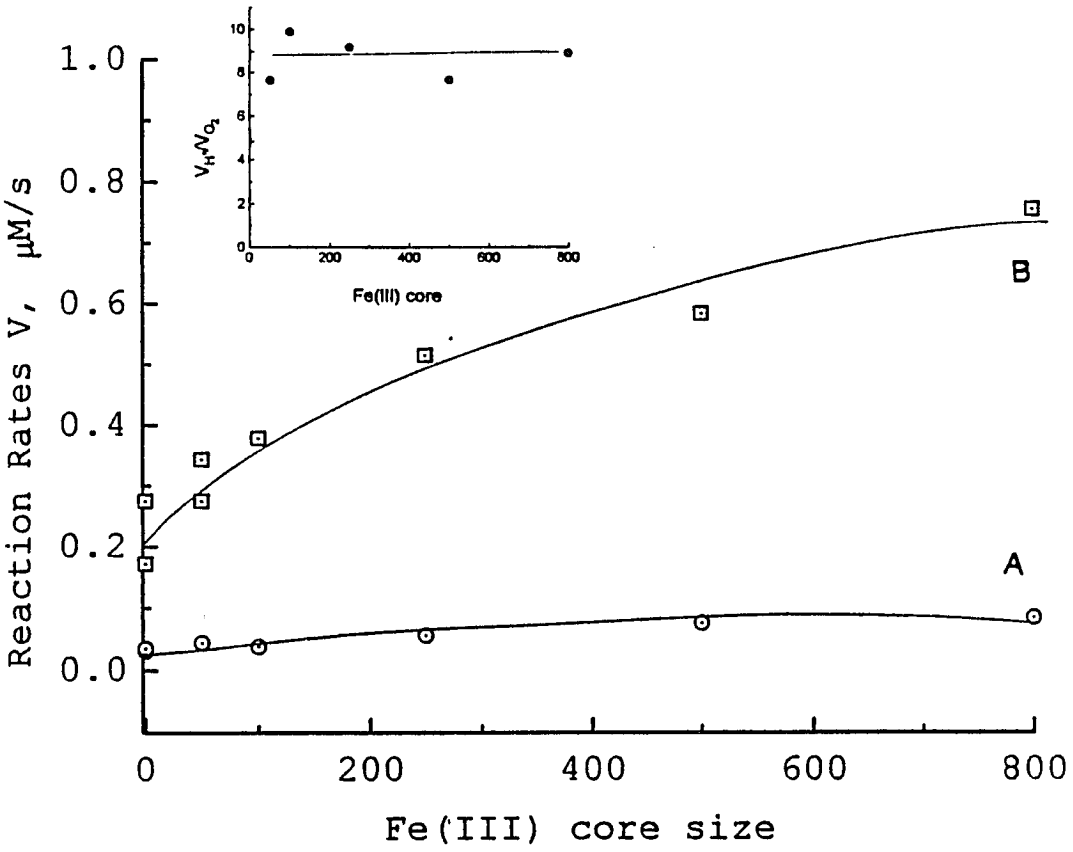

Figure 2.11: Influence of core size on rates of iron oxidation (⊙) and hydrolysis (⊡) in HuLF. Conditions are the same as given in Figure 2.8 except [HuLF] = 3 μM and [Fe(II)] = 150 μM. File name 090494.org **Inset:** Ratio of hydrolysis and oxidation rates as a function of ferric core in HuLF. Conditions are the same as given in Figure 2.11.

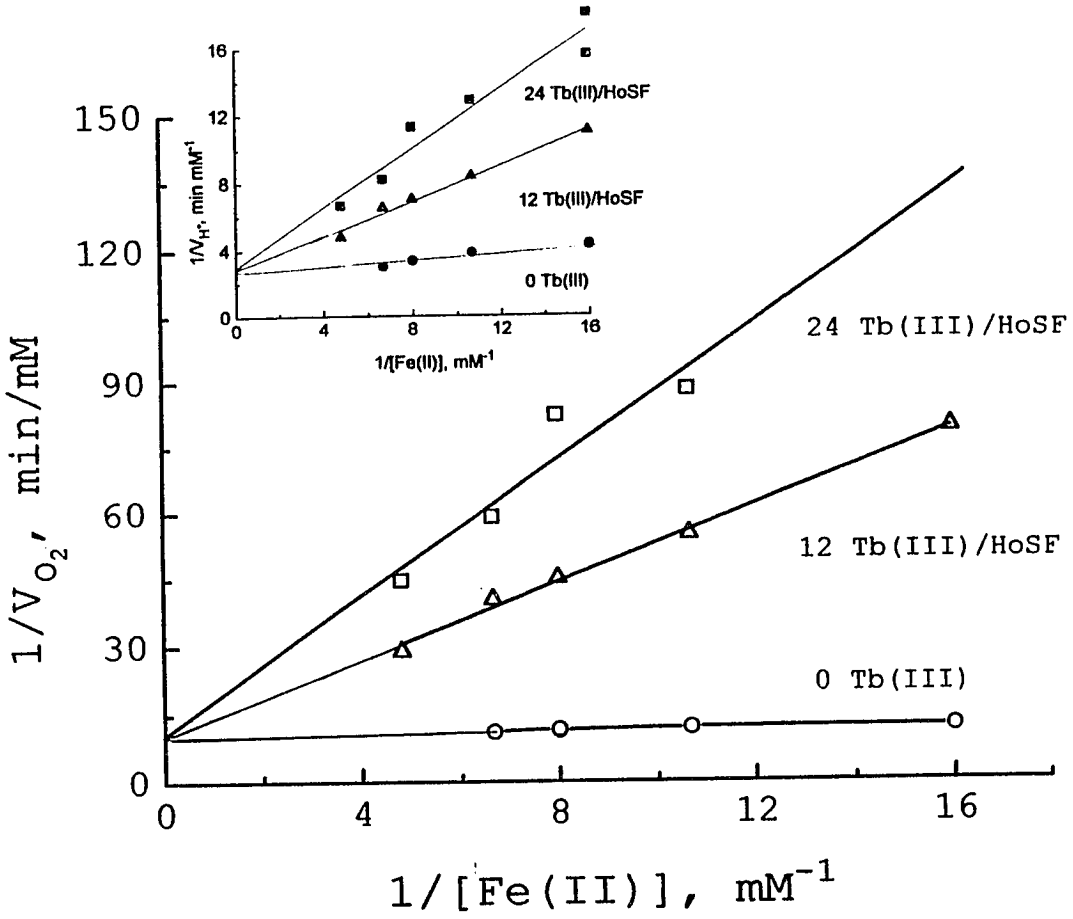

Figure 2.12: Lineweaver-Burk plots of terbium inhibition for Fe(II) oxidation (symbols with open centers) and hydrolysis (inset, symbols with solid centers) in HoSF with the fixed Tb(III)/protein ratios of 0 (○), 12 (△) and 24 (□). Conditions are the same as given in Figure 2.1C.
(File name: 050594.org)

shows the double reciprocal plots of oxygen consumption rate and proton release rate (inset) *vs.* iron concentration in the presence of terbium. Both sets of curves demonstrate competitive inhibition patterns with apparent inhibition constants of $K_{I,O2}$ = 2.86 ± 0.25 μM and $K_{I,H}$ = 13.5 ± 1.6 μM calculated from an equation $K_m^{Tb} = K_m (1 + [Tb]/K_I)$ (Mathews & van Holde, 1990), possibly due to the terbium binding at the 3-fold channels as observed in HuHF (Treffry et al., 1993). The difference in $K_{I,O2}$ and $K_{I,H}$ is probably caused by the different $K_{m,O2}$ and $K_{m,H+}$ values obtained for oxidation and hydrolysis as described earlier (Figure 2.2). The corresponding V_{H+}/V_{O2} ratios are plotted as a function of iron loading in Figure 2.13. A V_{H+}/V_{O2} ratio of ~8 is observed at minimum iron core size of 10 - 20 Fe(III)/protein, which then decreases to 6 as the iron loading increased to Fe(II)/protein = 70, probably due to the replacement of terbium by iron at the ferroxidase site and increasing the amount of Fe(II) oxidized via the ferroxidation pathway (Figure 2.13).

pH Dependence

Figure 2.14 shows the pH dependence of the oxygen consumption rate (Figure 2.14A) and proton release rate (Figure 2.14B) in HoSF with an Fe(II)/protein ratio of 31. Increases in the rates of oxygen consumption and proton release with increasing pH were observed in the pH range of 6 - 8. After subtracting the iron autoxidation reaction

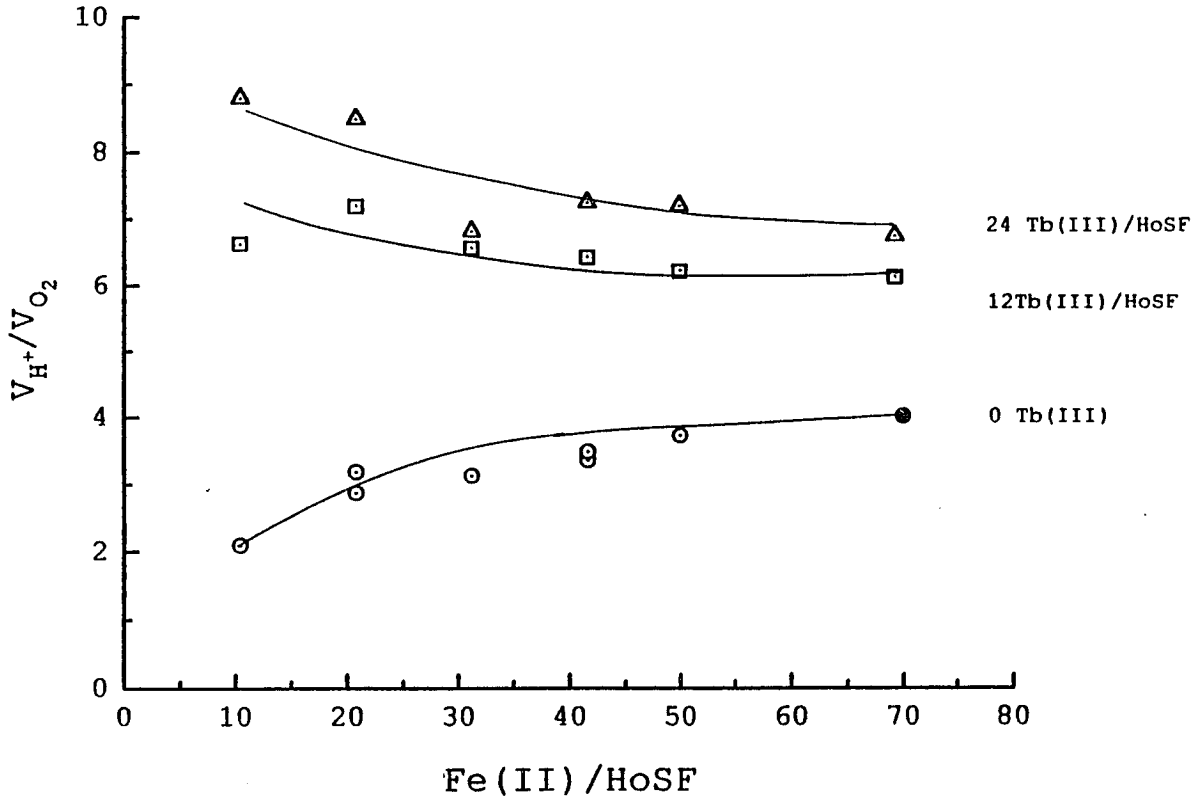

Figure 2.13: Ratio of initial oxidation and hydrolysis rates as a function of iron loading in the absence (⊙) and in the presence of 12 (▵) and 24 (⊡) Tb(III)/protein. Conditions are the same as given in Figure 2.12 except the (•) is performed at [HoSF] = 1.5 μM (File name: 050594.org).

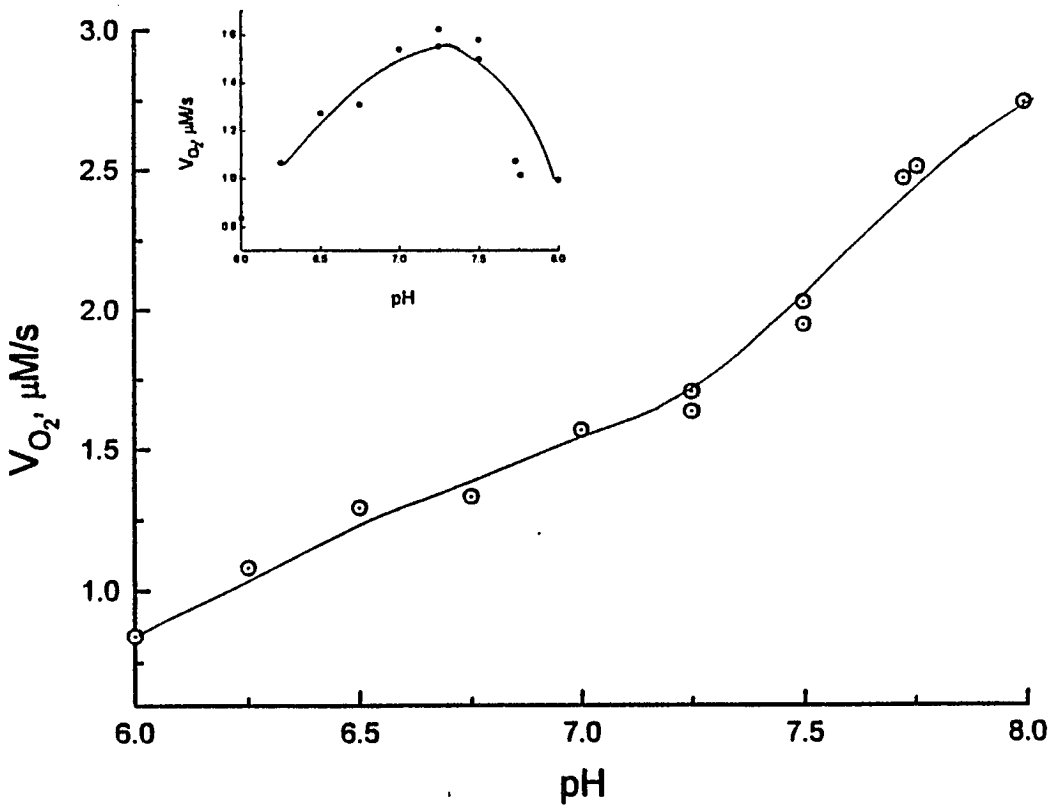

Figure 2.14a: pH dependence of initial Fe(II) oxidation rate in HoSF. Conditions are the same given as in Figure 2.9 except [HoSF] = 4 μM, [Fe(II)] = 125 μM, [NaOH] = 7.8 mM (File names: 051794.org) **Inset:** pH dependencies of initial Fe(II) oxidation rate in HoSF after subtraction of the iron autoxidation rate in the absence of protein. Conditions are the same as given in Figure 2.14a (File names: 051794.org)

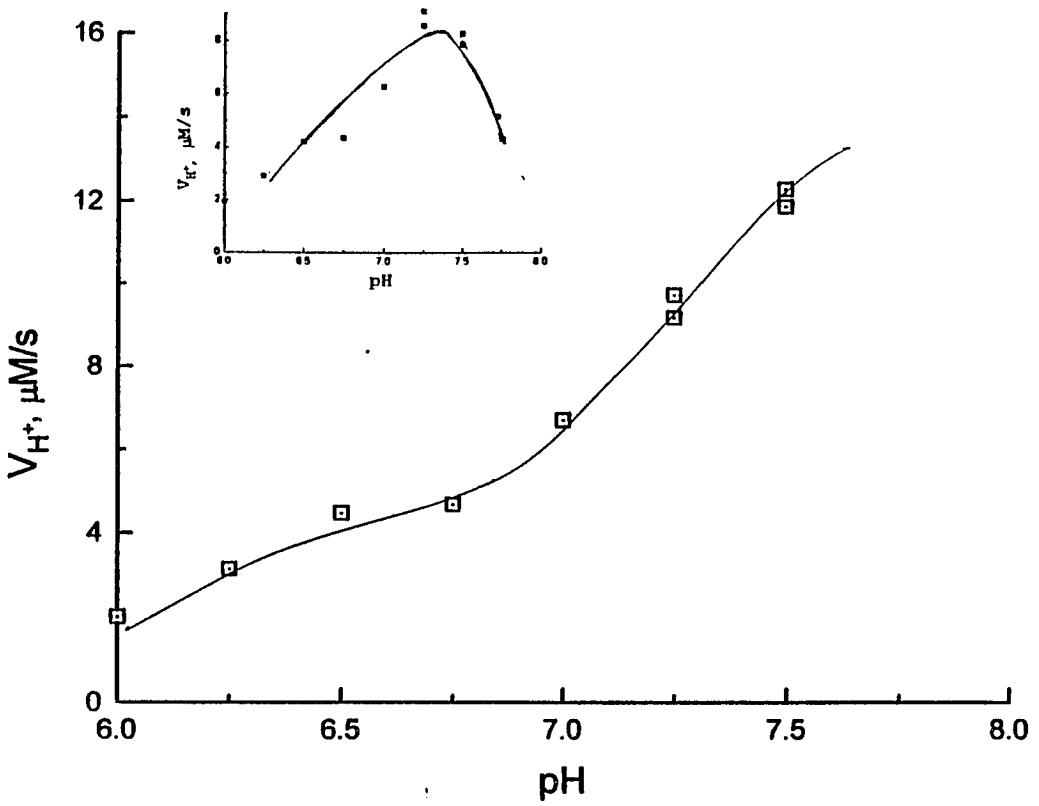

Figure 2.14b: pH dependencies of initial Fe(II) hydrolysis rate in HoSF. Conditions are the same as given in Figure 2.14 (File names: 051794.org) **Inset:** pH dependencies of initial Fe(II) hydrolysis rate in HoSF after subtract the iron autoxidation in the absence of protein. Conditions are the same as Figure 2.14a (File names: 051794.org)

obtained with buffer alone, a bell shaped rate curve with increasing pH was observed with maximum reaction rates obtained at pH ~7.2 (Figure 2.14 insets).

Both oxidation (Figure 2.15) and hydrolysis (Figure 2.15, inset) rates in HuHF showed an apparent 2-phase pH dependency curve. The V_{H+}/V_{O2} values ranged from 2 - 4 at pH 6 - 7 and 4 - 8 at pH 7 - 8 (Figure 2.16) and are in accord with both iron ferroxidation and autoxidation occurring above pH 7.

Phosphate Effect

Phosphate is one of the components of the ferritin core (Theil, 1987). Although phosphate appears to be only surface adsorbed and in disordered regions of the ferric crystalline core (Treffry et al., 1987; Theil, 1987), it is still an interesting question whether or not inorganic phosphate (P_i) plays a role in the kinetics of iron oxidation. Thus, different phosphate concentrations ranging from 0 - 4.1 P_i/Fe(II) were used to examine the effect of P_i on the rates of iron oxidation (A) and hydrolysis (B) in HoSF at iron loading of 49 Fe(II)/protein (Figure 2.17). However, no significant effect on the rates of either iron oxidation or hydrolysis was observed under the experimental conditions, arguing against a role for phosphate in the initial stages of core formation.

HuHF and 222 Mixture

The coexistence of H and L subunits is biologically

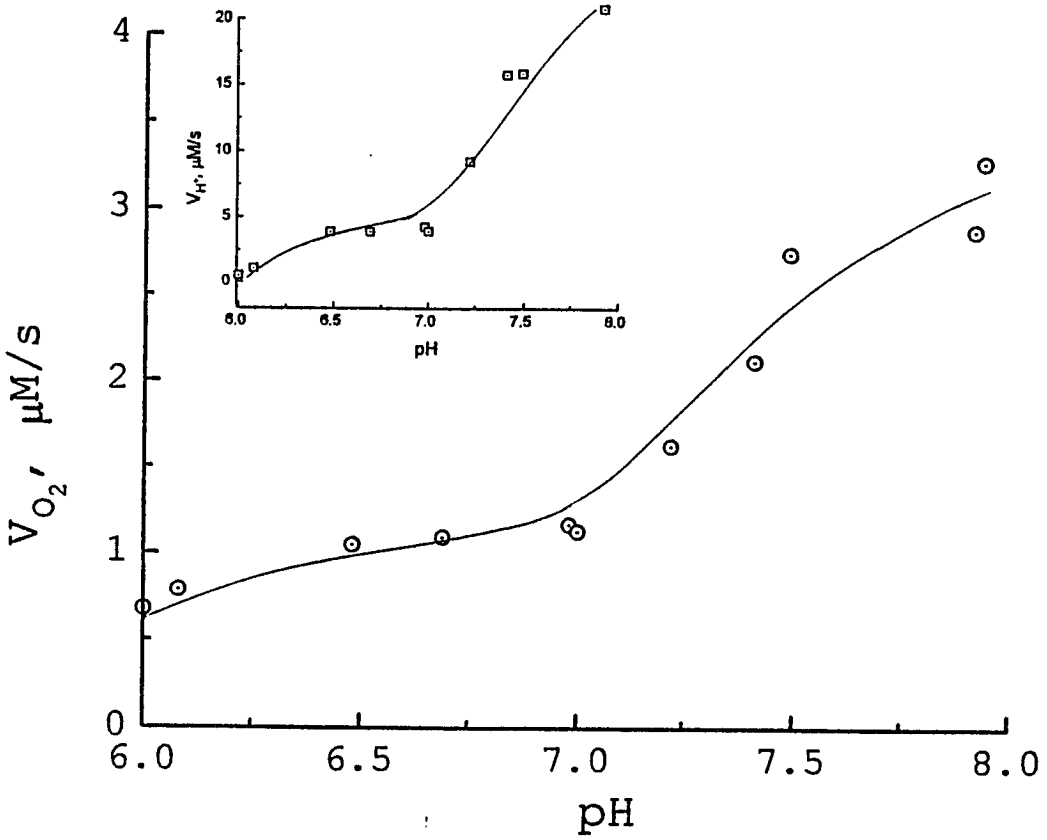

Figure 2.15: pH dependencies of initial Fe(II) oxidation (⊙) and hydrolysis (inset, ⊡) reactions in HuHF at an Fe(II)/protein ratio of 278. Conditions are the same as Figure 2.2b except [Fe(II)] = 105 μM (File names: 080494.org)

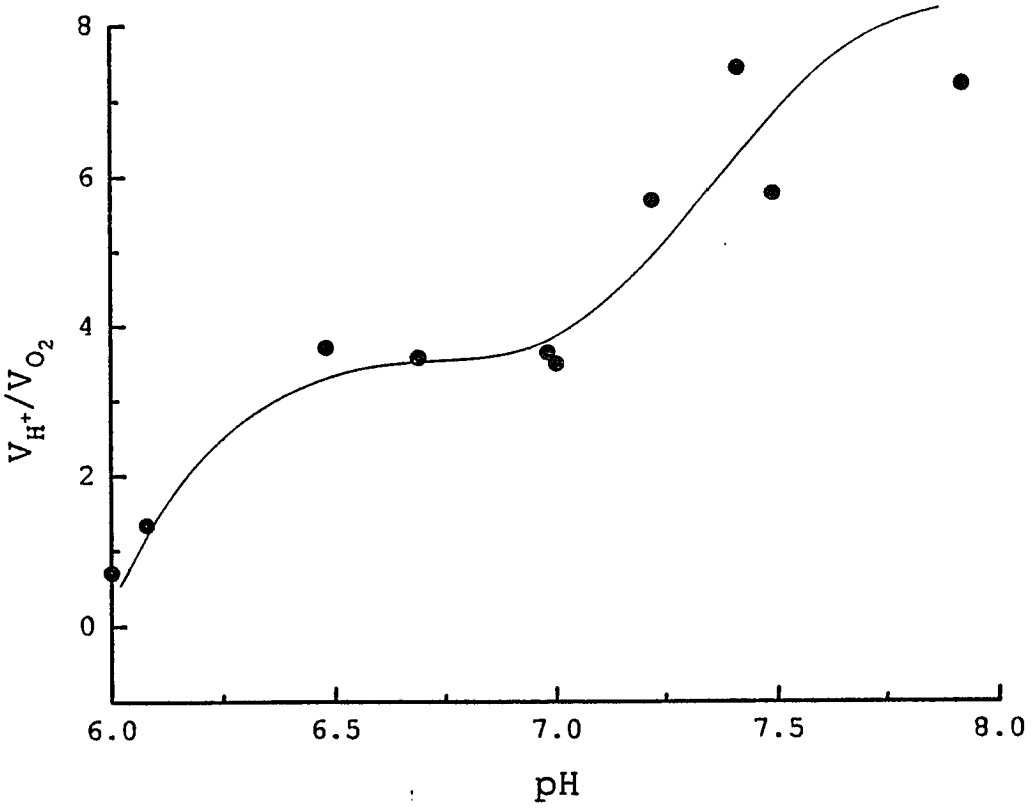

Figure 2.16: Ratio of initial rates of iron oxidation and hydrolysis in HuHF as a function of pH at an Fe(II)/HuHF of 278. Conditions are same as Figure 2.15 (File name: 080494.org)

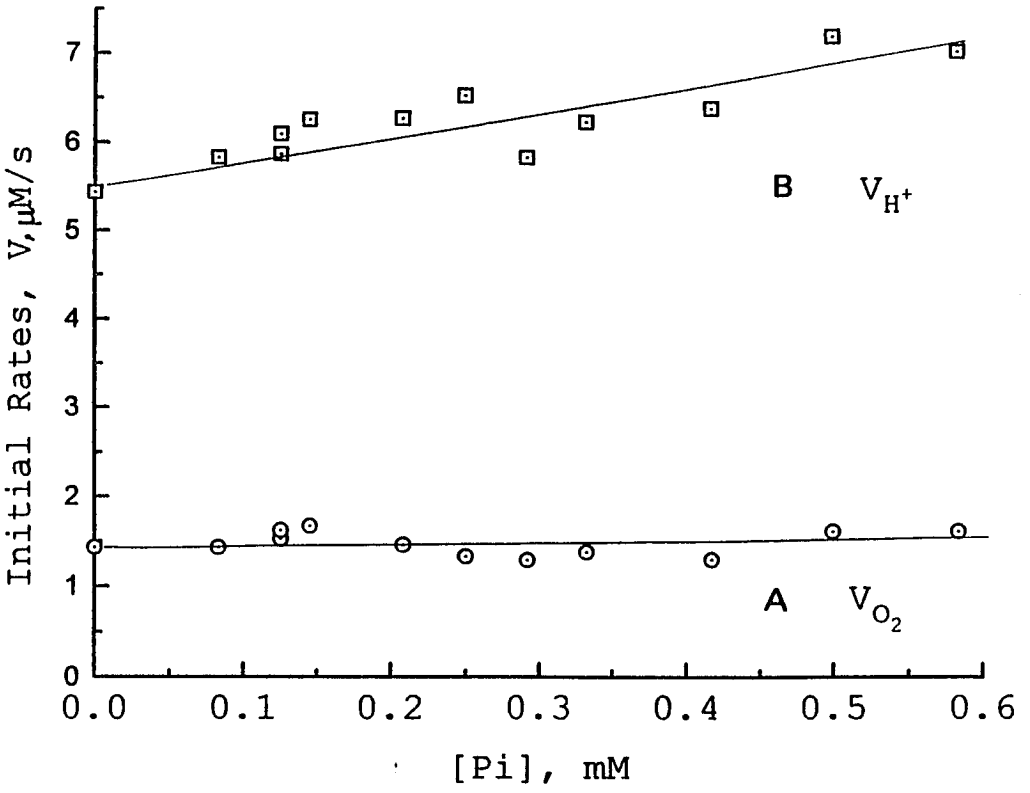

Figure 2.17: Effects of phosphate on initial rates of iron oxidation (⊙) and hydrolysis (⊡) reactions. Conditions are the same as Figure 2.1C except $[NaOH]_{stock}$ = 7.97 mM, [Fe(II)] = 0.146 mM at an Fe(II)/HoSF of 49, P_i/Fe(II) from 0.5 to 4.0. (File name: 042994.org)

favored in nature (Levi et al., 1992; Andrews et al., 1992). A study was therefore conducted to examine the role of the ferroxidase site in "synthetic" ferritins of mixed H an L subunit composition. The 222 protein, an H-chain ferroxidase site mutant with Glu-62 and His-65 being replaced by Lys and Gly as in the L-chain, respectively, has been shown not only to greatly diminish the catalytic capability of HuHF toward iron oxidation but also to form a core that more closely resembles that in HuLF (Bauminger et al., 1991). A series of synthetic ferritins composed of HuHF and 222 mixtures was therefore studied. Both rates of iron oxidation and hydrolysis appear to increase with increasing HuHF content in the mixed protein polymers, presumably due to the increase in total ferroxidase sites in the protein (Figure 2.18). The reaction rates normalized to the number of ferroxidase sites present, however, are independent of the H-chain composition of the protein except at 100% H-chain (Figure 2.18, inset). This finding suggests that the ferroxidase site is the only influential site responsible for the rate of iron oxidation and hydrolysis in the "synthetic" ferritins.

Discussion

In this work, the kinetics of iron deposition in different ferritins has been examined with respect to both iron oxidation and hydrolysis reactions. The stoichiometric and kinetic relationships of O_2, H^+ and Fe^{2+} have provided

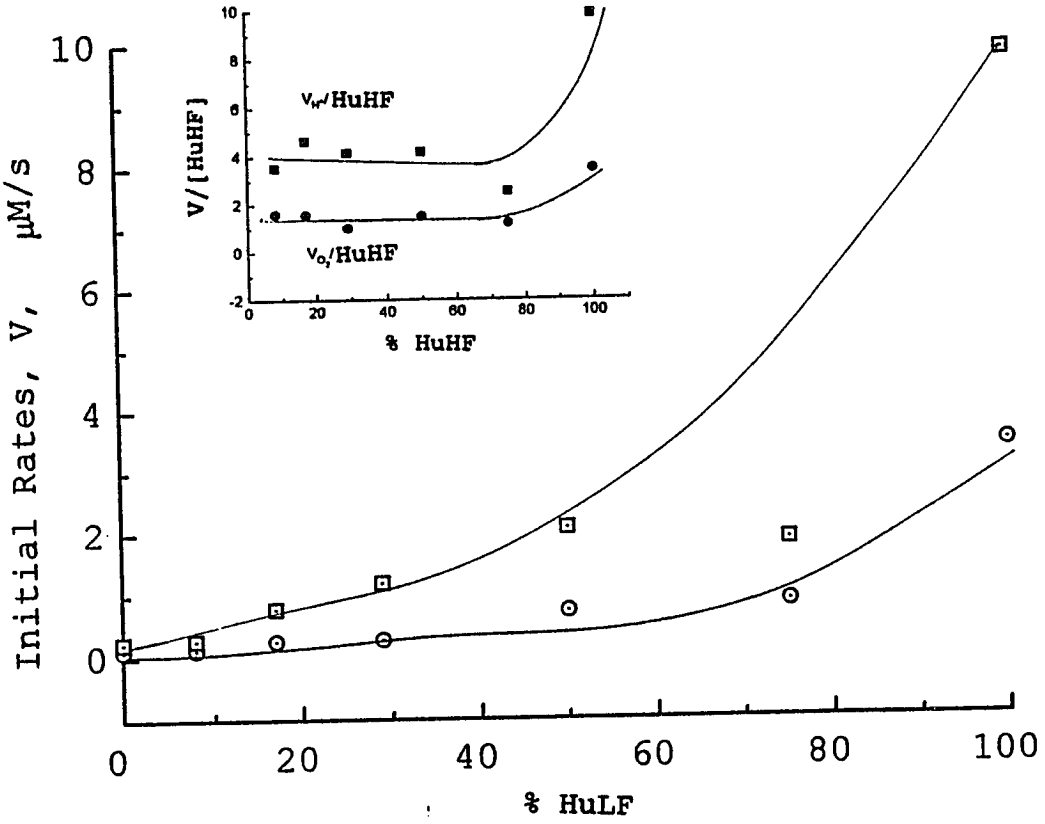

Figure 2.18: Initial rates of oxidation (⊙) and hydrolysis (⊡) as a function of HuHF composition in a heteropolymer of 222 and HuHF. Conditions: $[Protein]_{total}$ = 1.24 μM, [Fe(II)] = 73 μM, $[NaOH]_{stock}$ = 4.91 mM in 0.15 N NaCl and 0.5 mM MOPS pH = 7, 20 °C. (File name: 061594.org) **Inset:** Normalized initial rates of oxidation (●) and hydrolysis (■) against HuHF concentration as a function of HuHF composition. Conditions are the same as Figure 2.18 (File name: 061594.org)

detailed information on the mechanism of iron oxidative deposition in HuHF and HoSF. The similarities in kinetic results in HoSF and HuHF further confirm that the H-subunit acts as a ferroxidase in iron incorporation in ferritins containing H-subunit. HuLF, however, was shown to undergo different iron deposition kinetics, as expected based on its distinct role in promoting mineral core nucleation (Levi et al., 1992; Bauminger et al., 1991).

The formation of superoxide as a product of dioxygen reduction during iron deposition in ferritin has been one of the focuses of this kinetics study. Even though a superoxide production mechanism had been proposed or speculated upon previously by many researchers (Grady et al., 1989; Sun & Chasteen, 1992; Treffry et al., 1992), no evidence for its formation has been obtained. Attempts to use $^{17}O_2$ as an oxidant for iron oxidation and therefore to observe the distinctive $^{17}O_2^{\cdot-}$ superoxide radical hyperfine splitting by epr spectroscopy have given negative results (Sun and Chasteen, 1994). Efforts to add superoxide dismutase (SOD) prior to superoxide formation and thus observe a change in the initial oxidation rate, hydrolysis rate or rate ratios have proven ineffective (this work). One explanation is that the superoxide may be associated with iron at the iron binding site. Antiferromagnetic coupling of the electron spin of the radical ($S = 1/2$) with that of the Fe^{3+} ($S = 5/2$) to form an EPR silent $S = 2$ species may account for the lack of an $^{17}O_2^{\cdot-}$

epr spectrum. Also ferritin, being a hollow shell protein with narrow channels, can exclude large molecules from its ferroxidase site, accounting for the minimal effect of SOD on the reaction kinetics.

By combining oxygen electrode and pH stat measurements, the early stages of iron oxidation and hydrolysis pathways can be monitored simultaneously, and thus provide insight into the relationship between H^+ production and O_2 consumption throughout the reaction. The V_{H+}/V_{O2} ratio approaching 1 as the Fe(II)/protein ratio approaches 0 supports the existence of $O_2^{\cdot-}$ as an intermediate product of dioxygen reduction and lends support to the mechanism described in reactions 2.1, 2.6, 2.10 & 2.11. A similar one electron iron oxidation mechanism with superoxide as the product has also been demonstrated in aqueous Fe(II)-EDTA or Fe(II)-phenanthroline systems (Goto et al., 1970; Kurimura & Kuriyama, 1969; Afanas'ev, 1989).

The constant value of 0.6 H^+/Fe(II) observed at Fe(II)/HoSF of 3 - 8 may be caused by the ferrous iron binding at the protein 3-fold channels. This finding is in accord with a similar observation of ~0.4 H^+/Fe(II) produced at 8 Fe(II)/HoSF (Jacobs et al., 1989b). The Asp-131 (human H numbering) and Glu-134 residues in the 3-fold channels, Asp-42, Glu-61, Glu-64 and Glu-67 on the cavity surfaces are possible candidates for iron binding ligands, since they have been reported to play important roles in iron incorporation

into the H-chain ferritin (Treffry et al., 1993; Levi et al., 1994). These residues are also conserved in HoSF L and human L subunits (Andrews et al., 1991), which may account for partial ferrous binding to HoSF and HuLF. Other carboxyl amino acid residues, Glu-57 and Glu-60, present in HuLF (His-57 in H-chain) may be contributing to the ferrous iron binding in HuLF as well, which would explain the higher proton release in HuLF than in HoSF. Other iron binding sites are also possible, such as at His-118 suggested by ENDOR and ESSEM (Hanna et al., 1991a; Gerfen et al., 1991), which is consistent with the higher proton release in HuLF compared to HoSF since histidine may be incompletely deprotonated at pH 7. Attempts to directly observe the ferrous binding to HoSF at anaerobic condition were unsuccessful as values of 0.44 - 0.52 H^+ produced per Fe(II) added were obtained at Fe(II)/HoSF ratios of 3 to 104. It is possible that a partial ferrous core formation ($FeOH^+$) may contribute to the number of proton released at high iron loading into ferritin (Jacobs et al., 1989a).

The stoichiometric value of 0.6 H^+/Fe(II) at low iron deposition in HoSF can also be explained as one proton produced per two iron involved, which gives a H^+/Fe(II) of 0.5. This is consistent with the recent observation of a μ-oxo-bridged iron dimer forming between the ferroxidase site and the intermediate site in bacteria ferritin (conventional type), a protein that resembles HuHF in both structure and

ferroxidase activity (Hempstead et al., 1994). Thus, a different mechanism (Mechanism III), a modified version of the mechanism II from previous work (Sun & Chasteen, 1992; Sun et al., 1993) is proposed.

Mechanism III:

1st Fe(II) and O_2 binding:

$$Fe^{2+} + O_2 + P^z \rightarrow [Fe^{2+}(O_2)P^z]^{z+2} \quad (2.12)$$

1st Fe(II) oxidation, Fe(III) hydrolysis and $O_2^{\cdot-}$ formation:

$$[Fe^{2+}(O_2)P^z]^{z+2} + H_2O \rightarrow [O_2^{\cdot-}(FeOH)^{2+}P^z]^{z+1} + H^+ \quad (2.13)$$

Protein radical formation:

$$[O_2^{\cdot-}(FeOH)^{2+}P^z]^{z+1} \rightarrow [O_2^{2-}(FeOH)^{2+}P^{\cdot z+1}]^{z+1} \quad (2.14)$$

2nd Fe(II) binding and oxidation:

$$[O_2^{2-}(FeOH)^{2+}P^{\cdot z+1}]^{z+1} + Fe^{2+} \rightarrow [Fe^{3+}(O_2^{2-})FeOH^{2+}P^z]^{z+3} \quad (2.15)$$

Fe(III) hydrolytic polymerization to form core:

$$[Fe^{3+}(O_2^{2-})FeOH^{2+}P^z]^{z+3} + 3H_2O \rightarrow 2FeOOH_{core} + H_2O_2 + 3H^+ + P^z \quad (2.16)$$

In this mechanism, the superoxide is produced during dioxygen reduction but not released from the iron binding site while the ferric iron is partially hydrolyzed (reaction 2.13) giving a $V_{H+}/V_{O2} = 1$ as observed (Figure 2.2a & 2.2b). The superoxide oxidizes an amino acid residue at the protein active site to produce a peroxide and a protein based radical (reaction 2.14), possibly leading to the observation of the tyrosine radical in HuHF reported in Chapter III. The 2nd Fe(II) then binds and is oxidized to form a peroxo bridged

ferric dimer, meanwhile transferring one electron equivalent back to the protein radical to regenerate the intact protein active site (reaction 2.15). In this step, the proton release from the equation 2.13 is not consumed by superoxide dismutation as suggested by Mechanism I, but is shared by the ferric dimer and gives the stoichiometric relationship of $H^+/Fe(II) = 0.5$. The oxygen involved in the first iron oxidation is also responsible for the second iron oxidation, which addresses the net ratio of $Fe(II)/O_2 = 2$ at very low iron loading into ferritin (Fe(II)/protein → 0) (Figure 2.3). Further hydrolysis of the ferric dimer at higher iron loading of protein (Fe(II)/protein > 10) leads to the formation of hydrogen peroxide and the ferrihydrite core (reaction 2.16), where the iron mineral surface reaction (reaction 2.9) is taking place.

Both modified Mechanism I and Mechanism III are consistent with the observed kinetic and stoichiometric relationships of Fe(II), O_2 and H^+, and the one electron reduction of the dioxygen, but Mechanism III has explained the observation of dimeric iron binding in ferritin as well as the lack of detection of superoxide. Thus, Mechanism III may be a more suitable description for iron oxidative deposition in ferritin.

The iron mineral surface oxidation has been observed to occur at an iron core size of 20 - 40 Fe(II)/protein in HuLF (Figure 2.8), < ~70 Fe(II)/protein in HoSF (Figure 2.2a), and

< 400 Fe(II)/protein in HuHF (Figure 2.2b). Apparently, the more efficient (4 Fe(II)/O_2, instead of 2) and less harmful (no H_2O_2 and $OH^{\cdot}$ radicals are produced) mineral surface reaction takes place at an earlier stage where the L-subunit content in ferritin is higher, consistent with the observation that iron cluster size in ferritin varies according to the sequence HuHF < HLF or HoSF < HuLF (Wade et al., 1991; Bauminger et al., 1991; Bauminger et al., 1993). Meanwhile, the iron incorporation rates are ranked as HuHF > HoSF > HuLF with ferroxidation being the more rapid iron oxidation pathway. The combination of these two effects may be the reason that HoSF with mixed L and H subunits is more biologically favored than either H or L homopolymers, an observation in keeping with the nonexistence of homopolymers in mammals.

When terbium is present in HoSF, the mineral surface reaction takes place with a smaller core surface (10 Fe(II)/protein instead of 70) (Figure 2.12). Terbium likely binds at the ferroxidase and nucleation sites of the H-subunit and consequently saturates these active sites at low iron fluxes (Mertz & Theil, 1983). Fe(II) may therefore be oxidized on other sites of the L-subunit, following the iron deposition mechanism in HuLF. The mineral surface reaction becomes the primary pathway even at low iron loading in HoSF, in accord with the observation that terbium accelerates Fe(III) cluster formation (Treffry et al., 1993). When the iron loading increases to 70 Fe(II)/protein, iron may replace

terbium at the ferroxidase site, resulting in the mixed ferroxidation and mineral surface reactions being observed (Figure 2.13).

Two types of pathways for iron oxidative deposition in HuLF have been observed. In addition to the mineral surface reaction shown in Figure 2.11, another passage for iron deposition in HuLF is evidenced by the observation of iron oxidation at low Fe(II)/HuLF loading capacity in the absence of hydrolysis (Figure 2.8A & 2.8B). It is likely that a small portion of the initial iron, possibly 2 Fe(II)/subunit according to the stoichiometry of Fe(II)/HuLF = 40 - 50, is bound and oxidized to Fe(III) on HuLF. The newly formed Fe(III) species then serve to nucleate the formation of the mineral core where subsequent incoming iron is oxidized according to equation 2.9. The role of the L-chain in iron incorporation is conceivably as a ferric chelation sink in which iron is stored after being oxidized, either through ferroxidation by the H-subunit or through aqueous iron autoxidation. This idea is in accord with the observation that ferritin serves as a ferric iron source for iron uptake in transferrin (Bakker & Boyer, 1986). It also explains the loss of iron incorporation ability of HuLF at pH 5.5 and its restoration in the presence of HuHF (Levi et al., 1992; Levi et al., 1989), since only iron ferroxidation, not autoxidation, is efficient at acidic pH (Figures 2.14 and 2.15).

The difference in the apparent $K_{m,Fe}$ and k_{cat} values obtained using proton release rates compared to that using the oxygen consumption rates is probably caused by the continually changing of iron oxidation pathways as iron is added to the protein, from iron ferroxidation (equation 2.5) to iron mineral surface oxidation (equation 2.9). Consequently, the number of protons produced per oxygen consumed are constantly changing as the hydrolysis reaction changes, resulting in the changes in V_{H+} and V_{O2} as observed in Figures 2.2a and 2.2b. In general, the apparent values for K_m and k_{cat} obtained using oxygen consumption rates should be more accurate, since iron oxidation by dioxygen is apparently controlling the iron hydrolysis (Figure 2.1). In addition, the much larger calculation errors introduced in the double reciprocal plots when using the hydrolysis rates (~57% error) than using the oxidation rates (~12% error) may also contribute to the disagreement between K_m and k_{cat} for oxidation *vs.* hydrolysis.

The previous report that P_i accelerates the Fe(II) to Fe(III) oxidation rate in HoSF as monitored by Mössbauer spectrometry (Cheng & Chasteen, 1991), has not been substantiated by electrode oximetry measurement (Figure 2.17) (Sun & Chasteen, 1992). It is possible that a certain amount of iron may not be oxidized by dioxygen reduction but by the protein itself and would escape detection in the present experiment but be seen by Mössbauer spectrometer (Watt et al., 1992). The faster iron oxidation rate in the absence of

protein reported previously compared to this work (Figure 2.1A), however, is likely due to autoxidation at pH 7.5, the experimental condition used (Cheng & Chasteen, 1991). It is also possible that phosphate accelerates the ferric core rearrangement as shown by the decreased quadrupole splitting after iron is oxidized (Cheng & Chasteen, 1991), but not the iron oxidation rate. This idea is in agreement with the observation that faster iron cluster formation is observed in mutant 222 with the ferroxidase site mutated than in HuHF, even though the iron oxidation rate is slower in 222 (Bauminger et al., 1991). Unfortunately, the ferric core structure and species distribution in ferritin cannot be monitored in the type of study reported here.

In summary, this work provides further insight into the kinetic descriptions of iron oxidative deposition in the ferritins. Superoxide has been implicated as an intermediate product of dioxygen reduction during iron ferroxidation in both recombinant H-chain ferritin and horse spleen ferritin as described in modified mechanism I and mechanism III. Iron deposition in recombinant L-chain ferritin appears to be very different from that of H-subunit containing ferritins, iron oxidation at the mineral surface being the dominant pathway in the former protein.

CHAPTER III

CHARACTERIZATION OF RADICALS FORMED DURING INITIAL IRON UPTAKE IN FERRITIN OBSERVATION OF TYROSINE RADICAL FORMATION

Introduction

Oxygen radicals have been implicated in pathogenetic processes of a large number of diseases and dysfunctions due to the damage they inflict upon critical cellular components such as DNA, proteins and lipids (Halliwell & Gutteridge, 1988; Davies et al., 1991; Starke & Farber, 1985; Reif, 1992). The production of oxygen radicals normally occurs in the presence of transition metals such as iron through the Haber-Weiss process (equations 3.1 - 3.3), where iron acts as a catalyst for the generation of an extremely reactive radical, the hydroxyl radical, from hydrogen peroxide (Graf et al., 1984; Grady & Chasteen, 1990; Bolann & Ulvik, 1993).

$$Fe^{2+} + O_2 \rightarrow Fe^{3+} + O_2^{\cdot -} \quad (3.1)$$

$$2O_2^{\cdot -} + 2H^+ \rightarrow H_2O_2 + O_2 \quad (3.2)$$

$$Fe^{2+} + H_2O_2 \rightarrow HO^{\cdot} + HO^- + Fe^{3+} \quad (3.3)$$

Since hydrogen peroxide and superoxide have been reported to form during iron uptake in ferritin (Xu & Chasteen, 1991; Sun & Chasteen, 1992), characterization of these oxygen

radicals, their abilities to mobilize iron and their damage to the ferritin molecule, are of great interest (Grady et al., 1989; O'Connell et al., 1986; Bolann & Ulvik, 1990; Bolann & Ulvik, 1993; Grady & Chasteen, 1990).

The mechanisms of iron deposition into the cavity of horse spleen ferritin (HoSF, 16% H and 84% L) has been studied extensively (Arosio et al., 1978; Crichton et al., 1980; Sun & Chasteen, 1992; Xu & Chasteen, 1991). This process involves both Fe(II) oxidation and Fe(III) hydrolytic polymerization (Lawson et al., 1989). At low fluxes of iron deposition into ferritin (< 50 Fe(II)/HoSF), the ferritin coat plays a catalytic role in iron oxidation. The stoichiometric relationships of Fe^{2+}, O_2 and H^+ are described in equation 3.4 (Xu & Chasteen, 1991; Sun & Chasteen, 1992).

$$2Fe^{2+} + O_2 + 4H_2O \rightarrow 2FeOOH_{core} + H_2O_2 + 4H^+ \qquad (3.4)$$

This catalytic site is at the ferroxidase center, consisting in part of residues Glu-27, Glu-62 and His-65, on the H-subunit (Lawson et al., 1991; Lawson et al., 1989; Treffry et al., 1992). Several other residues, Gln-141, Ala-144 and Tyr-34 are also in the vicinity of this ferroxidase center and also contribute to the facilitation of iron oxidation but to a lesser extent (Hempstead et al., 1994). Recently, residue Tyr-34 has been discovered as a ligand in a Fe(III)-tyrosinate complex which gives an absorbance at 550 nm (Waldo et al.,

1993; Waldo & Theil, 1993) (Harrison et al., unpublished results). The kinetic role of the Fe(III)-tyrosine complex in iron incorporation into ferritin, however, is not clear.

The L-subunit has been shown to have the ability to facilitate iron oxidation (Chapter II), even though no ferroxidase center has been located on the L-subunit. Iron oxidation in the recombinant L-chain ferritin is thought to occur directly on the mineral surface of the iron core with water instead of hydrogen peroxide as the final product of dioxygen reduction (Levi et al., 1992; Xu & Chasteen, 1991; Andrews et al., 1992; Cozzi et al., 1990) (Chapter II).

A protein radical formed during iron oxidative deposition in horse spleen ferritin has been reported previously (Grady et al., 1989). This radical was determined to be a hydroxyl radical derived protein radical which is formed only during the initial stages of iron deposition (Grady et al., 1989). What is still unclear, however, is the location of the radical in the protein structure and the functional role this radical plays in the iron uptake process.

In this work, recombinant horse L-chain (HoLF) and human H-chain ferritin (HuHF) as well as various H-chain mutants were utilized to locate the site of protein radical formation. Evidence will be presented to suggest that two types of protein radicals are formed in HuHF and HoSF during dioxygen reduction. One radical formed in HuHF is a Tyr-34 centered radical, possibly related to the formation of superoxide.

Another radical formed in HoSF is a Fenton chemistry (equation 3.3) related radical, probably the result of the attack of $OH^{\cdot}$ on the protein. The site(s) of formation of the HoSF radical is unknown at this point, however, it is speculated to be at one of the iron binding sites on the L-subunit. The reaction of the L-subunit with $OH^{\cdot}$ radical may be biologically favored since it may help minimize hydroxyl radical damage to the ferroxidase site on the H-subunit, thus protecting the iron oxidation capability of ferritin.

Material and Methods

Monobasic and dibasic phosphate were obtained from Fisher Scientific Inc. and MOPS, BES and HEPES buffers were from Research Organics. Iron sulfate and potassium ferricyanide were purchased from Baker Scientific Inc.. 2,2,5,5-tetramethyl-3-pyrrolin-1-yloxy-3-carboxamide was from Eastman Kodak. L-Tyrosine, H_2O_2, PBN, EDTA disodium salt dihydrate, sodium dithionite (technique grade), vanadyl sulfate and mercaptoacetic acid (thioglycolic acid, TGA) were from Aldrich and ceruloplasmin was from Calbiochem. All reagents were reagent grade or purer unless otherwise stated.

Horse spleen ferritin (HoSF) was purchased from Boehringer-Mannheim and sheep spleen ferritin was isolated from frozen sheep spleen (Mertz & Theil, 1983), (Appendix III). Recombinant horse L-chain ferritin (HoLF), E-coli ferritin (FTN), human H-chain ferritin (HuHF) and HuHF

mutants, Y34F, Y29F, Y32F, Q141E, A144H were provided by Dr. Pauline Harrison and coworkers at the University of Sheffield, UK. The HuHF mutants, 222 (E62K, H65G, K86Q) and S-13 (K86Q, W93F) were provide by Dr. Paolo Arosio and coworkers at the University of Milan, Italy. Apoferritins were prepared using the dithionite method (Appendix II) or the thioglycolic acid method (Chasteen & Theil, 1982). The subunit composition of apoferritin was determined using 12.5% and 17% SDS PAGE.

All experiments were carried out in 50 mM MOPS buffer, pH 7.0, unless otherwise stated. All epr measurements were performed on a Varian E-4 or E-9 epr spectrometer, equipped with a TE_{102} or TE_{104} cavity, respectively, and interfaced with an ISA-standard Intel 80486 based computer. Epr data acquisition software, version 2.41A (Scientific software services, Bloomington, IL) was used to acquire and manipulate epr spectra.

Unless otherwise stated, directly observed protein radicals were generated by passing a stream of moist argon gas over a 17 μM apoprotein solution in 50 mM MOPS buffer and 0.15 N NaCl, pH 7.0, with constant stirring for 45 - 60 minutes. An $FeSO_4$ solution (0.1 M, pH < 2) was added to the protein solution to reach an Fe(II)/protein ratio of 150. The ferrous iron was then incubated with protein anaerobically for 3 minutes before it was exposed to moist O_2 (1 atm) for 1 minute for HuHF and HuHF mutants, 3 minutes for HoSF and sheep spleen ferritin (6.25 μM) and 4 minutes for HoLF. The sample

solution was then transferred to a quartz epr tube which was immediately frozen in a dry ice-acetone bath. The epr measurements were performed at 77 K.

Inhibitions of radical formation in HoSF by ceruloplasmin (10 μM) and Zn^{2+} (0.833 mM) followed the same procedures and conditions as described above except the inhibitors were incubated with the HoSF solution for 30 - 40 minutes prior to the addition of Fe(II). A concentration of 0.010 mM HoSF in 50 mM phosphate buffer was used in the ceruloplasmin inhibition experiment and an Fe^{2+}/HoSF ratio of 50 was used in the zinc inhibition experiment.

Ferritin radicals generated using other oxidants followed the same procedures and conditions as described above except a 5 μl of a 3% H_2O_2 solution was added anaerobically instead of oxygen to 8.8 μM HoSF, HuHF, HoLF and bacteria ferritin (conventional type, FTN) solutions for 1 minute or a 25 mM $K_3Fe(CN)_4$ solution was added to a 17 μM HoSF solution for 3 minutes. In the case of the VO^{2+}/H_2O_2 system used to generate HoSF radicals, a 0.39 mM VO^{2+} solution was added to a 17 μM HoSF sample (VO^{2+}/HoSF = 23) prior to the addition of H_2O_2. In the case of Fe(II)/EDTA/H_2O_2 system used to generate HoSF radicals, 1.66 mM Fe(II) was incubated with 3.32 mM EDTA for 10 minutes prior to their addition to the 17 μM HoSF solution.

Reduced and oxidized HoSF were prepared by incubating HoSF with 4 mM sodium dithionite or 4 mM potassium ferricyanide, respectively, for 3 - 4 hours prior to removal

of reagents through ultrafiltration under nitrogen atmosphere (Watt et al., 1992).

The spin trapped ferritin radical was generated by incubating a HoSF solution with 50 mM α-phenyl-N-t-butyl-nitrone (PBN) in 0.15 N NaCl and 50 mM MOPS buffer, pH 7.0, anaerobically for 45 minutes prior to the addition of 150 Fe(II)/HoSF for 3 minutes. One atm oxygen was then purged through the sample solution for 4 minutes. Epr measurements were carried out immediately at room temperature in an aqueous solution flat quartz cell.

Separation of the spin trapped protein radicals was conducted in an Amicon 3 ml ultrafiltration cell with a XM 300 membrane (M.W. cutoff 300,000) and a UM 5 membrane (M.W. cutoff 500) over a period of 40 minutes.

Concentrations of the directly observed radicals were calculated by comparing the double integral of the radical first derivative signal against a radical standard 2,2,5,5-tetramethyl-3-pyrrolin-1-yloxy-3-carboxamide. Radical half-lives were calculated from slopes of the logarithm radical decay plot.

The radical power saturation experiment was conducted in the front cavity (cavity I) of the critically coupled E-9 spectrometer. The microwave power distributed in cavity I was calculated as 0.875 x dial settings, according to Appendix E. The power at half saturation, $P_{1/2}$, and the inhomogeneity parameter, b, were obtained from a curve fit based on equation

3.5 using the software package, Origin 3.5 (MicroCal Scientific, Inc.) (Styring & Rutherford, 1988; Sahlin et al., 1986; de Paula & Brudvig, 1985).

$$A = KCP^{0.5}/[1 + (P/P_{1/2})]^{0.5b} \qquad (3.5)$$

Here A is radical signal amplitude, K is an apparatus related parameter, C is the radical concentration and P is the microwave power used in the epr measurement.

The amino acid residue analysis for HoSF samples containing 50 mM phosphate and 150 Fe(II)/protein oxidized by 6 different concentrations of H_2O_2 were conducted at the University of Texas, Medical Branch, Galveston, Texas. The protein in each sample was hydrolyzed with 6 N HCl at 108 °C then derivatized with ninhydrin, followed by the separation of amino acids at 51 °C using a Beckman Model 121MB (microbore reaction coil) single column packed with Beckman W-2 resin.

The model tyrosine radical was generated using a Rayonet photochemical reactor (The Southern N.E. UV Co., Middletown, Conn.) equipped with a UV lamp with output at 253.7 Å. A rotating epr tube containing 250 μl deoxygenated frozen solution of 10 mM tyrosine in 12.5 mM sodium borate buffer, pH 10.0, was placed in a quartz insert dewar filled with liquid nitrogen. The tyrosine solution was illuminated for 2 minutes and the radical formation was monitored by epr spectrometer (Sahlin et al., 1987).

Results

Directly Observed Radical during Fe(II) Oxidation by O_2

HoSF Radicals - Phosphate is a physiological buffer and a component of the iron core in ferritin (Treffry & Harrison, 1978). It also complexes both Fe(II) and Fe(III), thus influencing the iron oxidation rate and the reaction mechanism of iron oxidative deposition in ferritin (Graf et al., 1984; Burkitt & Gilbert, 1991). Good's buffers are commonly used in studying iron incorporation into ferritin due to their intrinsic low affinity for iron and their small effect on iron oxidation (Tadolini, 1987). Unfortunately, Good's buffers have been reported to generate buffer radicals (Grady et al., 1988). In the experiments reported here, radicals produced during iron oxidation by dioxygen in HoSF were examined in the presence of phosphate (A) and three Good's buffers, MOPS (B), HEPES (C) and BES (D) (Figure 3.1). A 3-line radical epr spectrum with a g-factor of 2.0067 $\pm$ 0.0005, a peak to trough linewidth, ΔH_{Bpp} = 17 $\pm$ 0.9 G and a hyperfine splitting (between stick markers), a = 12 - 13 G were obtained in the presence of phosphate (Figure 3.1, spectrum A). A five-line radical signal with a g value of 2.0066 $\pm$ 0.0005, a = 11 - 14 G and ΔH_{Bpp} = 30 $\pm$ 1.8 G was observed for all three Good's buffers (Figure 3.1, spectra B, C & D). All radical signals were observed with protein solutions retained on an XM 300 membrane at room temperature with or without the presence of a spin trapping reagent, indicating that the observed radicals

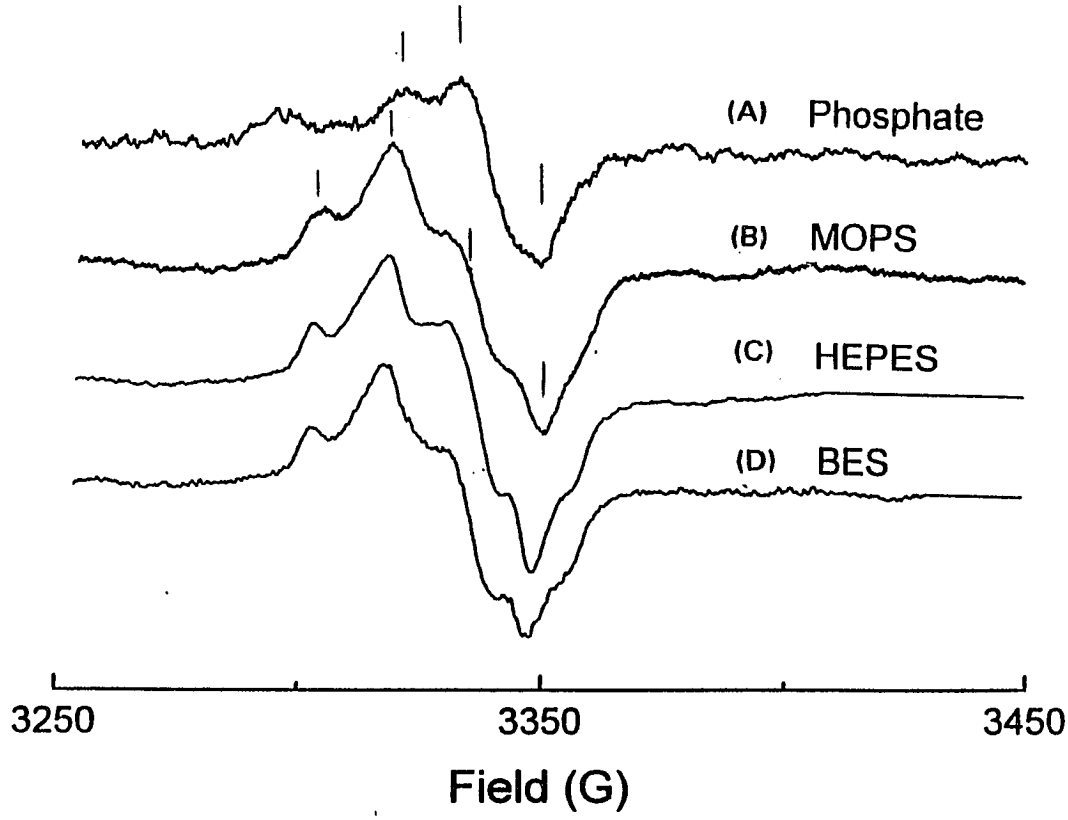

Figure 3.1: Epr spectra of HoSF radicals formed in the presence of phosphate (A), MOPS (B), HEPES (C) or BES (D) buffers, cavity signals are not subtracted. Conditions: 2.6 mM FeSO4 solution was added to 300 μl of 17 μM HoSF in 50 mM buffer and 0.15 N NaCl, pH 7.4, under moist Ar, followed by the exposure of the sample to 1 atm O_2 for 4 minutes. The sample was then frozen in dry ice - acetone bath. Spectral parameters: Field set, 3350 G; Scan range, 200 G; Time constant, 3 s; Power, 20 mW; Modulation amplitude, 5 G; Scan time, 16 minutes; Frequency: 9.3711 GHz; Temperature: 77 K. Hyperfine splittings were measured between the stick markers. (File names: Sep2402.fls, Dec0436.fls, Dec1005.fls, 07301493.fls, 08170794.fls)

are ferritin associated radicals which do not traverse the membrane.

Occasionally, the spectrum observed with phosphate was also seen with MOPS and vice versa, indicating that the observed spectra are not entirely buffer specific. Both types of spectra are similar to those reported for tyrosine based radicals found in other proteins (Lassmann et al., 1991; Hallahan et al., 1992; Bender et al., 1989; King et al., 1967) and thus appear to be related. The strong iron chelator, EDTA, inhibits the radical formation by ~75%, when complexed to Fe(II) prior to oxidation in ferritin, suggesting that iron binding to protein is a requirement for radical formation.

Figure 3.2 shows epr spectra of HoSF radical formation and decay. An axial radical signal with component A_1 and A_2 was detected at 4.4 K when Fe(II) was added to ferritin and subsequently exposed to oxygen for 1 minute. The g factors for A_1 and A_2 are 2.0379 and 2.0056, respectively (Figure 3.2a). This axial signal decays over time with the A_1 signal decaying away completely 2 minutes after the initiation of iron oxidation. Signal A_2 remained observable but reached its minimum signal amplitude before increasing again, indicating the disappearance of one radical species, which is responsible for the observation of A_1 & A_2, and the formation of another radical species at approximately the same field position as A_2. At 4 minutes, this new radical at the A_2 position started to grow and the signal evolved into a 5-line structured

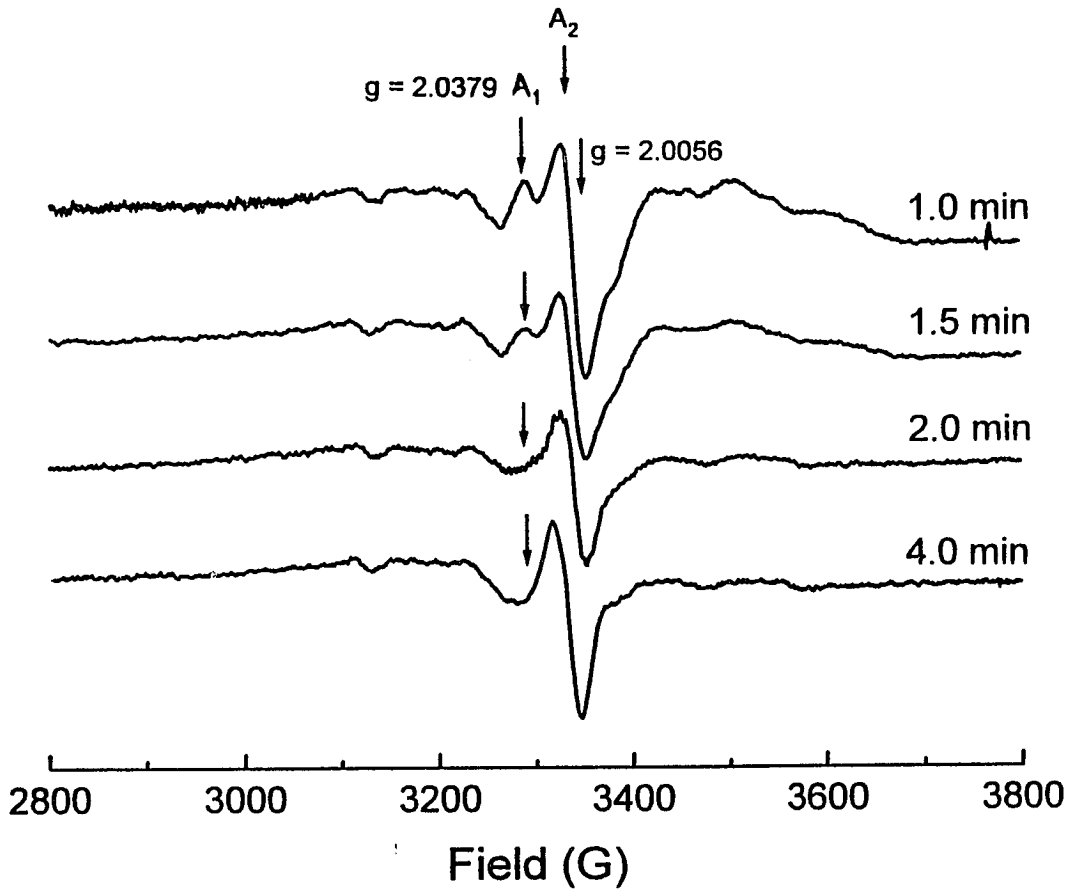

Figure 3.2a: The HoSF radical decay from 1 to 4 minutes. Conditions: [HoSF] = 17 μM, [FeSO4] = 2.6 mM in 50 mM MOPS and 0.15N NaCl, O_2 = 1 atm, pH 7.1. Sample preparation is the same as described in Figure 3.1 except the O_2 purging time was 1 minute. The same sample was repeatedly thawed and frozen at various times to record the radical decay. Spectral parameters: Field set, 3330 G; Scan range, 1000 G; Time constant, 1 s; Power, 0.5 mW; Modulation amplitude, 10 G; Scan time, 8 minutes; Frequency: 9.3863 GHz; Temperature: 4.4 K. The g factors are 2.0379 for A_1 and 2.0056 for A_2. (File name: AXIAL.org)

radical signal at 5 minutes as observed in Figure 3.2b. This fine structured radical signal reached its maximum between 20 to 30 minutes (Figure 3.3a, curve A), corresponding to a radical concentration of ~10% of the 24mer protein concentration as judged from the value of the epr double integral. The yield of radicals is low, approximately one radical produced per 600 - 1000 Fe(II) oxidized. This fine structured radical signal decay has 2 first-order phases as shown in Figure 3.3b, curve A. The signal was reduced to 55% of the maximum at the end of the first phase (150 minutes) which has a half life of 100 minutes, and 15% after 40 hours which gives a half life of 10 hours for the second decay phase.

Decay for the 3-line radical formed in the presence of phosphate buffer is shown in Figure 3.3a, curve B. A maximum radical signal was observed 4 minutes after the Fe(II) was exposed to O_2. This radical signal decayed in 3 first-order decay phases (Figure 3.3b, curve B) with the signal amplitudes being reduced to 60% at 50 minutes (first phase), 48% at 180 minutes (second phase) and 38% after 40 hours (contamination signal in the cavity of the epr spectrometer is not subtracted). The half lives of this radical are 20 minutes, 100 minutes and 12 hours for 1st, 2nd and 3rd decay phases, respectively.

Radicals formed in both MOPS and phosphate buffers were found to be pH dependent with optimal radical signal

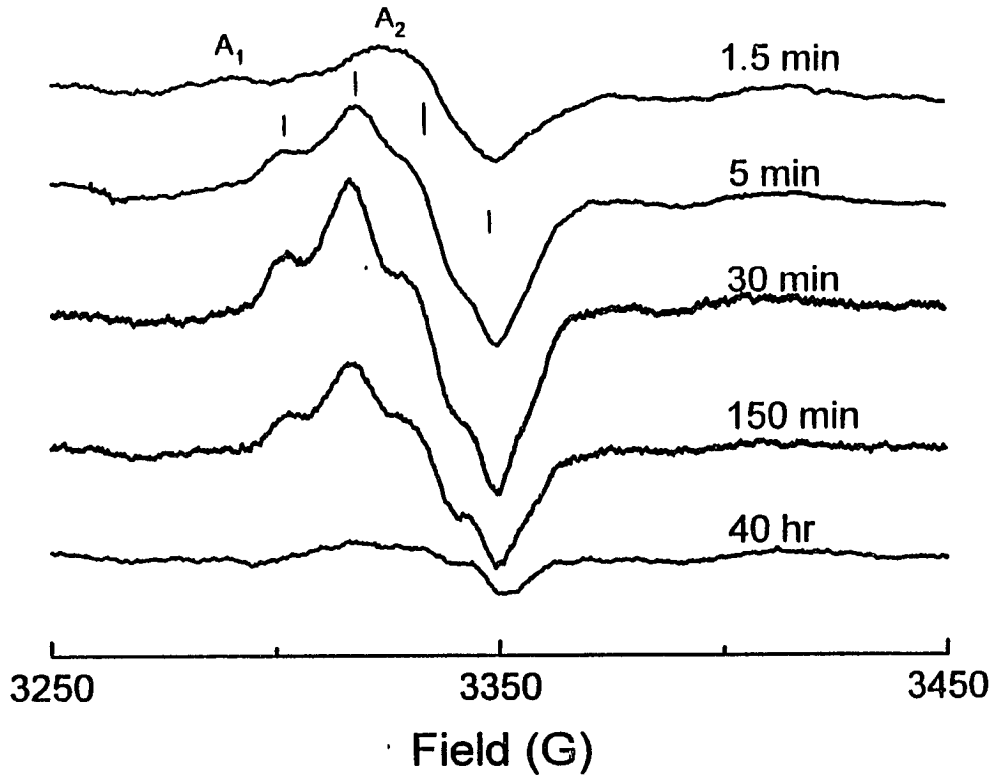

Figure 3.2b: The HoSF radical decay from 3 minutes to 40 hr. Conditions: [HoSF] = 17 μM, [FeSO4] = 2.6 mM in 50 mM MOPS and 0.15N NaCl, O_2 = 1 atm, pH 7.1. Sample preparation is the same as described in Figure 3.2a. Spectral parameters are the same as given in Figure 3.1. Hyperfine splittings were measured between the stick markers. (File name: HOSFDCY.org)

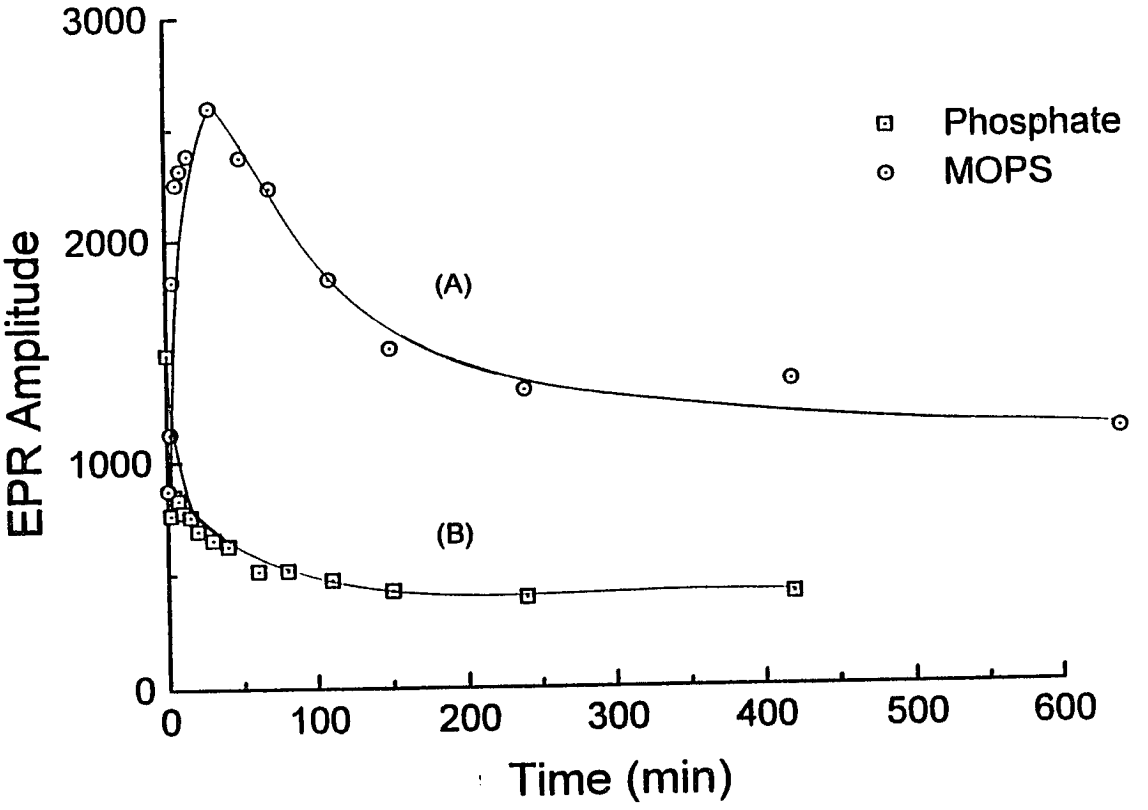

Figure 3.3a: Time course for the decay of the HoSF radical observed in MOPS (A) and phosphate (B) buffer. Sample preparation and conditions are the same as described in Figure 3.2b. (File name: BUFDECY.org)

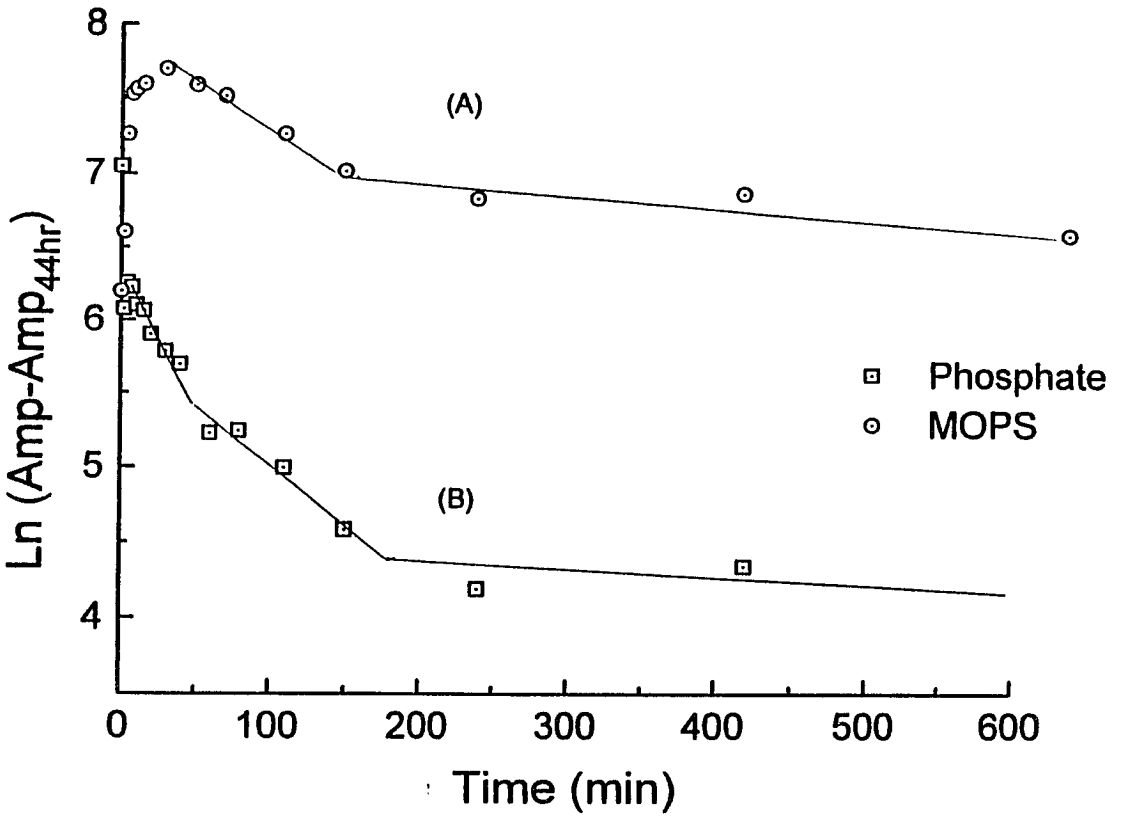

Figure 3.3b: First order plot of HoSF radical decay, ln(Amp - Amp_{44hr}) *versus* time, where Amp_{44hr} is the epr amplitude at 44 hr. HoSF radicals were generated in the presence of both MOPS (A) and phosphate (B) buffer. Conditions are same as given in Figure 3.2b.
(File name: BUFDECY.org)

amplitudes observed at pH 6.5 - 8. The line shapes and g factors, however, were found to be invariant with the pH.

HuHF Radicals - Figure 3.4 shows the HuHF radical epr signal generated during iron oxidation by dioxygen in MOPS buffer (Figure 3.4). Similar to the HoSF radical, the initial HuHF radical (at 1 min), is also relatively featureless. It then evolves to a partially resolved 3-line spectrum at 1.5 minutes, with a g factor of 2.0072 $\pm$ 0.008, hyperfine splitting of 18 - 19 G between the doublet marked by sticks and ΔH_{Bpp} = 30 $\pm$ 1.2 G. The HuHF radical signal reaches its maximum intensity 2 minutes after the Fe(II) loaded HuHF is exposed to oxygen, corresponding to 1 radical produced per 4 protein molecules and 300 - 600 Fe(II) ions oxidized. The fine structures of the radical signal then decay over time, resulting in the whole radical signal becoming featureless at 6 minutes, and diminishing to near background levels at 70 minutes. The remaining radical signal is ~18% of the maximal intensity (including background cavity signal) (Figure 3.4 & 3.5). Three first-order decay phases were observed for the HuHF radical, with the first, second and third phases ending at 3, 20 and 120 minutes, a signal amplitude reduction of 21%, 60% and 85%, respectively (Figure 3.5, inset). The half lives for 1st, 2nd and 3rd decay phases are 2.2, 4 and 50 minutes, respectively.

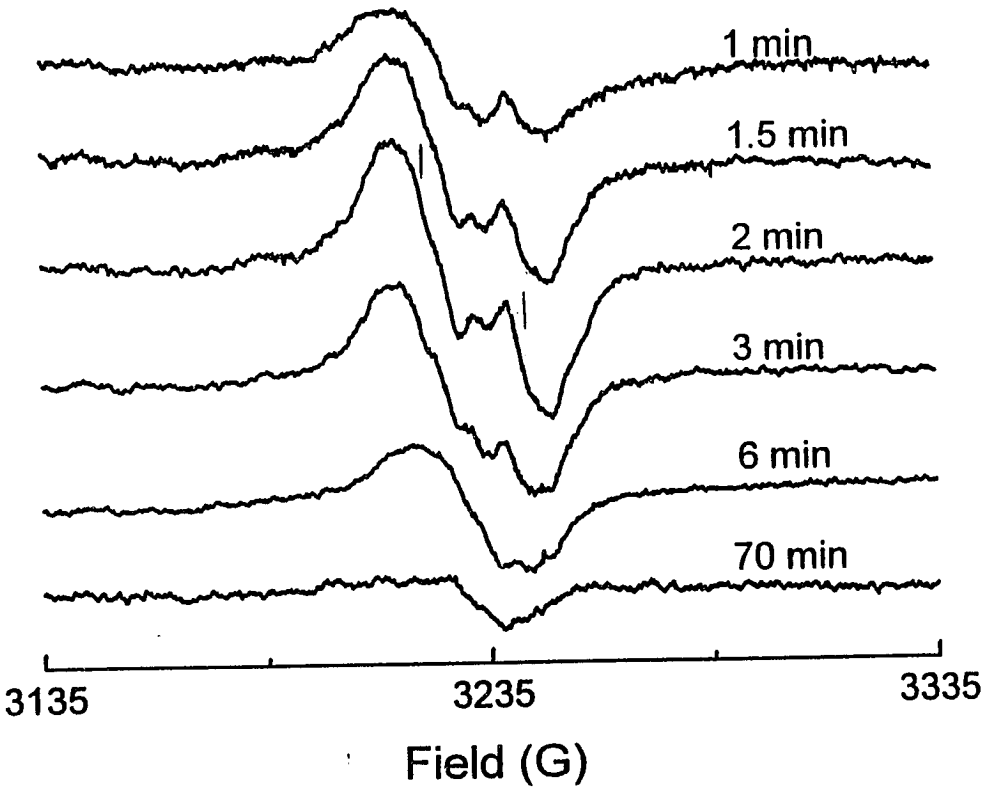

Figure 3.4: HuHF radical decay over time. [HuHF] = 17 μM, [Fe(II)] = 2.6 mM in 50 mM MOPS and 0.15 N NaCl, O_2 = 1 atm, pH 7.1. Sample preparation is the same as given in Figure 3.2a. Spectral parameters: Field set, 3235 G; Scan range, 200 G; Time constant, 3 s; Power, 20 mW; Modulation amplitude, 5 G; Scan time, 16 minutes; Frequency: 9.06352 GHz; Temperature: 77K. Hyperfine splitting was measured between the stick markers. (File name: RHFDECAY.org)

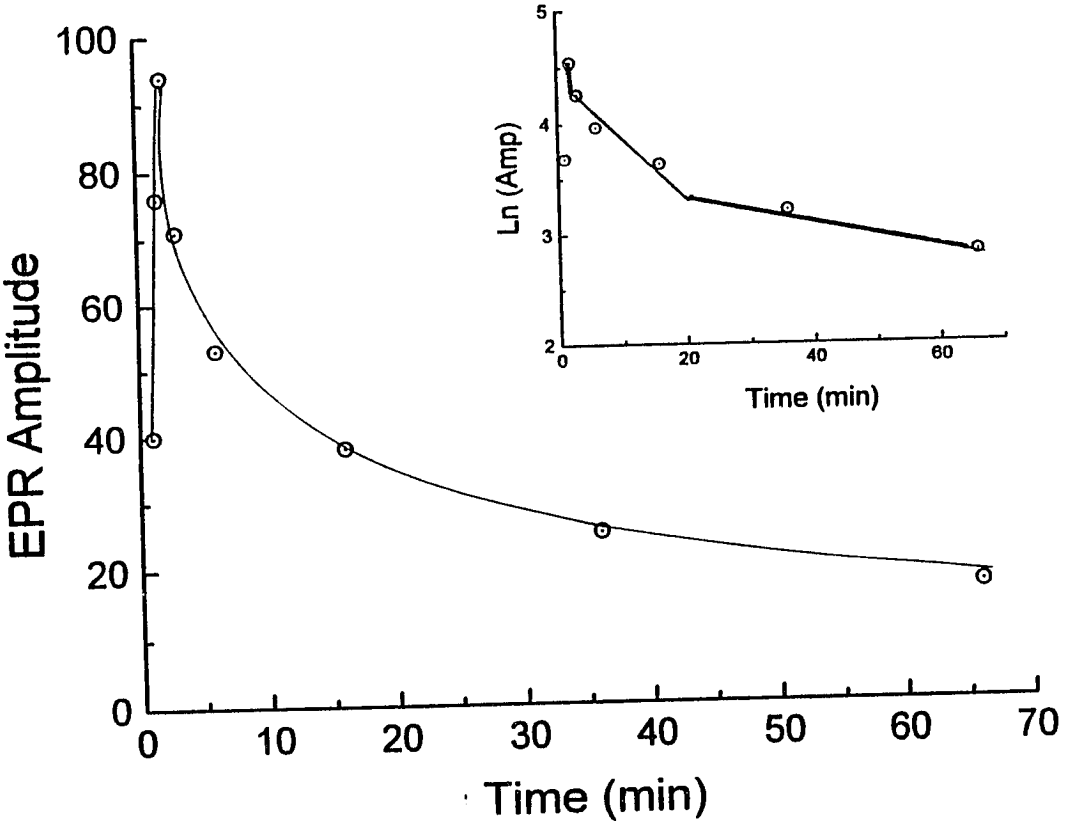

Figure 3.5: Time course for the decay of the HuHF radical. The sample was prepared the same as described in Figure 3.2a. Inset: First order plot of HoSF radical decay, Ln (Amp) *versus* time. Conditions are the same as described in Figure 3.4. (File name: Power.org)

Power Saturation - The microwave power saturation behaviors of the HoSF and HuHF radicals are shown in Figure 3.6 and 3.7, respectively. All features in both HoSF and HuHF radical epr spectra (Figure 3.1, spectrum B, and Figure 3.4) show uniform power saturation behaviors, suggesting they may come from the same radical species. A power at half saturation, $P_{1/2}$ = 6.79 ± 1.23 mW and 12.16 ± 1.45 mW were obtained from the HoSF and HuHF radical data, respectively, which are 10 - 20 fold greater than the $P_{1/2}$ of 0.65 ± 0.19 mW obtained from the model compound tyrosine radical (g = 2.0052) generated by UV radiation (Figure 3.8 & 3.9), suggesting the ferritin radical sites of formation may be in close proximity to the iron center. An inhomogeneity constant, b = 1.23 ± 0.08, was also obtained from the HoSF radical data, as expected for a frozen solution sample. A smaller b value of 0.61 ± 0.02 obtained from the HuHF radical data in Figure 3.7 is probably caused by the lack of complete saturation of the radical spectra within the microwave power range studied.

The HoSF radical generated in the presence of phosphate buffer showed a similar $P_{1/2}$ (8.95 ± 1.88 mW) and b value (1.37 ± 0.15) to that in MOPS buffer, consistent with the idea that the observed HoSF radicals are not buffer dependent.

Ferritin Radical Formation Site - Identification of the subunit type responsible for the formation of ferritin radicals was accomplished using recombinant horse L-chain

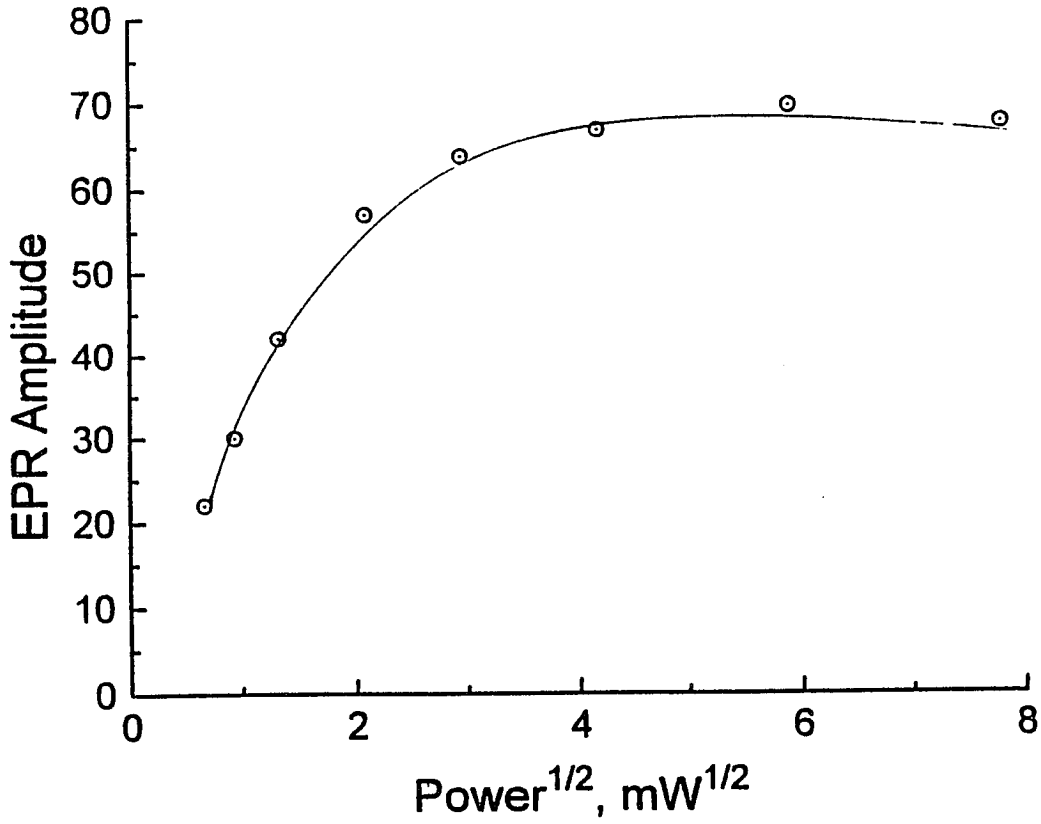

Figure 3.6: Power saturation of the HoSF radical in MOPS buffer. Sample preparation and conditions are the same as described in Figure 3.1. A half saturation $P_{1/2}$ and an inhomogeneity parameter were obtained from the curve fit to the equation described in the "Material and methods" section.

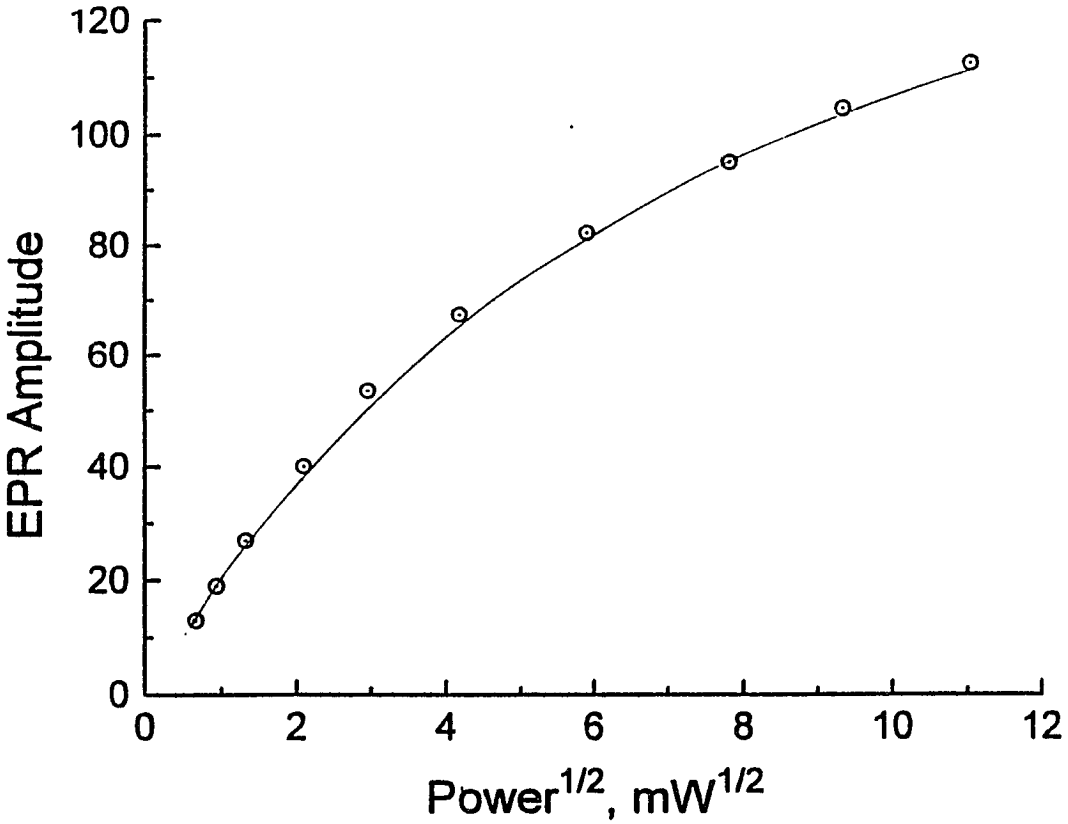

Figure 3.7: Power saturation of the HuHF radical in MOPS buffer. Sample preparation is the same as described in Figure 3.2a. Conditions are the same as described in Figure 3.4. A half saturation $P_{1/2}$ and an inhomogeneity parameter were obtained as described in Figure 3.6. (File name: Power.org)

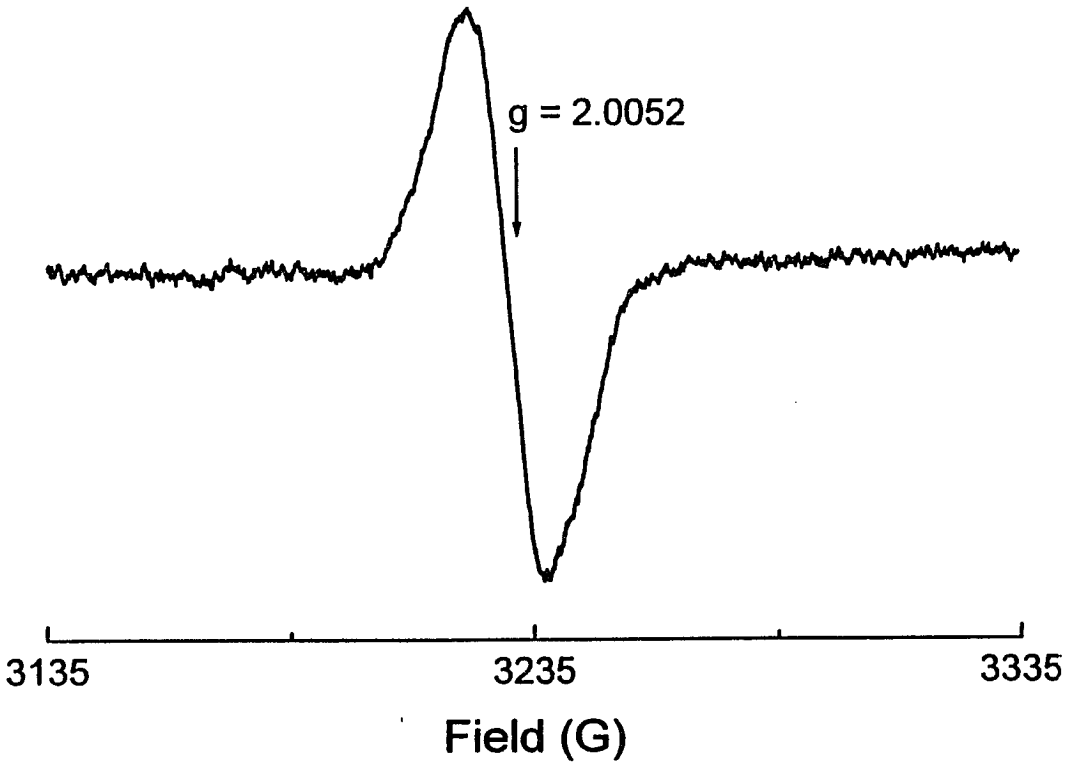

Figure 3.8: A model tyrosine radical generated by UV radiation. Conditions: [L-tyrosine] = 10 mM in 12.5 mM borate buffer, pH 10.0. The frozen tyrosine solution was radiated at 253.7 Å for 2 minutes. Spectral parameters are the same as described in Figure 3.4 except the microwave power is 5 mW and modulation amplitude is 2 G. (File name: PURETYR.org)

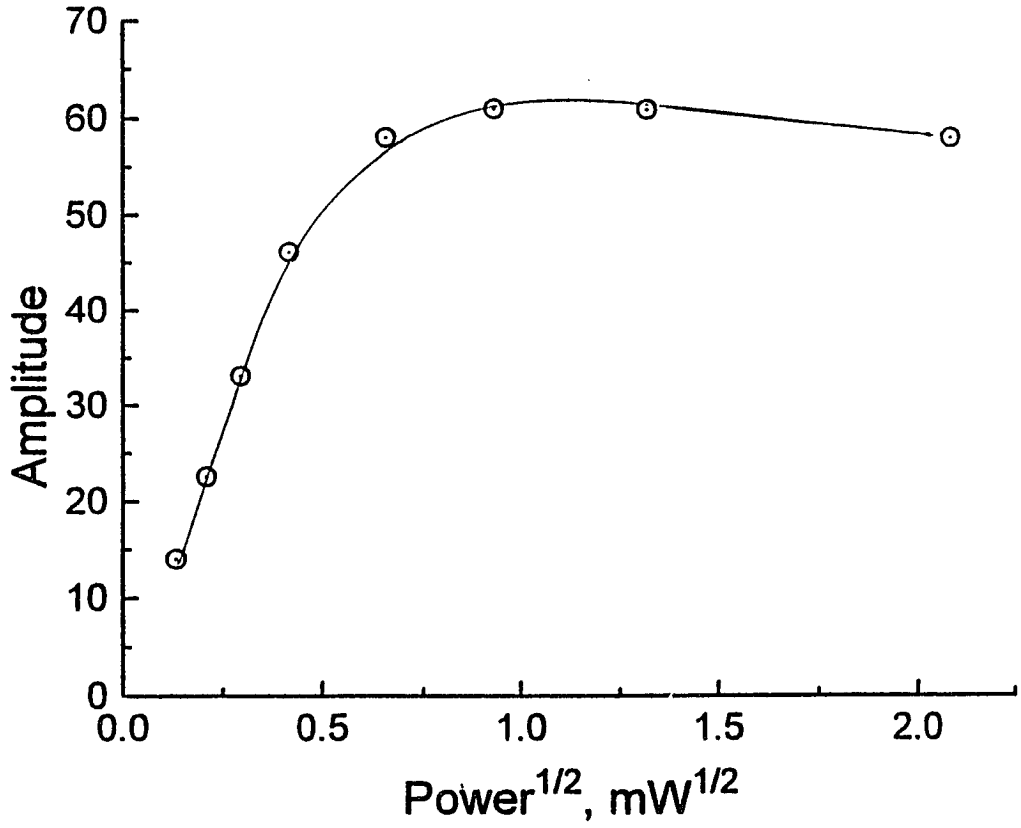

Figure 3.9: Power saturation of the model tyrosine radical. Conditions are the same as described in Figure 3.8. A half saturation $P_{1/2}$ and an inhomogeneous parameter were obtained as described in Figure 3.6. (File name: TYRPOW.org)

(HoLF) and human H-chain ferritin (HuHF) homopolymers as well as the heteropolymers, sheep spleen ferritin (55% H, 45% L and ~40% dimer) and horse spleen ferritin (16% H, 84% L) (Figure 3.10). No apparent ferritin radical was detected with L-chain ferritin, indicating the radical formation requires the presence of the H-subunit in ferritin. Sheep spleen ferritin generates a similar protein radical epr signal to that of HoSF (Figure 3.1, spectrum B) but with a 51 - 58 % reduction in signal amplitude, suggesting the L-subunit may also contribute to the radical formation, in accord with the cooperative roles observed between L and H subunits in iron incorporation into ferritin (Levi et al., 1992; Levi et al., 1989).

Since the ferroxidase site was reported to be the most important site on the H-subunit for catalyzing iron oxidation (Lawson et al., 1991; Sun et al., 1993; Treffry et al., 1992), several ferroxidase site mutants were employed to investigate the possible involvement of the ferroxidase site in HuHF radical formation (Figure 3.10). The mutant 222, an HuHF variant with the Glu-62 and His-65 residues mutated, lacked the HuHF radical signal, suggesting the HuHF radical formation is either located on residue Glu-62 or His-65 or it is originated from iron ferroxidation at the site (equation 3.4). Mutant Q141E, a HuHF mutant that disrupts the bonding between Gln-141 and the Fe^{2+} at the ferroxidase site, was shown to generate a radical with entirely different features than that of the HuHF, supporting the idea that HuHF radical formation

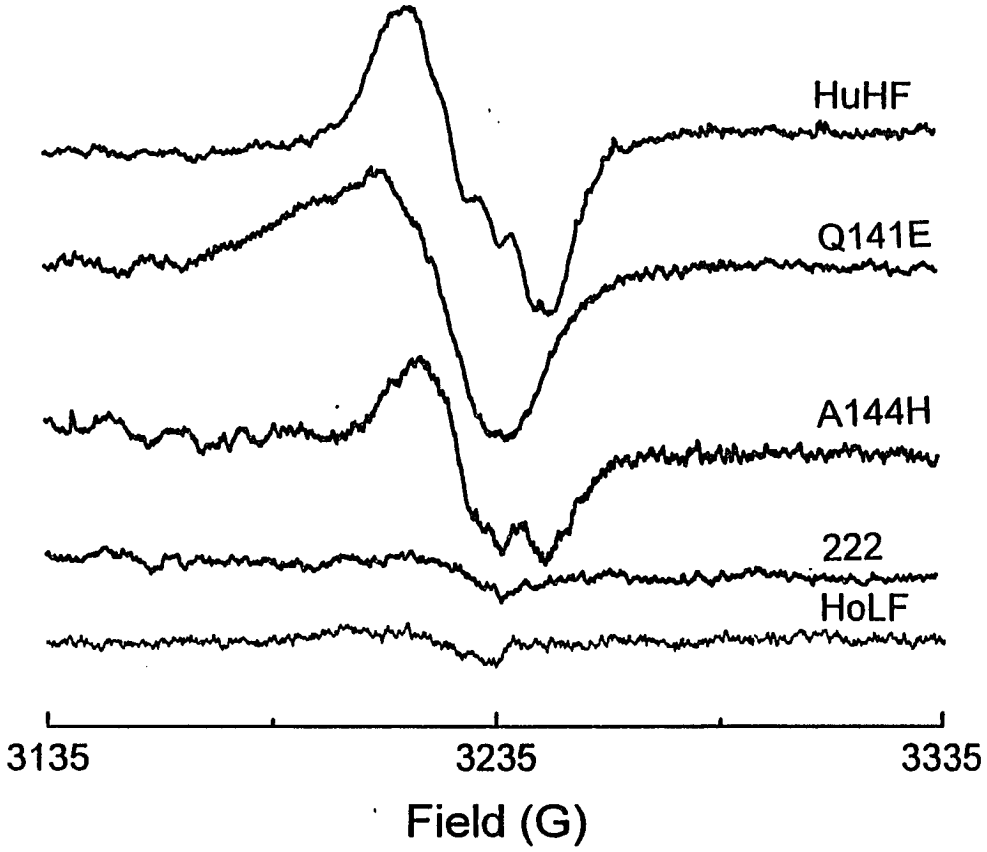

Figure 3.10: Radicals formed in the presence of HoLF, HuHF and HuHF variants, Q141E, A144H and 222. Sample preparation is the same as described in Figure 3.2a. Conditions are the same as described in Figure 3.4 except [Q141E] = 8.8, [A144H] = 8.8 μM, and [222] = 3 μM, and an Fe^{2+}/protein of 150 was maintained in all samples. The differences in protein concentration and instrumental gain setting were corrected for each spectrum. (File name: TYR34.org)

is related to iron ferroxidation. A144H, another HuHF variant, was shown only to reduce the amplitude of the HuHF radical spectrum, consistent with assumption that the residue Ala-144 is not involved in iron binding on the ferroxidase site in HuHF.

Establishing the specific amino acid residue on which the radical is centered is of great interest, since it may play a functional role in the process of iron deposition in the protein. The epr spectra of the HuHF radicals showed similarities to the reported tyrosine radicals from other proteins (Lassmann et al., 1991; Hallahan et al., 1992; Bender et al., 1989; King et al., 1967; Gerfen et al., 1993). Thus, several HuHF's variants with different tyrosine residue mutations, Y29F, Y32F, Y34F, were examined for radical formation (Figure 3.11). The characteristic tyrosine radical doublet (as marked by sticks) observed in the HuHF radical spectrum were preserved in Y29F and Y32F, but lost in Y34F, consistent with the observed radical being a Tyr-34 centered radical. The iron oxidation, however, has been shown to proceed in mutant Y34F at only a slightly reduced rate, suggesting that this tyrosyl radical may be the byproduct of the ferroxidation (Hempstead et al., 1994).

Figure 3.12 shows the epr spectra of the radicals generated with S-13 (W93F, K86Q), a mutant of the only tryptophan present in HuHF, Trp-93, and a control HuHF sample. The up field peak of the HuHF radical doublet is not clear in

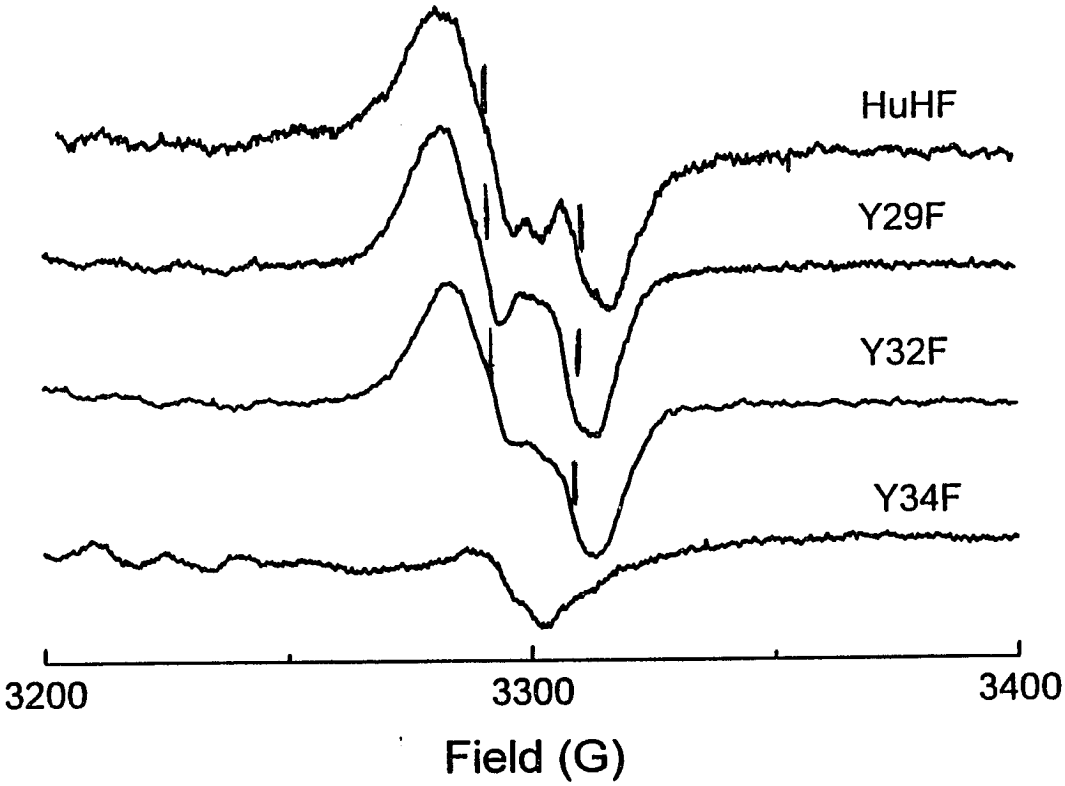

Figure 3.11: Radicals formed in the presence of HuHF and its tyrosine residue variants, Y29F, Y32F and Y34F. Sample preparation is the same as described in Figure 3.2a. Conditions are the same as described in Figure 3.4 except the concentrations of the Y29F and Y32F were 8.8 μM. An Fe^{2+}/protein of 150 was maintained in all samples, regardless of the protein concentrations. The differences in protein concentration and instrumental gain setting have been corrected for each spectrum. The field setting is 3300 G and the frequency is 9.2536 GHz. Hyperfine splittings were measured between the stick markers. (File name: Y2902.org)

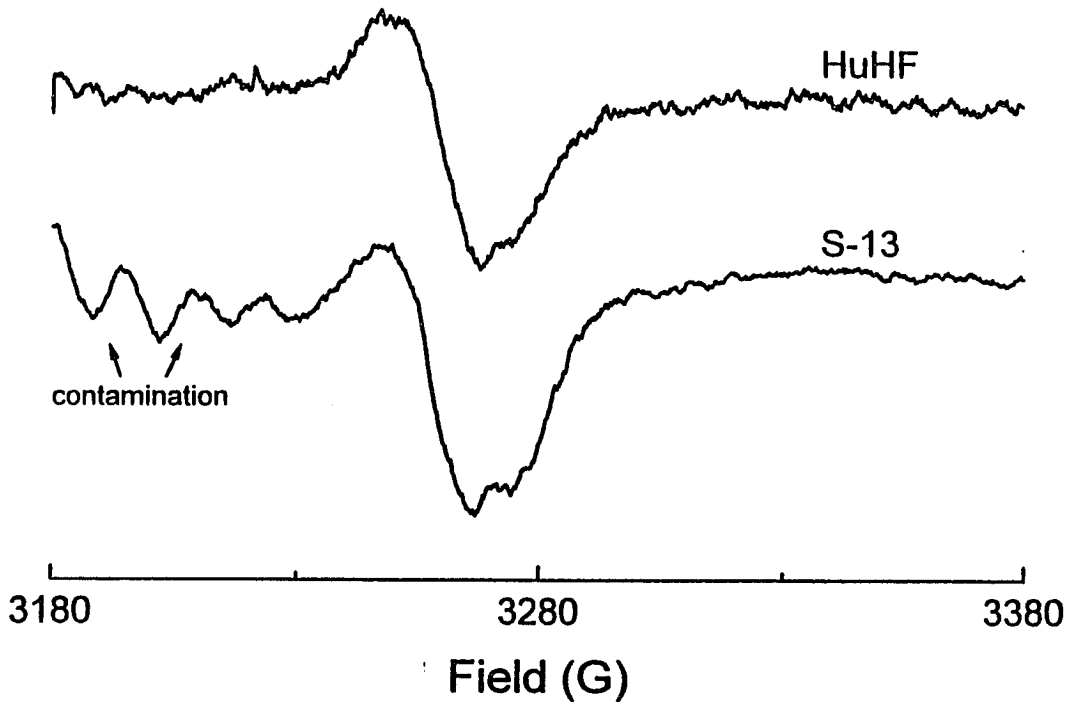

Figure 3.12: Radicals formed in the presence of HuHF and its Trp mutant, S-13. Sample preparation is as described in Figure 3.2a. Conditions are the same as described in Figure 3.4 except [HuHF] = 8.8 μM, [S-13] = 8.8 μM, and an Fe^{2+}/protein of 150 was maintained in both protein samples. Field setting 3280 G, power 10 mW and Frequency is 9.1498 GHz. (File name: S13.org)

either sample, possibly due to the decay of the signals during the sample preparation period. Nevertheless, the S-13 radical signal resembles that of the control, indicating that Trp-93 is probably not involved in radical formation in HuHF.

To investigate the radical formation site in HoSF, an iron ferroxidase site inhibitor, zinc, was employed (Sun & Chasteen, 1992; Sun et al., 1993; Treffry et al., 1993). In the presence of Zn^{2+}, a broad radical epr signal with unresolved hyperfine structure was observed and signal amplitude reduced by 75%, suggesting the ferroxidase center is also required for radical formation in HoSF, a finding in accord with the lack of radical formation in HoLF. Since the fine structured epr spectrum of the HoSF radical is also reminiscent of the tyrosine radicals reported in the literature but with a larger hyperfine splittings (Lassmann et al., 1991; Hallahan et al., 1992), it is possible that the HoSF radical observed in Figure 3.1b is also a tyrosine centered radical. But other aromatic radicals such as from histidine or tryptophan are not precluded by the data.

A bacterial ferritin, FTN (conventional type), in which the ferroxidase center, Tyr-34 and Gln-141 residues are conserved (Hempstead et al., 1994; Andrews et al., 1991) was examined for radical formation. A radical signal (g = 2.0064) showing similar fine structure to that of HoSF with smaller hyperfine couplings was observed (Figure 3.13). The hyperfine splitting of 8 G between all features and a ΔH_{Bpp} of 22 G were

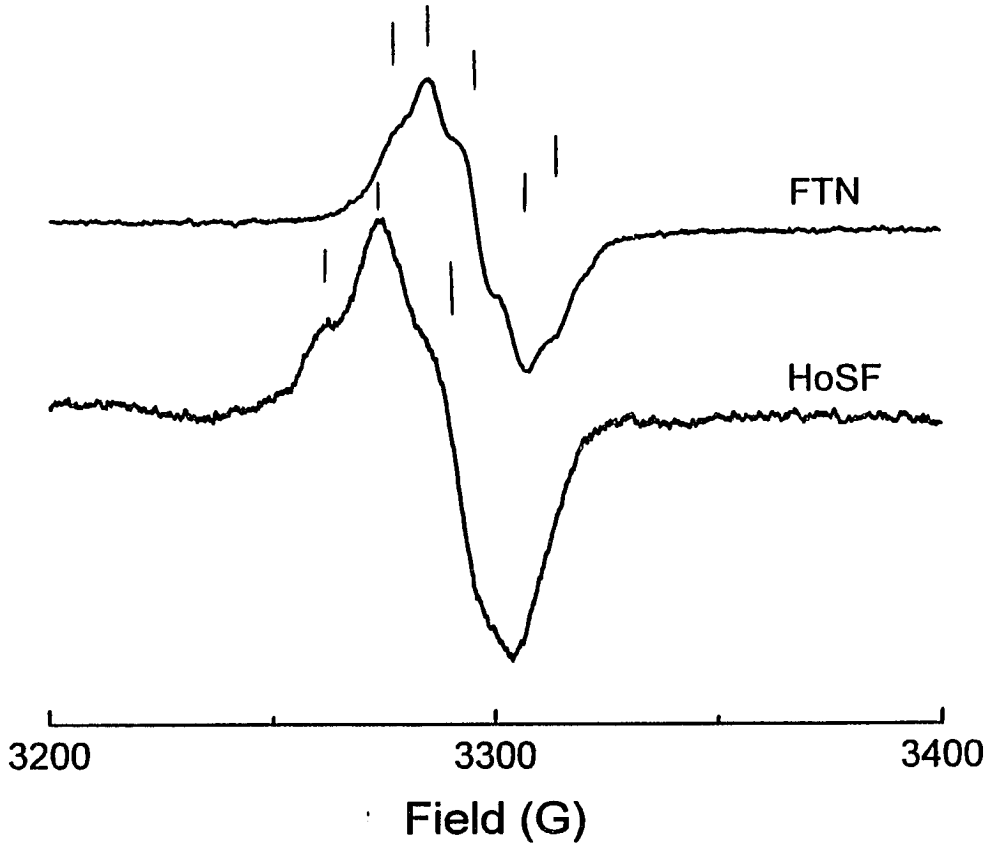

Figure 3.13: Radicals formed in the presence of HoSF and *E-coli* FTN. HoSF sample preparation is the same as described in Figure 3.1, FTN preparation is the same as described in Figure 3.2a. Conditions are the same as described in Figure 3.4 except [FTN] = 8.8 μM, an Fe^{2+}/protein of 150 was maintained in both protein samples. Hyperfine splittings were measured between the stick markers. (File name: FTNO2.org).

obtained, which are similar to those of a model tyrosine radical and the tyrosine radical observed in photosystem II (Barry et al., 1990; Hoganson et al., 1986; Petersen et al., 1990).

Functional Roles of Ferritin Radicals - Previously, it has been reported that the apoHoSF shell is redox active and undergoes a 6-electron redox reaction (Watt et al., 1992). A number of tyrosine residues associate with the 4-fold channel in HoSF have been postulated as the protein redox center where electrons are transferred between iron and protein during iron deposition to or mobilization from ferritin (Watt et al., 1992). An experiment was therefore undertaken, using ferricyanide oxidized and dithionite reduced HoSF in phosphate buffer, to investigate the possible role the HoSF radical may play in this redox process (Figure 3.14). Both protein samples revealed the same epr radical signal line shapes, amplitudes and g-factors (within experimental error), indicating the observed HoSF radical is not related to the redox states of the protein reported by Watt et al., (Watt et al., 1992).

Fenton Chemistry Related Ferritin Radicals

Ferritin Radicals Formed during Fe^{2+} Oxidation by H_2O_2 - Figure 3.15 shows the epr spectra of radicals formed in the presence of HoSF (A), HoLF (B) and FTN (C) when H_2O_2 is used in

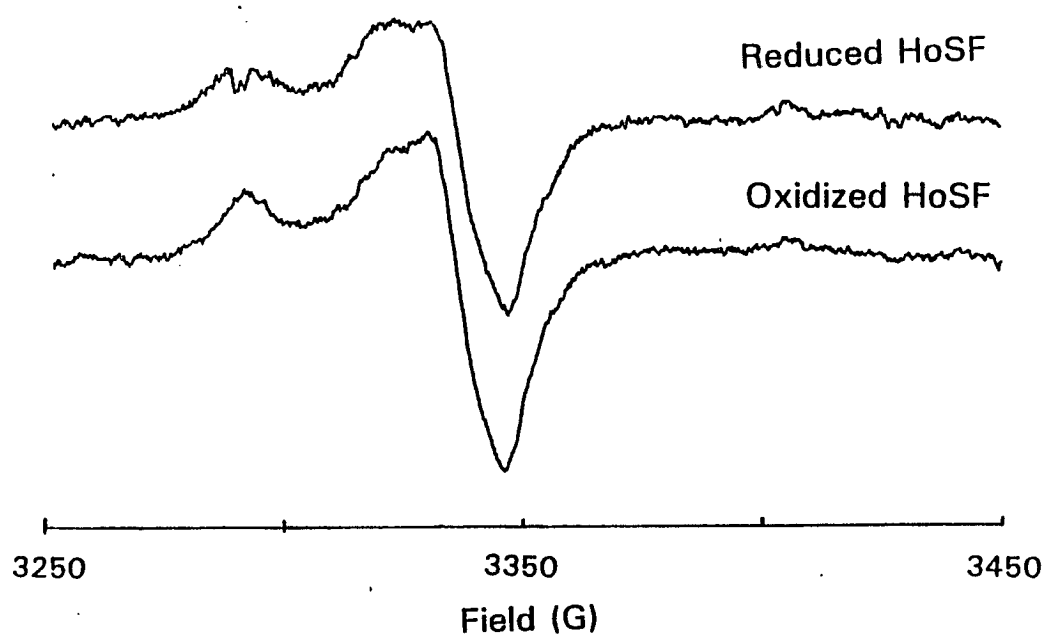

Figure 3.14: Radicals generated in the presence of oxidized and reduced HoSF in phosphate buffer. Sample preparation and conditions are the same as given in Figure 3.1. (File names: NOV2501.fls, NOV2502.fls)

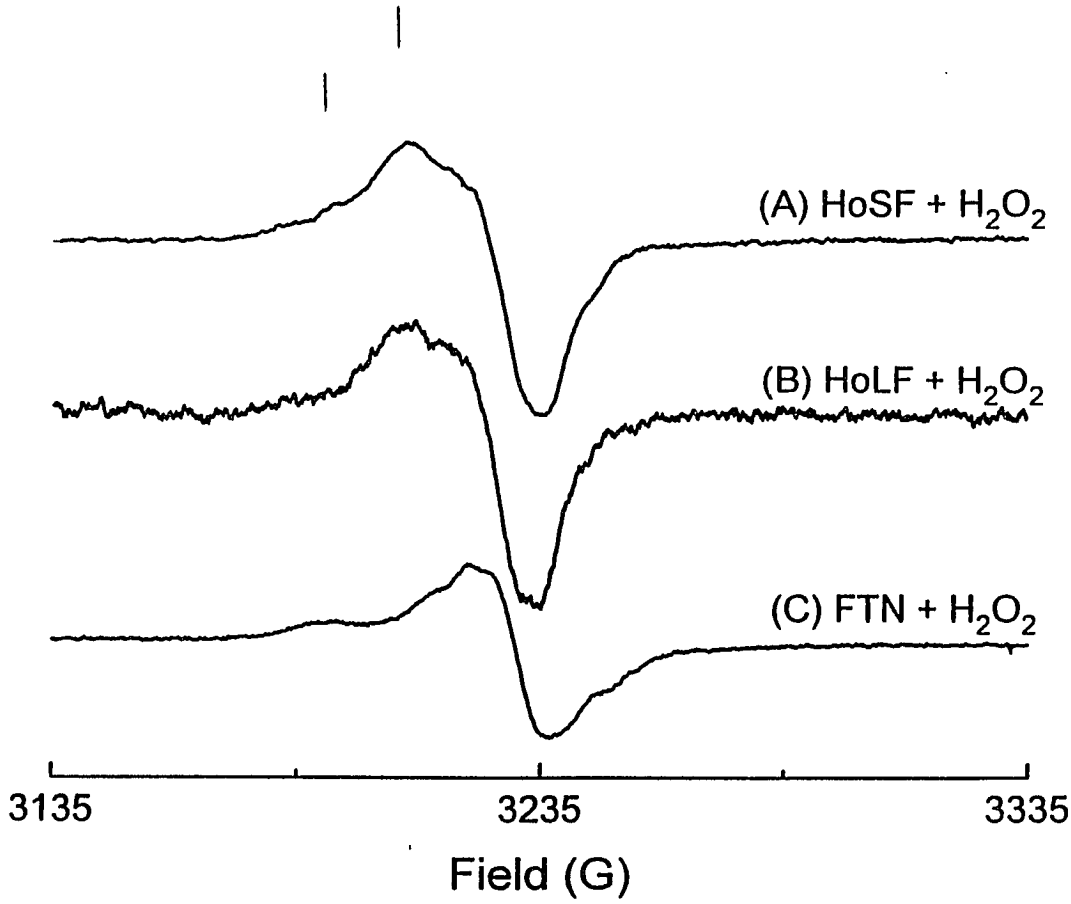

Figure 3.15: Radicals generated by H_2O_2 oxidation of Fe(II) in HoSF, HoLF and *E-coli* FTN. 1.32 mM Fe(II) was added to 250 μl of 8.8 μM protein solution in 50 mM MOPS and 0.15 N NaCl, pH 7.1, under moist Ar, followed by the addition of 5 μl 3% H_2O_2. The sample was then transfer to an Ar flushed epr tube before freezing in a dry ice - acetone bath. Spectral parameters are the same as described in Figure 3.4. Hyperfine splittings were measured between the stick markers. (File name: FTNH2O2.org).

place of O_2 as an Fe(II) oxidant. A fine structured radical signal (g = 2.0068, a = 12 - 14 G) was observed in HoSF which shows striking similarities to the HoSF radical formed in the presence of O_2 but with a 3 - 4 fold signal enhancement. When vanadyl, another Fenton chemistry promoting reagent (Carmichael, 1990), was used instead of iron to react with H_2O_2, a similar radical epr spectrum with a g factor of 2.0070 was observed. Thus, it appears that Fenton chemistry is involved in the radical formation in HoSF during iron oxidation by dioxygen. This result is consistent with the 40 - 50% HoSF radical signal inhibition observed when ceruloplasmin (ceruloplasmin/HoSF = 1), a protein that catalyzes Fe(II) oxidation without producing H_2O_2 (De Silva & Aust, 1992; De Silva et al., 1992), was present in Fe(II) oxidation by dioxygen.

When HoLF was exposed to the Fe(II)/H_2O_2 radical generating system, a radical signal that resembles that of HoSF is observed (Figure 3.15, spectrum B), indicating that the Fenton chemistry derived radical can be formed on the L-subunit as well.

When HuHF and its mutants, Y29F, Y32F, Y34F, Q141E, A144H and 222, were exposed to the Fe(II)/H_2O_2 system, radicals with epr spectra similar to that of HoSF in Figure 3.15 were observed in all HuHF variants with a value of 2.0064 $\pm$ 0.008 and hyperfine splittings of 12 - 14 G (Figure 3.16). These results suggest that this hydroxyl radical derived ferritin

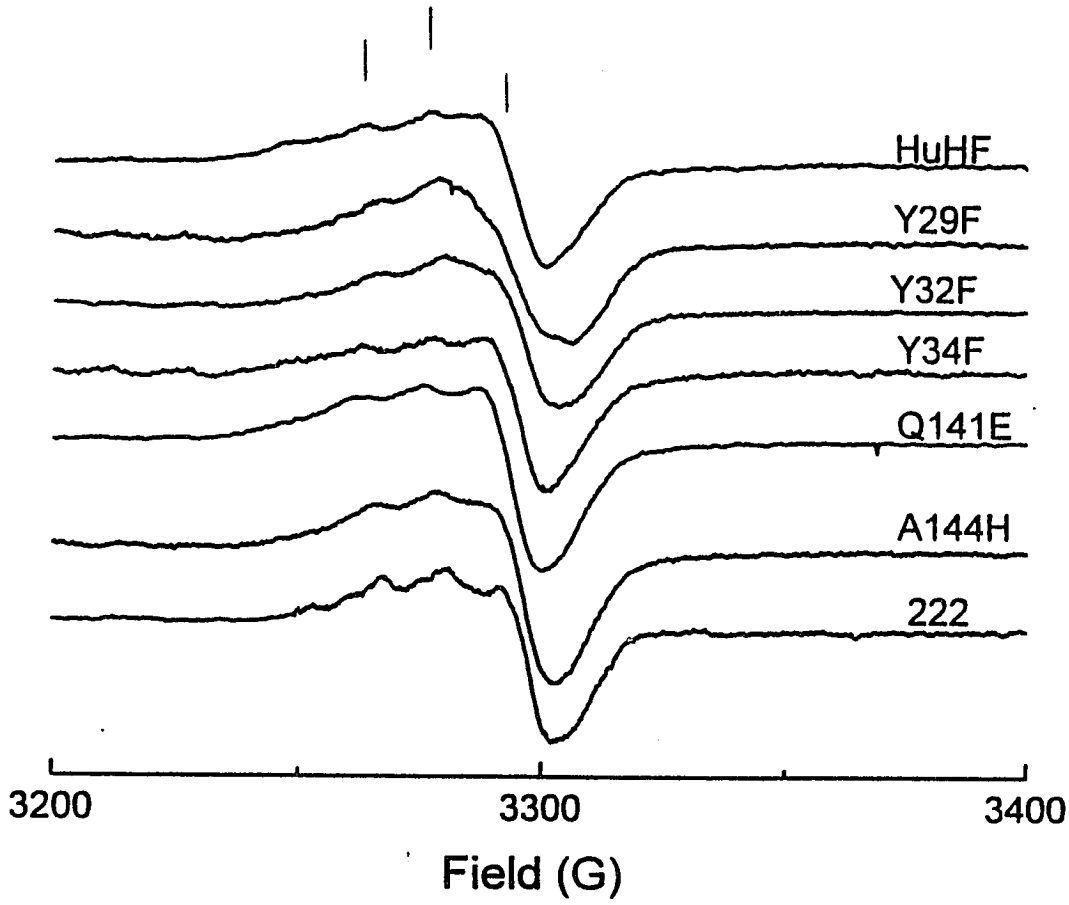

Figure 3.16: Radicals generated by H_2O_2 oxidizing Fe^{2+} loaded HuHF and its mutants, Y29F, Y32F, Y34F, Q141E and A144H. Sample preparation and spectral parameters are the same as described in Figure 3.15 except the field setting is 3300 and frequency is 9.2536 GHz Hyperfine splittings were measured between the stick markers. (File name: Y29H2O2.org).

radical is not formed at the ferroxidase site or its vicinity, not centered at Y29, Y32 or Y34 and it is not subunit specific.

Figure 3.15, spectrum C, shows a FTN radical epr signal generated by Fe(II)/H_2O_2. A fine structured epr signal with g = 2.0067 and a = 7 G were observed, which has different line shapes to the FTN radical observed in the presence of dioxygen (Figure 3.13). In addition, the radical signal amplitude did not increase when H_2O_2 was used instead of dioxygen, suggesting the FTN radical may not be derived from Fenton chemistry directly.

OH· Radical Damage to Ferritin - In HoSF the amino acid residue lysine has been reported to be depleted during iron oxidative deposition, resulting in an increase in the protein isoelectric focusing point (De Silva et al., 1992). To examine the correlation between protein damage and hydroxyl derived radical formation, the amino acid composition of the protein sample subjected to radical signal generation by Fe(II)/H_2O_2 was analyzed. A 21% reduction in histidine residue concentration (2.81 moles% (n = 1) *vs.* control of 3.57 $\pm$ 0.05 mole%) was observed when a HoSF sample was treated with Fe(II)/H_2O_2 repeatedly (6 times) at an Fe(II)/HoSF ratio of 150. The corresponding radical epr signal was reduced 52%, indicating that the observed ferritin radical is related to OH· damage to the protein. No amino acid composition change has

been observed for the protein samples that underwent radical generation only once, indicating that the ferritin molecule is relatively robust against damage from iron derived oxy radicals.

PBN Spin Trapped Ferritin Radicals

Figure 3.17 shows the room temperature epr spectrum of HoSF radicals as adducts of the PBN, in MOPS buffer. An immobilized anisotropic PBN adduct signal with $2a_{//}$ of 67.2 ± 0.4 G and a set of isotropic PBN signals with nitrogen and hydrogen splittings of a_N = 16.28 ± 0.09 G and a_H = 3.62 ± 0.09 G were clearly observed (spectrum A). The immobility of the PBN adduct suggests that a large molecule, presumably a ferritin based radical, is attached to the spin trap reagent. Retention of the immobilized signal by an XM 300 membrane (spectrum C) and partial retention of the isotropic signal by a UM 5 membrane (spectrum B) indicate that radicals from both presumed small peptide fragments and the whole protein are formed. The a_N and a_H of the isotropic signal were checked against known PBN adduct parameters in the database STBII (Li et al., 1988) and no match was found. They are assigned to an unknown ferritin fragment radical.

Figure 3.18 shows formation of the spin trapped radicals as a function of iron loading into HoSF. An increasing radical signal with increasing iron loading in ferritin was observed. Radical production appeared to reach a plateau at

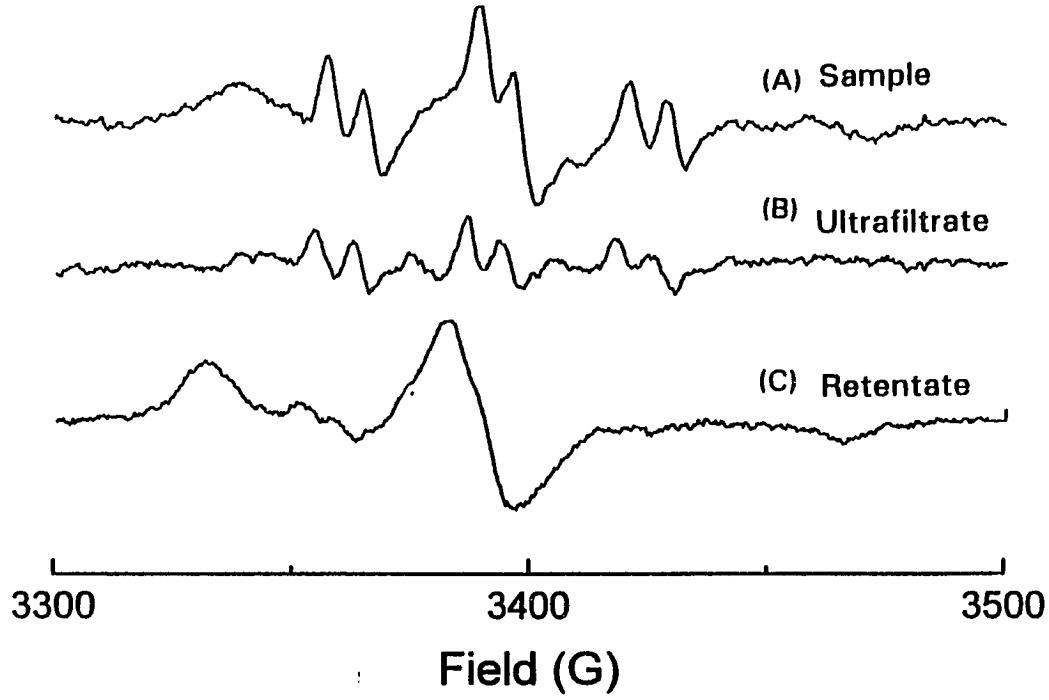

Figure 3.17: Separation of the PBN-R adducts by ultrafiltration with an XM 300 membrane. 17 μM HoSF was incubated with 50 mM PBN and 0.15 M NaCl, 50 mM MOPS buffer, pH 7.4, for 40 minutes prior to the addition of 150 Fe(II)/protein. The sample was then exposed to 1 atm O_2 for 4 minutes before it was transferred to an aqueous solution epr flat cell for epr measurement at room temperature. Spectral parameters are the same as given in Figure 3.1 except the field setting is 3400 G and the frequency is 9.52727 GHz. (File name: MAY0502.fls, MAY0405.fls, M196.fls)

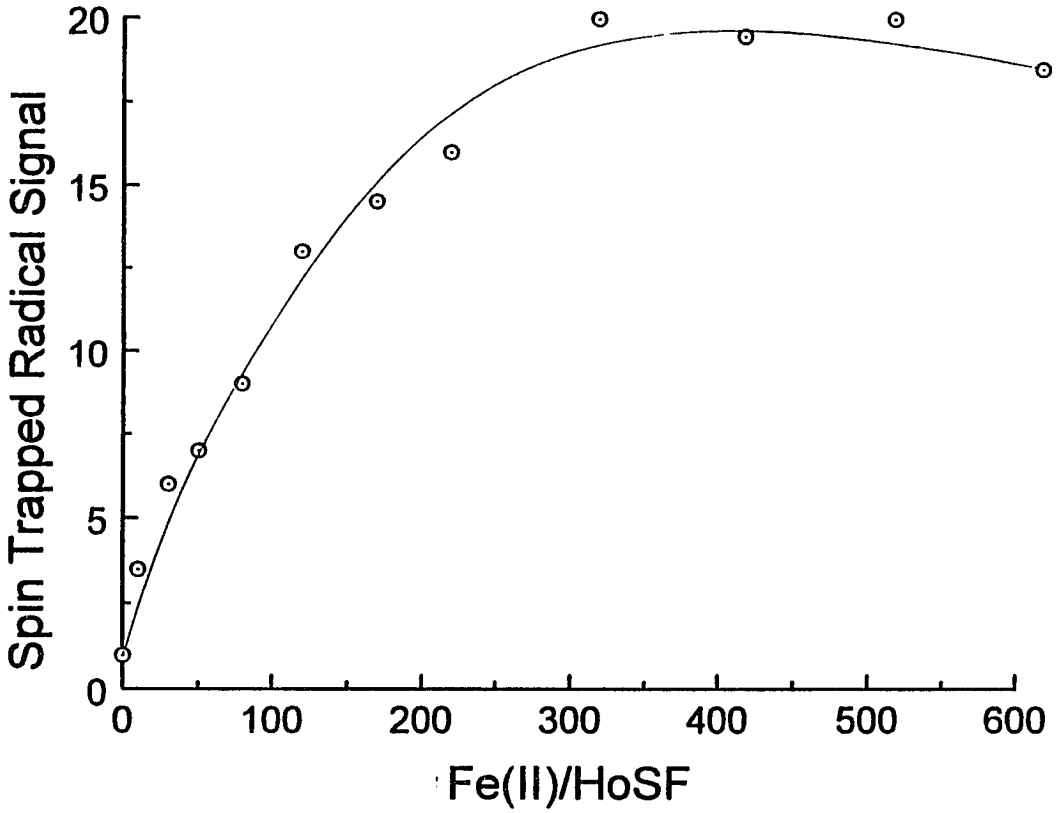

Figure 3.18: Accumulated epr signal of the PBN-R adduct as a function of the iron loading. Sample preparation and conditions are the same as describe in Figure 3.17. The same sample was used to repeatedly add various amount of stock 0.1 M FeSO4. (File name: PBN.org)

300 Fe(II)/HoSF, suggesting that the radical formation occurs only during the initial stages of iron deposition, *i.e.* when H_2O_2 is formed in the greatest amount.

A previous spin trap study for HoSF radicals revealed only the isotropic PBN signal (Grady et al., 1989), not the immobilized signal seen here. An experiment was thus carried out to compare the previous and current radical generating methodologies. Figure 3.19 shows the radicals generated by the addition of Fe(II) to an air (A), O_2 (B), and Ar (C) saturated protein samples followed by their exposure to 1 atm O_2 for 4 minutes. Methods A and C represent the previous and current radical generation methods, respectively. The epr spin trapped signal amplitude follows the order C > B > A, possibly due to less Fe(II) binding to protein in (A) and (B) prior to the Fe(II) oxidation. The low signal to noise level of the spectrum A compared to C may account for the lack of observation of an immobilized signal in the previous study (Grady et al., 1989).

Ferritin Radical Generated by $K_3Fe(CN)_4$

A ferritin radical was also observed when $K_3Fe(CN)_4$ was added directly to an apoHoSF sample (Figure 3.20). A singlet with no hyperfine structure was observed with a g = 2.0050 $\pm$ 0.0005 and ΔH_{Bpp} of 15 $\pm$ 0.4 G (n = 5). A $P_{1/2}$ value of 10.84 $\pm$ 3.15 mW and a b of 0.98 $\pm$ 0.08 were obtained from the data shown in Figure 3.21 inset (measured on E-4 spectrometer). A

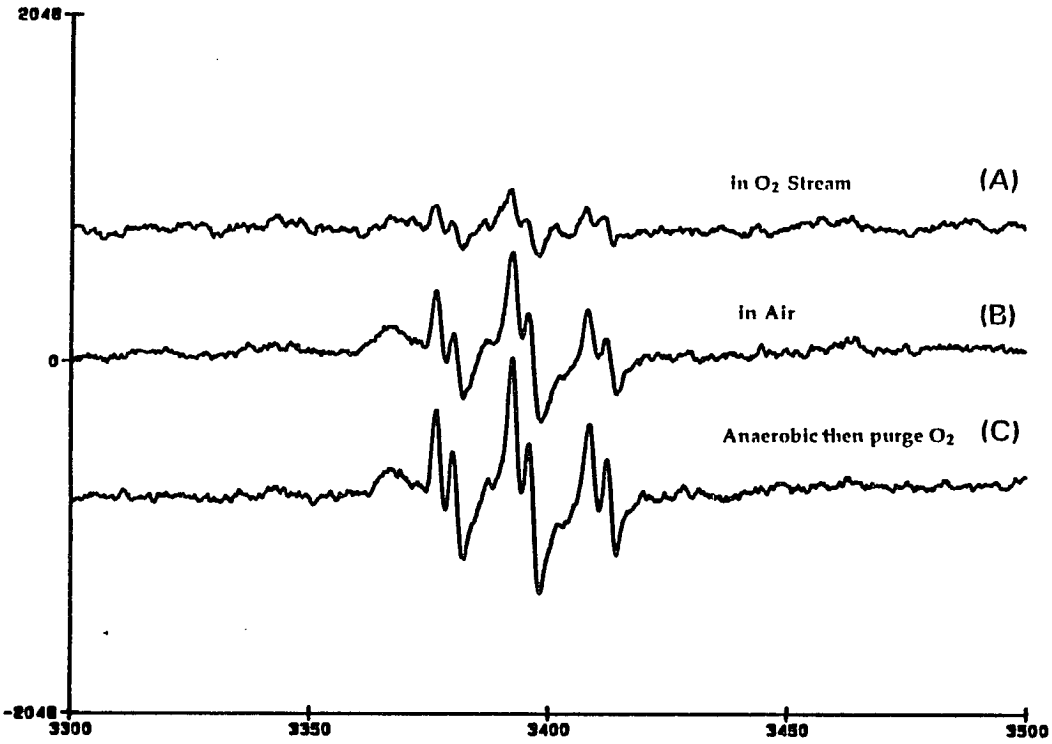

Figure 3.19: Spin trapped epr signals generated under different conditions. Fe^{2+} was added to an oxygen (A), air (B) and Ar (C) saturated HoSF sample solution before it was exposed to O_2 for 4 minutes. Sample preparation and conditions are the same as described in Figure 3.17 except phosphate was used instead of MOPS buffer. (File name: Jun0506.fls, Jun0505.fls, Jun0503.fls)

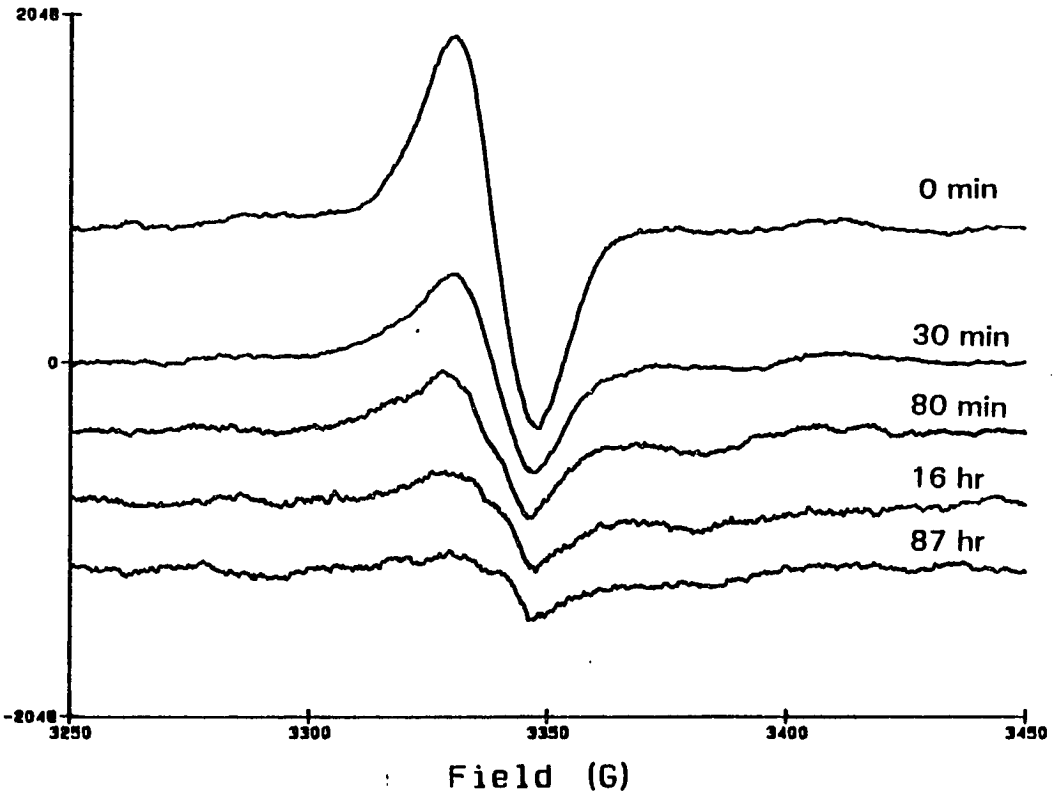

Figure 3.20: Epr signal of the HoSF radical generated in the presence of $K_3Fe(CN)_4$. 25 mM $K_3Fe(CN)_4$ was added to 300 μl of Ar dearaed 42 μM HoSF sample solution in 50 mM phosphate and 0.15 N NaCl, pH 7.4, for 3 minutes. The sample was then frozen in dry ice - acetone bath and the epr measurement was carried out at 77 K. Spectral parameters are the same as described in Figure 3.1. (File names: SEP0401.fls, SEP0902.fls, SEP0908.fls, SEP1001.fls, SEP1705.fls)

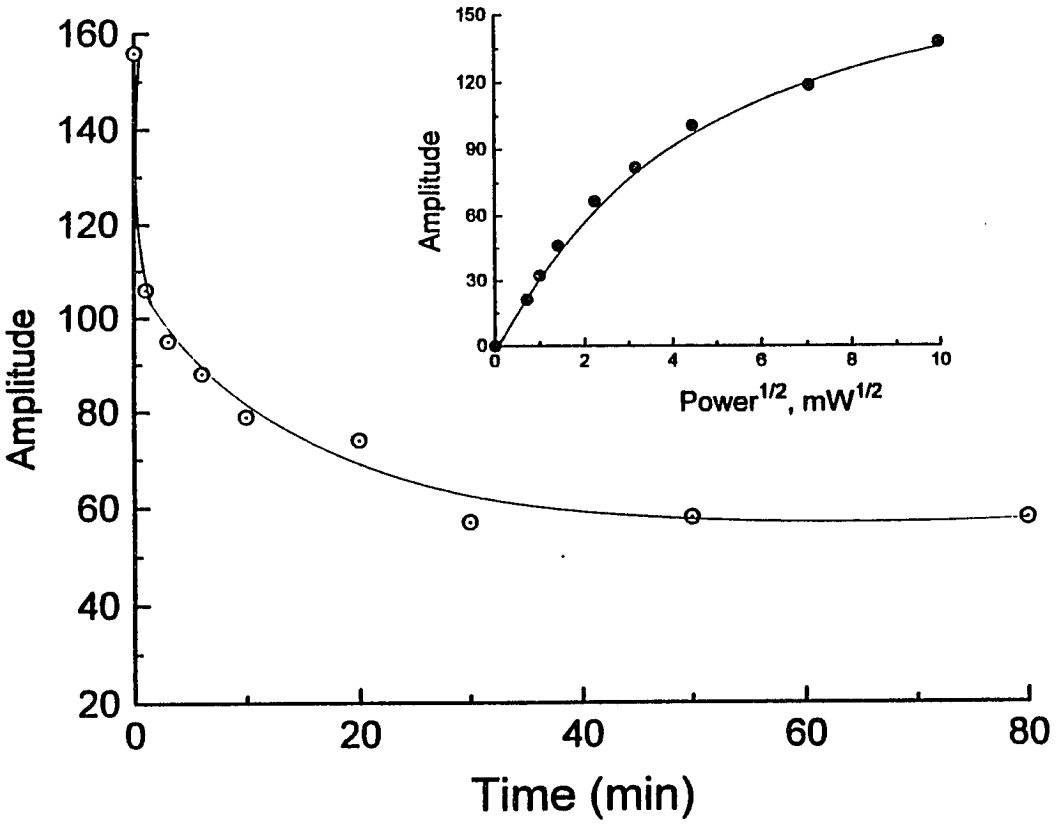

Figure 3.21: Time course for the decay of the HoSF radical generated in the presence of $K_3Fe(CN)_4$. Inset: Power saturation of the HoSF radical formed in the presence of $K_3Fe(CN)_4$. Sample preparation spectral parameters are the same as described in Figure 3.20. $P_{1/2}$ and b were obtained from the curve fit to the equation described in the "Material and methods" section. Power saturation experiment was performed in E-4 spectrometer and the $P_{1/2}$ and the b were calibrated against the parameters obtained from the E-9 spectrometer.

2-phase radical decay with half lives of 1 and 9 minutes were obtained from Figure 3.21.

Discussion

In this work, several radical species have been observed during iron oxidative deposition into ferritin. A radical species formed in HuHF is evidently a tyrosine radical which does not appear to be Fenton chemistry related (Figure 3.4). A different ferritin radical species was observed in HoSF and it is likely the result of $OH^{\cdot}$ damage to protein (Figure 3.1b). A third radical species was observed in E-coli ferritin (non-heme type) which does not appear to be a Fenton chemistry related radical, but gives an epr line shape reminiscent of that observed in HoSF with a slightly different ΔH_{Bpp} and hyperfine splittings (Figure 3.15).

Locating the site of radical formation is one objective of this research. The radical formed in HuHF originates from the iron ferroxidation in ferritin and perhaps is a secondary radical derived from superoxide radical formation at the ferroxidase site, an idea consistent with the proposed iron deposition Mechanism III where superoxide is formed as an intermediate species of the dioxygen reduction at the ferroxidase site (Sun & Chasteen, 1992) (Chapter II). Failure to detect peroxyl or superoxide radical hyperfine splittings when using $^{17}O_2$ as Fe(II) oxidant is probably due to the formation of an epr silent species with a net electron spin of

S = 2 when the superoxide (S = 1/2) is near or bound to the Fe^{3+} (S = 5/2).

The HuHF radical is evidently a Tyr-34 centered radical based on both the radical epr parameters and the site directed mutant studies (Figure 3.11). This Tyr-34 radical seems to correlate with the characteristic UV absorbance of the Fe(III)-tyrosinate complex at 550 nm. All mutants which failed to generate the characteristic tyrosine radical doublet in the epr spectra (Figure 3.10 & 3.11) were also found to have no absorbance at this UV region (Harrison, unpublished results). However, the Fe(III)-Tyr complex and Tyr-34 radical do not form in the same time scale. The Fe(III)-tyrosine complex was reported to form within 3 - 10 seconds of initiation of iron oxidation (Waldo & Theil, 1993) while the fine structured Tyr-34 signal does not appear until 1.5 minutes after the reaction was initiated. Thus, either the tyrosine radical is a byproduct, produced after Fe(III)-Tyr complex formation, or the Tyr-34 radical is epr silent at early stages of its formation due to the presence of Fe(III) at or near the Tyr-34 site, resulting in the lack of an epr spectrum.

The HoSF radical (Figure 3.1) formed during Fe(II) oxidation by dioxygen is most likely a secondary radical derived from the hydroxyl radical reaction with the protein, based on the similarities in radical epr spectra and the enhancement of the signal amplitude when H_2O_2 is used in place

of dioxygen to promote the Fenton chemistry (Figure 3.2b & 3.15). Formation of the HoSF radical requires the ferroxidase site on the H-subunit but the location of the radical is not subunit specific, provided that H_2O_2 is present in the sample (Figure 3.1, 3.15, 3.16). It is conceivable that the H-subunit is the source of H_2O_2 production, probably during iron ferroxidation, and the L-subunit is the sink for hydroxyl radical damage. This is consistent with recent findings showing a clear depletion of the L-subunit by SDS-PAGE when 35 - 45 consecutive oxidations of 50 Fe(II)/protein were conducted in HoSF (Grady and Chasteen, unpublished result). A function for the L-subunit as a $OH^{\cdot}$ radical sink may be biologically important, since such a function could prevent hydroxyl radical damage to the ferroxidase site on the H-subunit, thus protecting the capability of HoSF to carry out iron oxidation.

The Fenton chemistry related HoSF radical does not appear to form at random protein residues based on the dramatic reduction of the HoSF radical signal when Fe(II)/EDTA/H_2O_2, a random hydroxyl radical generating system, was employed. Thus, it appears that the H_2O_2 is produced at the ferroxidase site then is released to another iron binding site, perhaps on the L-subunit, where the bound Fe^{2+} undergoes the Fenton chemistry to generate the HoSF radical with fine structured signal (Figure 3.1B). A similar mechanism of hydroxyl radical damage to protein probably exists in the HuHF as well, but is

less predominant, due to the much faster iron oxidation rate in HuHF than in HoSF, resulting in much less ferrous iron available for the Fenton reaction at the experimental conditions used. The weak radical signal observed in Y34F, a HuHF mutant which slightly attenuates the iron oxidation rate (Hempstead et al., 1994), perhaps comes from the radicals produced in Fenton chemistry (Figure 3.11). The Fenton chemistry related radical signal in HuHF perhaps would be more apparent if Fe(II) was added incrementally over a period of time, a situation that may be closer to the natural process.

The amino acid residue(s) responsible for the hydroxyl radical related ferritin radical is difficult to establish, however, it appears to be conserved in both HoLF and HuHF. The radical epr signal line shape and g factors are reminiscent of the tyrosine radicals reported in other proteins (Lassmann et al., 1991), but it cannot be Tyr-29, Tyr-32 or Tyr-34 based on the studies using site directed mutants (Figure 3.16). Other tyrosine residues conserved in both HuHF and HoLF include Tyr-12, Tyr-40 and Tyr-168 but are not in the vicinity of any known iron binding sites (Andrews et al., 1991; Lawson et al., 1991), and are thus unlikely to be responsible for the radical observed. A histidine based radical (g = 2.009 (King et al., 1967)) has been reported to give epr line shapes similar to that of the tyrosine radical (Boussac & Rutherford, 1992; Nelson, 1988). Thus, it is possible that the HoSF radical is a histidine based radical,

perhaps His-118. His-118 (His 119 for FTN) is conserved in both the H and L subunits and it has been shown to be an iron binding site (Chasteen et. al, unpublished results) (Gerfen et al., 1991; Hanna et al., 1991a). The idea of a Fenton chemistry derived radical being a histidine centered radical is consistent with the slight reduction in histidine amino acid composition when ferritin is attacked by hydroxyl radical repeatedly as observed in this work and another study (De Silva et al., 1992).

The HoSF axial radical formed at early stages of iron oxidation does not appear to be related to the fine structured HoSF radical signal observed on a longer time scale, since the axial radical, monitored through the A_1 feature, decreases (2 min) before the fine structured radical signal increases (4 minutes) (Figure 3.2). It, however, is thought to be the same radical species as observed in the rapid freeze quench study of the initial iron oxidation (Sun and Chasteen, 1994). The slight difference in g factors, $g_{/\!/}$ of 2.042 and $g_{\perp}$ of 2.0033 in previous work (reaction time 5.4 s) *vs.* g (A_1) = 2.0379 and g (A_2) of 2.0056 from this work, is probably caused by the formation of the fine structured radical signal due to the longer reaction time (1 min) used in this work. It is possible that the radical with the axial signal was formed during the initial iron ferroxidation, and it is related to the superoxide formation. Perhaps the radical with the axial signal is also centered near the Tyr-34 residue, as observed

in the HuHF, although the Tyr-34 radical observed in the HuHF has a slightly slower decay time (6 min for the fine structured radical signal to disappear) than the axial radical signal observed in the HoSF (2 min for the axial signal to diminish).

The slow generation of the fine structured HoSF radical signal (Figure 3.2b) could be caused by the slow accumulation of H_2O_2 at the radical formation site or the formation of the epr silent Fe^{3+}-radical species during the initial stages of iron deposition into the core, or both. The Fe^{3+}-radical species may be decoupled after the Fe^{3+} migrates to the ferric core, resulting in the detection of the radical, in accord with the 20 - 30 minutes required for the fine structure radical signal to reach maximal intensity (Figure 3.3).

The HoSF radicals formed in the presence of phosphate and MOPS buffer are likely to be the same radical species based on their epr lineshapes, g factors and power saturation behaviors. The difference in radical epr lineshapes may be simply due to changes in the geometry of the tyrosine phenol ring (Barry et al., 1990; DeGray et al., 1992).

Similar radical epr line shapes but different hyperfine splittings and ΔH_{Bpp}s are observed in HoSF and FTN. The parameters observed in FTN are in good agreement with typical tyrosine radicals observed in other proteins (Russell & Harrison, 1978; Sun et al., 1993). The slightly larger hyperfine splittings observed in HoSF may be due to mixed

radical signals superimposed onto one another, consistent with the separation of the HoSF radical signals by Q-band epr. However, more accurate radical hyperfine couplings could not be obtained from the Q-band epr spectrum due to significant background noise.

In conclusion, two types of radicals have been identified in iron oxidative deposition into ferritin. One, a Tyr-34 radical, is formed on HuHF only and is possibly related to the superoxide radical formation. The other type is likely a Fenton chemistry derived radical formed in HoSF, perhaps the result of the H_2O_2 translocating to the L-subunit where Fe^{2+} is bound. The HoSF radical does not seem to be functionally important. The radical formation process may serve as a mechanism to protect HoSF itself from iron toxicity by preserving the ferroxidase site intact. The HuHF radical, does not appear to affect the rate of iron ferroxidation, but it may serve as an electron reservoir for oxidizing incoming Fe(II).

REFERENCES

Adams, R.E., Betso, S.R., & Carr, P.W. (1994) *Anal. Chem. 48(13)*, 1989.

Afanas'ev, Igor B. (1989) in *Superoxide Ion: Chemistry and Biological Implications Volume I* (pp 197-225, CRC Press, Boca Raton.

Andrews, S.C., Smith, J.M.A., Yewdall, S.J., Guest, J.R., & Harrison, P.M. (1991) *FEBS Lett. 293*, 164.

Andrews, S.C., Arosio, P., Bottke, W., Briat, J.F., Von Darl, M., Harrison, P.M., Laulhere, J.P., Levi, S., Lobreaux, S., & Yewdall, S.J. (1992) *J. Inorg. Biochem. 47*, 161.

Arosio, P., Adelman, T.G., & Drysdale, J.W. (1978) *J. Biol. Chem. 253(12)*, 4451.

Bakker, G.R. & Boyer, R.F. (1986) *J. Biol. Chem. 261*, 13182.

Barry, B.A., El-Deeb, M.K., Sandusky, P.O., & Babcock, G.T. (1990) *J. Biol. Chem. 265*, 20139.

Bauminger, E.R., Harrison, P.M., Hechel, D., Nowik, I., & Treffry, A. (1991) *Biochim. Biophys. Acta 1118*, 48.

Bauminger, E.R., Harrison, P.M., Hechel, D., Nowik, I., & Treffry, A. (1992) *Hyper. Inter. 71*, 1287.

Bauminger, E.R., Harrison, P.M., Hechel, D., Nowik, I., & Treffry, A. (1993) *Nucl. Instrum. Meth. Phys. Res. B 76*, 1.

Bender, C.J., Sahlin, M., Babcock, G.T., Barry, B.A., Chandrashekar, T.K., Salowe, S.P., Stubbe, J., Lindstrom, B., Petersson, L., Ehrenberg, A., & Sjoberg, B. (1989) *J. Am. Chem Soc. 111(21)*, 8076.

Bolann, B.J. & Ulvik, R. (1990) *Eur. J. Biochem. 193*, 899.

Bolann, B.J. & Ulvik, R.J. (1993) *FEBS Lett. 318*, 149.

Boussac, A. & Rutherford, A.W. (1992) *Biochemistry 31*, 7441.

Burkitt, M.J. & Gilbert, B.C. (1991) *Free Radical. Res. Commun. 14*, 107.

Carmichael, A.J. (1990) *FEBS Lett. 261;1*, 165.

Chasteen, N.D. & Theil, E.C. (1982) *J. Biol. Chem. 257*, 7672.

Cheng, Y.G. & Chasteen, N.D. (1991) *Biochemistry 30*, 2947.

Clegg, G.A., Fitton, J.E., Harrison, P.M., & Treffry, A. (1980) *Prog. Biophys. Molec. Biol. 36*, 1.

Cozzi, A., Santambrogio, P., Levi, S., & Arosio, P. (1990) *FEBS Lett. 277*, 119.

Crichton, R.R. (1973) in *STRUCTURE AND BONDING, Volume 17*, (Duanitz, J.D. et al. Eds.) pp. 67-134, SPRINGER-VERLAG, BERLIN.

Crichton, R.R., Roman, F., Roland, F., Paques, E., Paques, A., & Vandamme, E. (1980) *J. Mol. Cat. 7*, 267.

Crichton, R.R. & Roman, F. (1978) *J. Mol. Cat. 4*, 75.

Crichton, R.R. & Ward, R.J. (1992) *Biochemistry 31*, 11255.

Davies, M.J., Gilbert, B.C., & Haywood, R.M (1991) *Free Rad. Res. Comms. 15(2)*, 111.

de Paula, J.C. & Brudvig, G.W. (1985) *J. Am. Chem. Soc. 107*, 2643.

De Silva, D., Miller, D.M., Reif, D.W., & Aust, S.D. (1992) *Arch. Biochem. Biophys. 293*, 409.

De Silva, D. & Aust, S.D. (1992) *Arch. Biochem. Biophys. 298*, 259.

DeGray, J.A., Lassmann, G., Curtis, J.F., Kennedy, T.A., Marnett, L.J., Eling, T.E., & Mason, R.P. (1992) *J. Biol. Chem 267*, 23583.

Feig, A.L. & Lippard, S.J. (1993) *Coord. Chem. Rev.* 1.

Fontecave, M. & Pierre, J.L. (1993) *Biochimie 75*, 767.

Ford, G.C., Harrison, P.M., Rice, D.W., Smith, J.M.A., Treffry, A., White, J.L., & Yariv, J. (1984) *Phil. Trans. R. Soc. Lond. 304*, 551.

Gerfen, G.J., Hanna, P.M., Chasteen, N.D., & Singel, D.J. (1991) *J. Am. Chem. Soc. 113*, 9513.

Gerfen, G.J., Bellew, B.F., Un, S., Bollinger, J.M.,Jr., Stubbe, J., Griffin, R.G., & Singel, D.J. (1993) *J. Am. Chem Soc. 115*, 6420.

Goto, K., Tamura, H., & Nagayama, M. (1970) *Inorg. Chem. 9*, 963.

Grady, J.K., Chasteen, N.D., & Harris, D.C. (1988) *Anal. Biochem. 173*, 111.

Grady, J.K., Chen, Y., Chasteen, N.D., & Harris, D.C. (1989) *J. Biol. Chem. 264*, 20224.

Grady, J.K. & Chasteen, N.D. (1990) in *Iron Biominerals* (Frankel, R.B. & Blakemore, R.P., Eds.) pp 315-323, Plenum Press, New York.

Graf, E., Mahoney, J.R., Bryant, R.G., & Eaton, J.W. (1984) *J. Biol. Chem. 259*, 3620.

Guiles, R.D., Zimmermann, J.L., McDermott, A.E., Yachandra, V.K., Cole, J.L., Dexheimer, S.L., Britt, R.D., Wieghardt, K., Bossek, U., Sauer, K., & Klein, M.P. (1990) *Biochemistry 29*, 471.

Hallahan, B.J., Nugent, J.H.A., Warden, J.T., & Evans, M.C.W. (1992) *Biochemistry 31(19)*, 4562.

Halliwell, B. & Gutteridge, J.M.C. (1984) *Biochem. J. 219*, 1.

Halliwell, B. & Gutteridge, J.M.C. (1985) *Molec. Aspects. Med. 8*, 89.

Halliwell, B. & Gutteridge, J.M.C. (1988) *ISI Atlas of Science: Biochemistry* 48.

Hanna, P.M., Chasteen, N.D., Rottman, G.A., & Aisen, P. (1991a) *Biochemistry 30*, 9210.

Hanna, P.M., Chen, Y., & Chasteen, N.D. (1991b) *J. Biol. Chem. 266*, 886.

Harrison, P.M. (1986) *Biochem. Educ. 14*, 154.

Harrison, P.M., Treffry, A., & Lilley, T.H. (1986) *J. Inorg. Biochem. 27*, 287.

Hempstead, P.D., Hudson, A.J., Artymiuk, P.J., Andrews, S.C., Banfield, M.J., Guest, J.R., & Harrison, P.M. (1994) *FEBS Lett. 350*, 258.

Heqing, H., Watt, R.K., Frankel, R.B., & Watt, G.D. (1993) *Biochem. 32*, 1681.

Hoganson, C.W., Demetriou, Y., & Babcock, G.T. (1986) in

Progress in Photosynthesis Research: Proceedings of the VIIth International Congress on Photosynthesis, Providence, Rhode Island, USA, August 10-15, 1986 (Biggins, J., Ed.) pp I.5.479-I.5.482, Martinus Niijhoff Publishers, Dordrecht, The Netherlands.

Jacobs, D.L., Watt, G.D., Frankel, R.B., & Papaefthymiou, G.C. (1989a) *Biochemistry 28*, 1650.

Jacobs, D.L., Watt, G.D., Frankel, R.B., & Papaefthymiou, G.C. (1989b) *Biochemistry 28*, 9216.

King, N.K., Looney, F.D., & Winfield, M.E. (1967) *Biochim. Biophys. Acta 133*, 65.

Kurimura, Y., Ochiai, R., & Matsuura, N. (1968) *Bull. Chem. Soc. Jpn. 41*, 2234.

Kurimura, Y. & Kuriyama, H. (1969) *Bull. Chem. Soc. Jpn. 42*, 2238.

Lassmann, G., Odenwaller, R., Curtis, J.F., DeGray, J.A., Mason, R.P., Marnett, L.J., & Eling, T.E. (1991) *J. Biol. Chem 266(30)*, 20045.

Lawson, D.M., Treffry, A., Artymiuk, P.J., Harrison, P.M., Yewdall, S.J., Luzzago, A., Cesareni, G., Levi, S., & Arosio, P. (1989) *FEBS Lett. 254*, 207.

Lawson, D.M., Artymiuk, P.J., Yewdall, S.J., Smith, J.M.A., Livingstone, J.C., Treffry, A., Luzzago, A., Levi, S., Arosio, P., Cesareni, G., Thomas, C.D., Shaw, W.V., & Harrison, P.M. (1991) *Nature 349*, 541.

Levi, S., Salfeld, J., Franceschinelli, F., Cozzi, A., Dorner, M.H., & Arosio, P. (1989) *Biochemistry 28*, 5179.

Levi, S., Yewdall, S.J., Harrison, P.M., Santambrogio, P., Cozzi, A., Rovida, E., Albertini, A., & Arosio, P. (1992) *Biochem. J. 288*, 591.

Levi, S., Santambrogio, P., Cozzi, A., Rovida, E., Corsi, B., Tamborini, E., Spada, S., Albertini, A., & Arosio, P. (1994) *J Mol. Biol. 238*, 649.

Li, A.S.W, Cummings, K.B., Roethling, H.P., Buettner, G.R., & Chignell, C.F. (1988) *J. Magn. Reson. 79*, 140.

Macara, I.G., Hoy, T.G., & Harrison, P.M. (1973) *Biochem. J. 135*, 343.

Mathews, C.K. & van Holde, K.E. (1990) in *Biochemistry*, The

Benjamin/Cummings Publishing Company, Inc., Redwood City, CA.

Mayer, D.E., Rohrer, J.S., Schoeller, D.A., & Harris, D.C. (1983) *Biochemistry 22*, 876.

Mertz, J.R. & Theil, E.C. (1983) *J. Biol. Chem. 258*, 11719.

Nelson, M.J. (1988) *Biochemistry 27(12)*, 4273.

O'Connell, M.J., Baum, H.B., & Peters, T.J. (1986) *Biochem. J. 240*, 297.

Petersen, J., Dekker, J.P., Bowlby, N.R., Ghanotakis, D.F., Yocum, C.F., & Babcock, G.T. (1990) *Biochemistry 29*, 3226.

Reif, D.W. (1992) *Free Radic. Biol. Med. 12*, 417.

Rice, D.W., Ford, G.C., White, J.L., Smith, J.M.A., & Harrison, P.M. (1982) in *Advances in Inorganic Biochemistry, Volume 5* (Theil, E.C. et al., Eds.) pp 39-50, Elsevier Biomedical, New York.

Russell, S.M. & Harrison, P.M. (1978) *Biochem. J. 175*, 91.

Sahlin, M., Graslund, A., & Ehrenberg, A. (1986) *J. Magn. Res. 67*, 135.

Sahlin, M., Petersson, L., Graslund, A., Ehrenberg, A., Sjoberg, B.M., & Thelander, L. (1987) *Biochem. 26*, 5541.

Spiro, T.G. & Saltman, P. (1969) *Struct. Biol. 6*, 116.

Starke, P.E. & Farber, J.L. (1985) *J. Biol. Chem. 260*, 10099.

Styring, S.A. & Rutherford, A.W. (1988) *Biochemistry 27*, 4915.

Sun, S., Arosio, P., Levi, S., & Chasteen, N.D. (1993) *Biochemistry 32*, 9362.

Sun, S. & Chasteen, N.D. (1992) *J. Biol. Chem 267(35)*, 25160.

Tadolini, B. (1987) *Free Rad. Res. Comms. 4*, 173.

Theil, E.C., Eichhorn, G.L., & Marzilli, L.G. (1983) *Advances in Inorg. Biochem.* 1.

Theil, E.C. (1987) *Annu. Rev. Biochem. 56*, 289.

Treffry, A., Banyard, S.H., Hoare, R.J., & Harrison, P.M. (1977) in *Proteins of Iron Metabolism*, pp 3-11.

Treffry, A., Harrison, P.M., Cleton, M.I., de Bruijn, W., &

Mann, S. (1987) *J. Inorg. Biochem. 31*, 1.

Treffry, A., Hirzmann, J., Yewdall, S.J., & Harrison, P.M. (1992) *FEBS Lett. 302*, 108.

Treffry, A., Bauminger, E.R., Hechel, D., Hodson, N.W., Nowik, I., Yewdall, S.J., & Harrison, P.M. (1993) *Biochem. J. 296*, 721.

Treffry, A. & Harrison, P.M. (1978) *Biochem. J. 171*, 313.

Wade, V.J., Levi, S., Arosio, P., Treffry, A., Harrison, P.M., & Mann, S. (1991) *J. Mol. Biol. 221*, 1443.

Waldo, G.S., Ling, J., Sanders-Loehr, J., & Theil, E. (1993) *Science 259*, 796.

Waldo, G.S. & Theil, E.C. (1993) *Biochem. 32*, 13262.

Wardeska, J.G., Viglione, B., & Chasteen, N.D. (1986) *J. Biol. Chem. 261*, 6677.

Watt, G.D., Frankel, R.B., & Papaefthymiou, G.C. (1985) *Proc. Natl. Acad. Sci. USA 82*, 3640.

Watt, G.D., Frankel, R.B., Jacobs, D., Huang, H., & Papaefthymiou, G.C. (1992) *Biochemistry 31*, 5672.

Watt, R.K., Frankel, R.B., & Watt, G.D. (1992) *Biochemistry 31*, 9673.

Weir, M.P., Gibson, J.F., & Peters, T.J. (1984) *Biochem. J. 223*, 31.

Xu, B. & Chasteen, N.D. (1991) *J. Biol. Chem. 266*, 19965.

APPENDIX A

DETAILED PROCEDURES FOR SIMULTANEOUS MONITORING OF OXYGEN CONSUMPTION AND PROTON RELEASE RATE

Construction of the System

A pH electrode (Microelectrodes, Inc.) is placed in the center of the top piece of the reaction cell (Figure A.1) with a reference electrode on the left, O_2 electrode (Microelectrodes, Inc.) on the right and base delivery port at the front. All electrodes are fitted snugly into their positions to ensure that the system is gas tight. It is necessary to wrap one or two layers of Teflon type around the bottom section of the pH electrode as well as the reference electrode to ensure the fit. It may be necessary to glue the reference electrode into the reaction cell with Silicone Windshield and Glass Seal (Permatex, Loctite Corp.). The bottom of the cell, which is screwed into place and is sealed with an O-ring, contains a tiny spin bar to ensure the proper mixing of the reaction solution. The base delivery arm (PEEK tubing, 1/16" OD, 0.01" ID, Upchurch Scientific) is also screwed onto the reaction cell and sealed with an O-ring (Figure A.1).

The complete reaction cell is placed in a water bath and the water temperature is adjusted by the "TEMPERATURE CONTROL" dial on a Stir Kool (model SK 12, Thermoelectrics Unlimited,

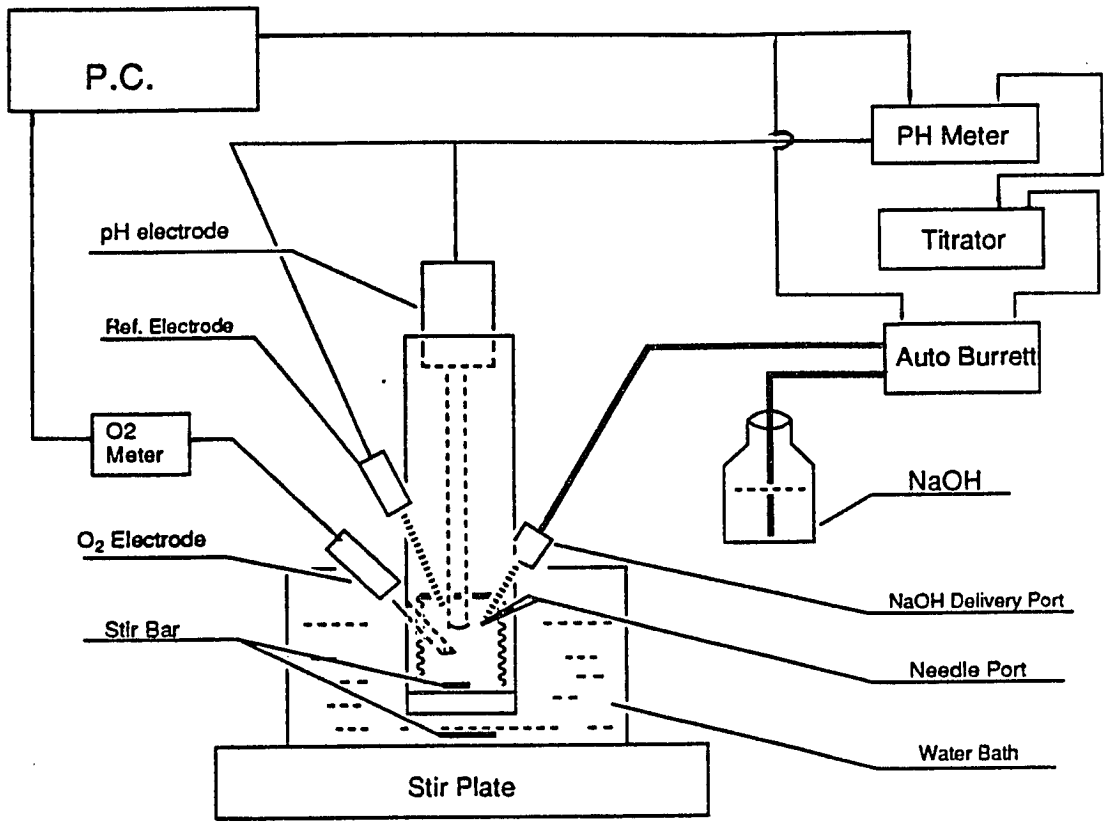

Figure A.1: Schematics of experimental setup for simultaneous monitoring of oxygen consumption and proton release kinetics.

Inc.), which controls the cooling water input.

The pH electrode is calibrated with both pH 4.00 and pH 7.00 buffer solution injected into the cell. The oxygen electrode is calibrated using ambient water (21% O_2, 0.28 mM) and 0.1 M freshly prepared sodium dithionite solution (0% O_2).

A base solution (0.0040 - 0.0100 N NaOH) is prepared daily by diluting 1 N NaOH (Fisher Scientific) in deionized distilled water (d.d.w). An accurate base solution concentration is obtained by titrating 2.00 - 5.00 ml of 0.0198 - 0.0202N HCl standard solution (Fisher Scientific) in a beaker. End point of the titration is monitored by pH electrode.

The base solution in the pH stat is supplied from the reservoir of an autoburette (ABU 80, Radiometer). The burette is filled and flushed while the "VOLUME" setting is at 1/1 position for each base concentration used. To change the base delivery volume to 0.1 μl per pulse, the burette needs to be emptied while the black switch is in the "MAN" position; then pull the "VOLUME" stick to 1/10.

Testing for leaks in the System

Before any experiments are conducted, the reaction cell should be tested for O_2 leaks to ensure the accurate measurement of the oxygen consumption rate. The detailed steps are as follows:

1. Deaerate 5 - 10 ml d.d.w with Ar gas for 1 - 2 hours

in order to expunge any dissolved oxygen.

2. Purge Ar through the empty reaction cell until the oxygen meter reads less than 5% oxygen.

3. Start the data acquisition program on the Spectra 486 equipped with an ADA board (Real Time Devices) under the directory C:\pH by typing command: O2. Enter file name, comments and reaction time.

4. Fill reaction cell with the deaerated water using a gas tight syringe while tilting the cell with base delivery port up to ensure zero head space in the cell. Screw the base delivery arm tightly in the center of the cell then place the cell in the water bath.

5. Turn on the stirrer to a setting of 60 - 70 to ensure the even distribution of the reactants. Set pH end point, speed and proportional band (See Conditions for pH Stat).

6. Start the data acquisition program and wait for 10 - 15 seconds for the base lines to stabilize. (When starting the data acquisition program, both the pH meter and the oxygen meter readings are raised slightly, ~0.02 - 0.03 units for pH reading and ~0.2 - 0.6 units in O_2 reading possibly due to voltage feed back from the computer).

7. Start the auto titrator (TTT 80, Radiometer) with ~30 μl of base delivered at a speed setting of 20 while recording the oxygen meter readings for 10 - 15 minutes then compute the oxygen level increase over time as shown in Figure A.2. In general, a 0.0016 - 0.0017% oxygen increase per second, which

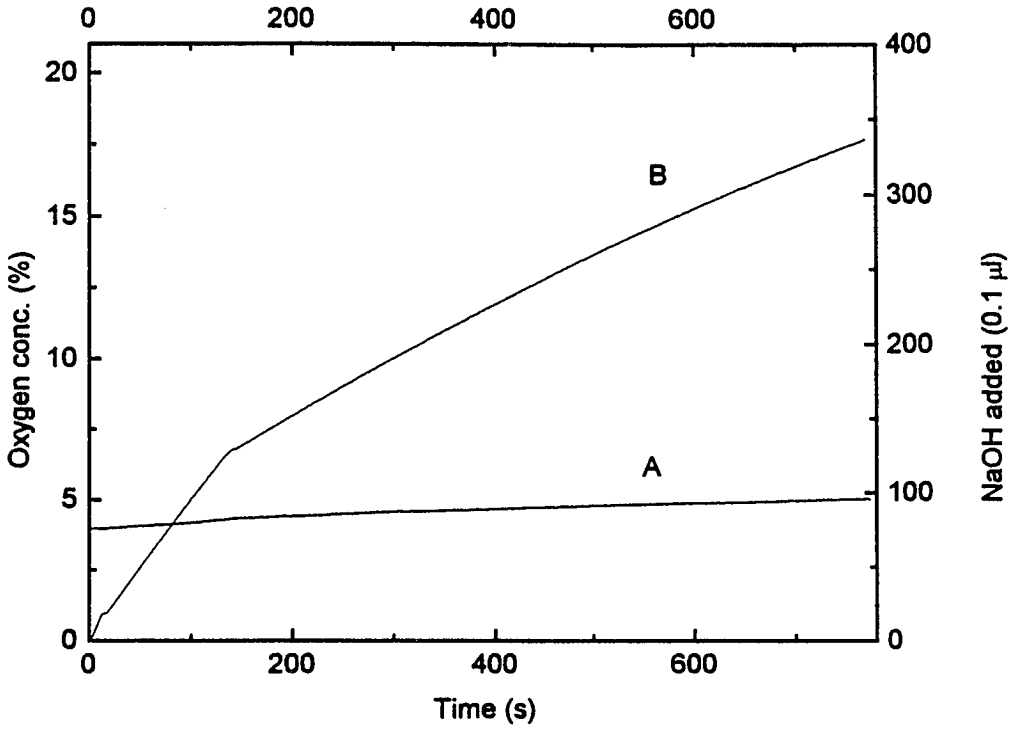

Figure A.2: Oxygen concentration increase in a deaerated water solution over time (A) while 0.1 M oxygen saturated NaOH is delivered (B). (File name: 01240694.oph)

corresponds to 0.02 - 0.03% oxygen increase in a 12 second interval, is acceptable since the oxygen meter is only accurate to the tenths place within 12 seconds at the oxygen consumption range studied. (File names: 01240394.oph, 01240494.oph, 01240594.oph, 01240694.oph, 01240794.oph)

Oxygen Electrode and pH Electrode Response Time

Oxygen electrode response time is tested by moving the oxygen electrode from an ambient water solution into a freshly prepared 0.1 N $Na_2S_2O_4$ solution and measuring the time needed for the electrode to respond when 90% of the oxygen in solution is consumed. The response time measured for the current electrode is 8.0 $\pm$ 0.4 seconds (01270194.oph, 01270294.oph, 01270394.oph).

The pH electrode response is tested by moving both pH electrode and the reference electrode from a pH = 7.00 buffer solution to a pH = 4.00 solution and measuring the time needed for the pH reading to reach 4.30 (90% response). The response times measured for the electrode in use is 2.8 $\pm$ 0.5 seconds.

Iron Oxidation and Hydrolysis Reaction Measurements

Detailed procedures for monitoring the iron oxidation and hydrolysis reaction are described below:

1. Deaerate a 20 ml solution of pH ~3.5 - 4.0 in a 25-ml Erlenmeyer flask for 1 - 2 hours while a 5-ml volumetric flask containing ferrous sulfate (Fisher Scientific) solid is purged

with Ar.

2. Transfer 480 μl of 0.15 M NaCl and 0.5 mM MOPS buffer (unless another buffer is required) sample solution with a 500 μl Hamilton syringe to the reaction cell as described in the oxygen leak test section.

3. Prepare a ferrous stock solution by transferring 5 ml deaerated water (adjusted to pH 3.5) using a 2.5-ml gas tight syringe to the Ar purged 5-ml volumetric flask containing solid ferrous sulfate.

4. Adjust the pH of the sample solution in the reaction cell using the auto titrator to the end point while the ferrous sulfate solid is dissolving in the volumetric flask. If the pH of the sample is too far from the end point setting, more concentrated acid or base may be used to adjust the pH to ~0.2 units below the end point. The auto titrator should be used to adjust the final pH of the solution to the end point in order to minimize the diffusion of sample solution to the base delivery arm resulting in inaccuracy of the base concentration delivered.

5. Start the data acquisition program, readjust the pH end point to 0.01 unit below the end point, then start the auto titrator.

6. Inject appropriate amount of iron solution into the reaction cell to initiate the iron oxidation reaction.

7. Print screen after the data acquisition is completed.

8. Immediately disassemble the two piece reaction cell,

clean and dry the cell with d.d.w. and Kimwipes.

9. Empty the burette each time after an experiment is completed to ensure the accuracy of the base concentration in the delivery arm. pH readings need to be checked against a pH 7.00 buffer after several runs.

Initial Rate Determination

Both the oxygen consumption and proton release rates are determined using a 3rd order polynomial fit to the data obtained when the reaction is 87 - 95 % complete (Waldo & Theil, 1993). The oxygen consumption or proton release is expressed as: $Y = A_0 + A_1t + A_2t^2 + A_3t^3$, $dY/dt = A_1 + 2A_2t + 3A_3t^2$, where Y is the amount of oxygen consumed or protons released, t is the reaction time and dY/dt is the reaction rate at any given time. At t = 0, the reaction rate is the initial rate which can be represented by $(dY/dt)_{t=0} = A_1$.

Examples of calculating the initial iron oxidation rate with the use of nitrilotriacetate (NTA, Aldrich) as a chelator using 100% and 87% reaction completion data are shown in Figures A.3 and A.4, respectively. The iron oxidation reaction is expressed as:

$$Fe(II)\text{-}NTA + O_2 \xrightarrow{k} Fe(III)\text{-}NTA + O_2^- \qquad (1)$$

where k is the reaction rate constant. Oxygen consumption rate V_{O2} can be represented as:

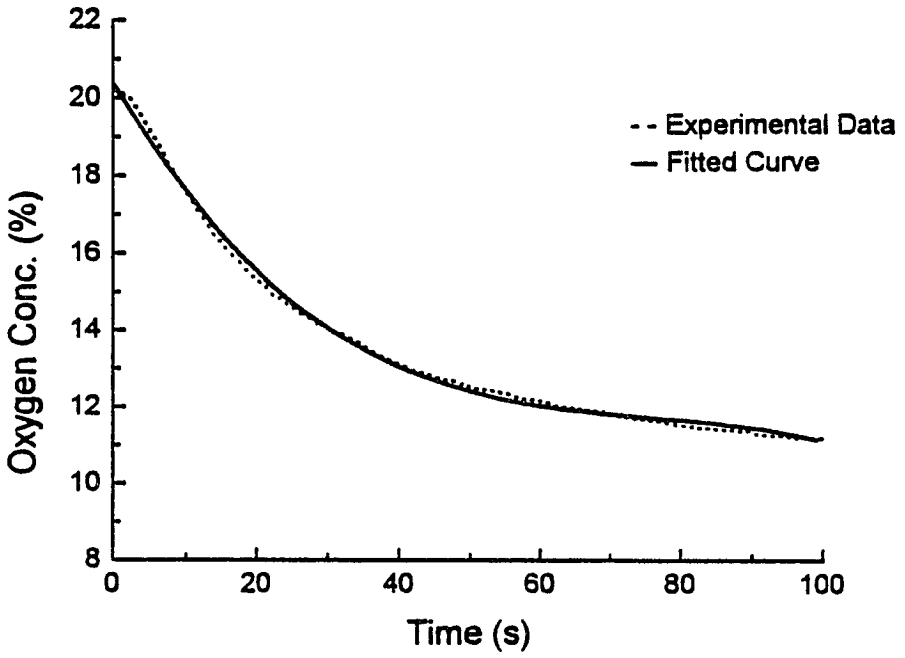

Rate Constant, $K = A_1/[O_2][Fe^{2+}] = 51\ M^{-1}S^{-1}$

Polynomial Regression
y = A0 + A1 x + A2 x^2 + A3 x^3 +...

Parameter	Value	sd
A0	20.272150	0.01218
A1	-0.31372849	0.00144
A2	0.0040919855	0.00004
A3	-1.8958081E-5	2.8406E-7

R =0.99942
R^2=0.99884
SD =0.11424

Figure A.3: Third order polynumeric fit for oxygen consumption rate using 87% reaction completion (reaction three half lives). Conditions: 4 mM NTA in 0.15 N NaCl and 50 mM MES, pH 6.38, 20 °C. $[Fe^{2+}]$ = 0.3 mM. (File name: 01240994.oph)

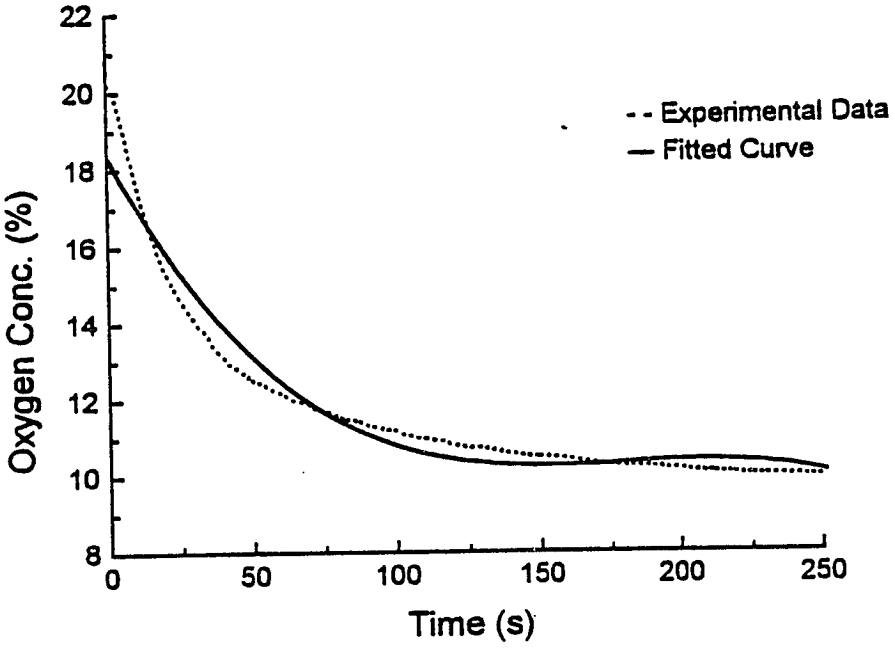

Rate Constant, $K = A_1/[O_2][Fe^{2+}] = 22\ M^{-1}S^{-1}$

Polynomial Regression
y = A0 + A1 x + A2 x^2 + A3 x^3 +...

Parameter	Value	sd
A0	18.331619	0.05902
A1	-0.14080270	0.00183
A2	8.0275961E-4	0.00002
A3	-1.4863232E-6	3.5746E-8

R =0.97734
R^2=0.9552
SD =0.45247

Figure A.4: Third order polynumeric fit for oxygen consumption rate using 100% reaction completion. Conditions are the same as Figure A.3. (File name: 01240994.oph)

$$V_{O2} = -d[O_2]/dt = k\ [Fe(II)\text{-}NTA]_0\ [O_2]_0$$

$[Fe(II)\text{-}NTA]_0$ and $[O_2]_0$ are the initial Fe^{2+} and oxygen concentrations in solution, respectively. When using 87% (3 halves) of reaction completion, a k value of 51 $M^{-1}s^{-1}$ (Figure A.3) is calculated from the A_1 term obtained by curve fitting, which is in a better agreement with the literature data of 80 $M^{-1}s^{-1}$ (Kurimura et al., 1968) comparing to the k value of 22 $M^{-1}s^{-1}$ obtained using 100% reaction completion (Figure A.4).

As a test for measuring proton release rate, hydrolysis of t-butyl chloride (Aldrich) in 0.1 M Na_2SO_4 (Aldrich) was monitored at pH 7.0, 20 °C. The reaction is:

$$\text{t-butyl-Cl} + H_2O \xrightarrow{k} \text{t-butyl-OH} + HCl \qquad (2)$$

where k is the reaction rate constant, which may be determined from the reaction rate $V_{H+} = d[HCl]/dt = -k[\text{butyl-Cl}]$ (when time (t) = 0, reaction rate V_{H+} = initial rate V_0, $[\text{butyl-Cl}] = [\text{butyl-Cl}]_0$ and V_0 can be determined from the initial rate of NaOH addition which is obtained from the A_1 term of the 3rd order polynomial fit of NaOH added over time (Figure A.5A)). The k value can also be determined from the slope of the first order reaction rate plot $\ln([\text{butyl-Cl}]_0-[HCl])$ *vs.* t, where $[\text{butyl-Cl}]_0 = [HCl]_\infty$ (Figure A.5B). However, an initial pH drop resulting from a faster base delivery rate than the

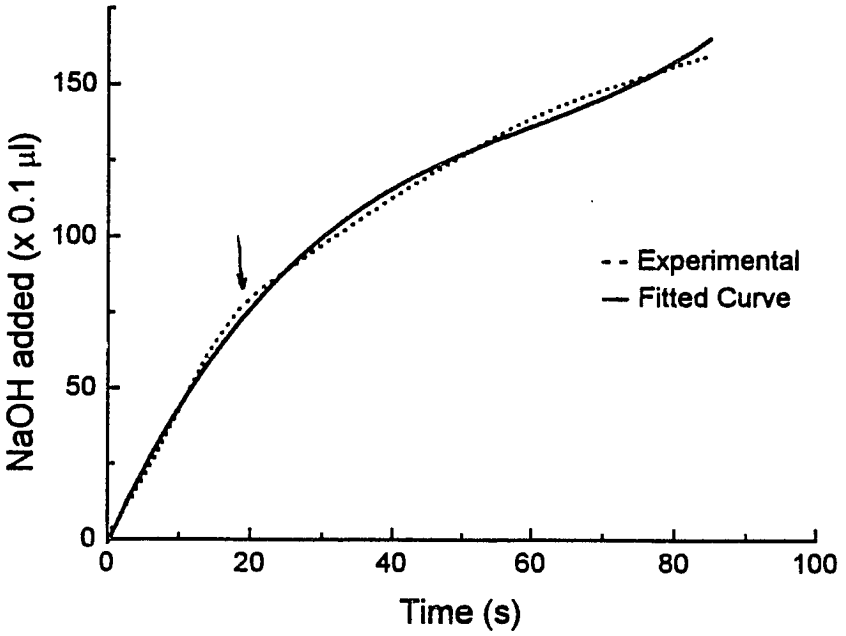

Rate Constant, $K = A_1[NaOH]/([t\text{-Butyl-Cl}]*\text{Total Vol.}) = 0.0311\ S^{-1}$

Polynomial Regression
$y = A0 + A1\ x + A2\ x^2 + A3\ x^3 + \ldots$

Parameter	Value	sd
A0	-1.2261699	0.56887
A1	5.1393618	0.07013
A2	-0.071730131	0.00211
A3	4.0184114E-4	0.00002

R =0.99864
R^2=0.99728
SD =2.42535

Figure A.5a: Hydrolysis reaction over time with base delivered over shooting at the beginning (Reaction 87% completion). Conditions: $[Na_2SO_4]$ = 0.1 M, [t-Butyl-Chloride] = 1.4 $x10^{-4}$ M in acetone, [NaOH] = 4.237 mM, pH 7, 23 °C. pH stat settings: Speed 30, PB 0.2, DELAY SEC: pH STAT, VOLUME 1/10. (File name: 02170494.dig)

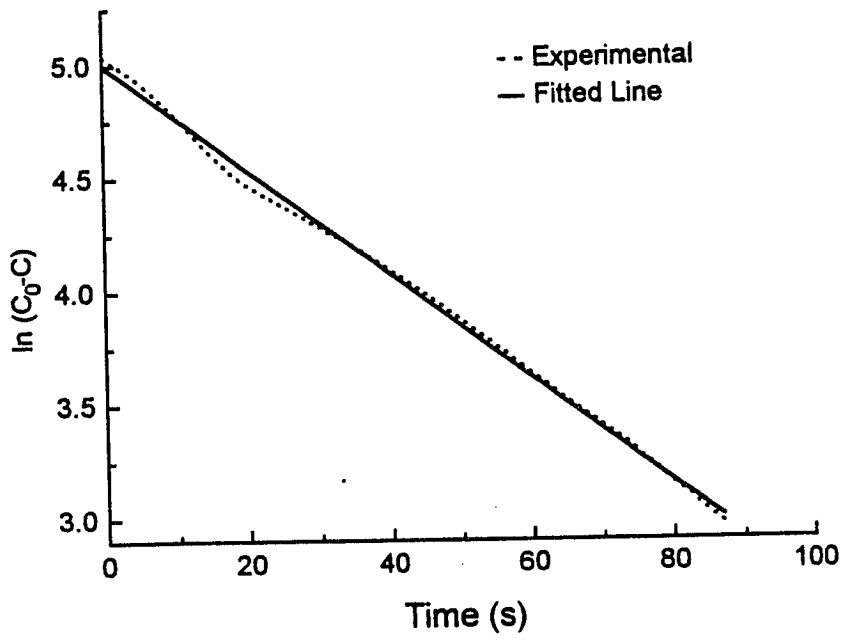

Rate Constant, K = B = 0.023 S^{-1}

```
Linear Regression
Y = A + B * X
Param       Value       sd
A           5.16546     0.00421
B           -0.02299    0.00011
R  = -0.99807
SD = 0.03352, N = 159
P = 2.4119E-191
```

Figure A.5b: The log of $[H^+]$ *versus* time. Conditions are the same as given in Figure A.5a. (File name: 02170494.dig)

actual reaction, or the slow delivery of base due to the lag of the electrode response time at the beginning portion of the reaction, as indicated by the arrow in Figure A.5A, are not avoidable. This will introduce error in the initial rate obtained by curve fitting if all of the data points are used. An example is shown in Figure A.5A where the reaction rate constant, $k = V_0/[\text{t-butyl-Cl}]_0 = 0.0311\ s^{-1}$, is 30% higher than obtained from the slope of the $\ln([NaOH]_\infty - [NaOH])$ *vs.* t plot (Figure A.5B, k = slope = $0.0230\ s^{-1}$). To minimize this artificial error, a curve fit using only the later portion of the reaction then extrapolation to the t = 0 point has been found more adequate (Figure A.6A). The rate constant k of $0.0232\ s^{-1}$ obtained using log fit (Figure A.6B) is only 12% different from the k value of $0.0262\ s^{-1}$ calculated from the A_1 term (Figure A.6A). Both k values are in agreement with the published k value of $0.020 - 0.037\ s^{-1}$ (Adams et al., 1994). A polynomial function with A_0 term forced to zero has also been applied to fit curve 6A and 2 - 4% difference in A_1 value is obtained comparing to that obtained when $A_0 \neq 0$.

Conditions for pH Stat

For every new system, a set of experiments is needed to obtain the optimal selections of instrument parameters.

Choosing Proportional Band

Base delivery speed is regulated by how far the pH of sample solution deviates from the end point within the

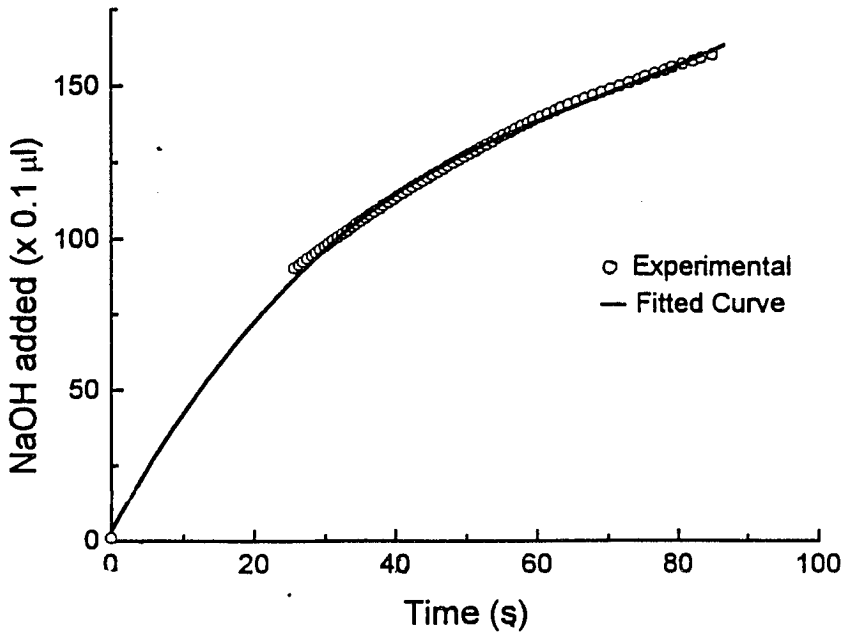

Rate Constant, $K = A_1[NaOH]/([t\text{-}Butyl\text{-}Cl]*Total\ Vol.) = 0.0262\ S^{-1}$

Polynomial Regression
y = A0 + A1 x + A2 x^2 + A3 x^3 +...

Parameter	Value	sd
A0	1.4720005	0.58737
A1	4.3329026	0.04473
A2	-0.047238297	0.00118
A3	2.1429805E-4	9.0652E-6

R =0.99959
R^2=0.99919
SD =0.83041

Figure A.6a: Hydrolysis reaction over time after delete the base over shooting portion of data (A). Conditions are same as Figure A.5a. (File name: 02170494.dig)

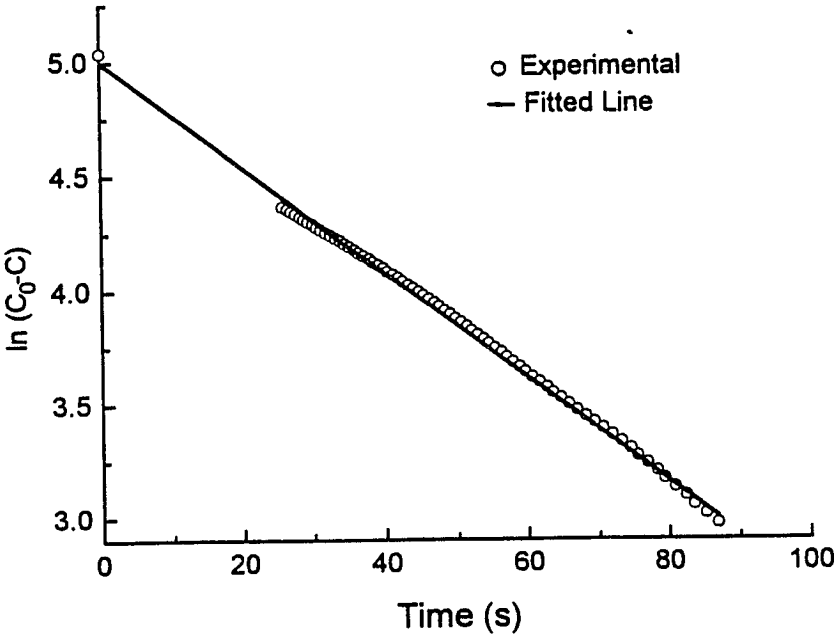

Rate Constant, K = B = 0.0232 S^{-1}

```
Linear Regression
Y = A + B * X
Param       Value       sd
A           5.18432     0.0054
B           -0.02315    0.0001
R  = -0.99942
SD = 0.01447, N = 66
P = 1.3896E-95
```

Figure A.6b: The log of [H^+] *versus* time. Conditions are same as given in Figure A.5a. (File name: 02170494.dig)

proportional band (TITR. light blinking). The farther the pH reading is away from set end point, the faster the base will be delivered until the sample pH is the same as the end point, at which time the proton production rate of the reaction will be the same as the base delivering speed. The proportional band (PB), therefore, needs to be set as narrow as possible because too wide a band will artificially decrease the base delivery rate so much that the pH meter reading will be below the end point throughout the whole reaction time. As a result, the base delivery rate will be slower than the actual reaction rate (Figure A.7, PB = 2). If the proportional band is too narrow, the initial reaction may be too fast for the pH electrode response, causing the pH value to drop below the PB range (TITR. light steady) thus resulting in a base delivered speed that follows the constant speed set by the speed dial (Figure A.8, PB = 0.2). Normally a PB setting of 0.1 is suitable for many iron oxidation reactions, however, t-butyl-chloride hydrolysis is too fast to be monitored at a PB of 0.1, hence a PB of 0.5 should be used (Figure A.9).

Choose Base Delivering Speed

The speed of the delivery of the base should be chosen at a relatively fast setting to ensure that delivery speed does not constrain the reaction rate recorded. If the speed chosen is too slow, the reaction rate recorded will be slower than the actual rate, while the pH remains below the end point

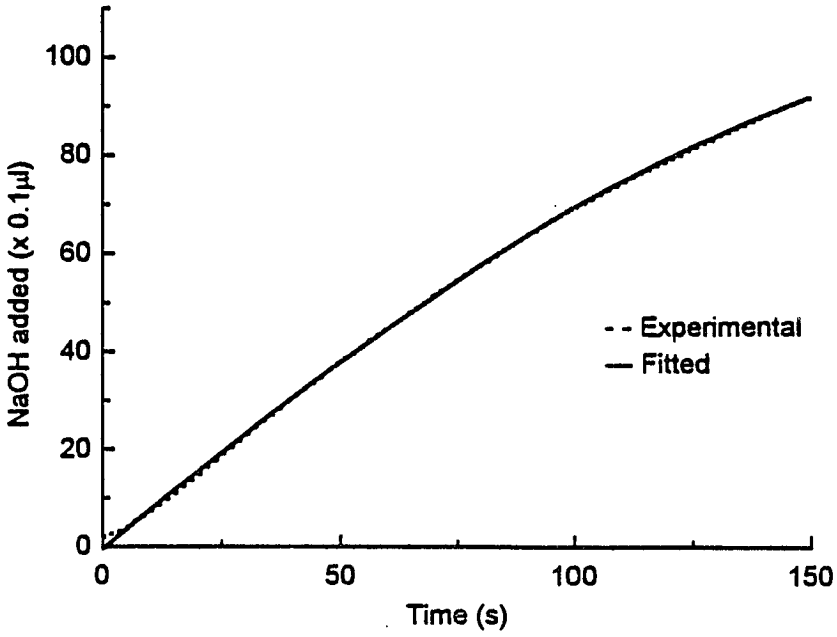

Rate Constant, K = 0.0138 S^{-1}

Polynomial Regression
y = A0 + A1 x + A2 x^2 + A3 x^3 +...

Parameter	Value	sd
A0	-0.50809988	0.17266
A1	0.81608405	0.00929
A2	-7.2554061E-4	0.00013
A3	-3.8914919E-6	5.5357E-7

R =0.99988
R^2=0.99977
SD =0.43221

Figure A.7: Hydrolysis reaction of t-butyl-chloride in water. Conditions are same as Figure A.5a except [t-butyl-chloride] = 5 x10^{-5} M, speed is set at 80, PB at 2. (File name: 02210594.dig)

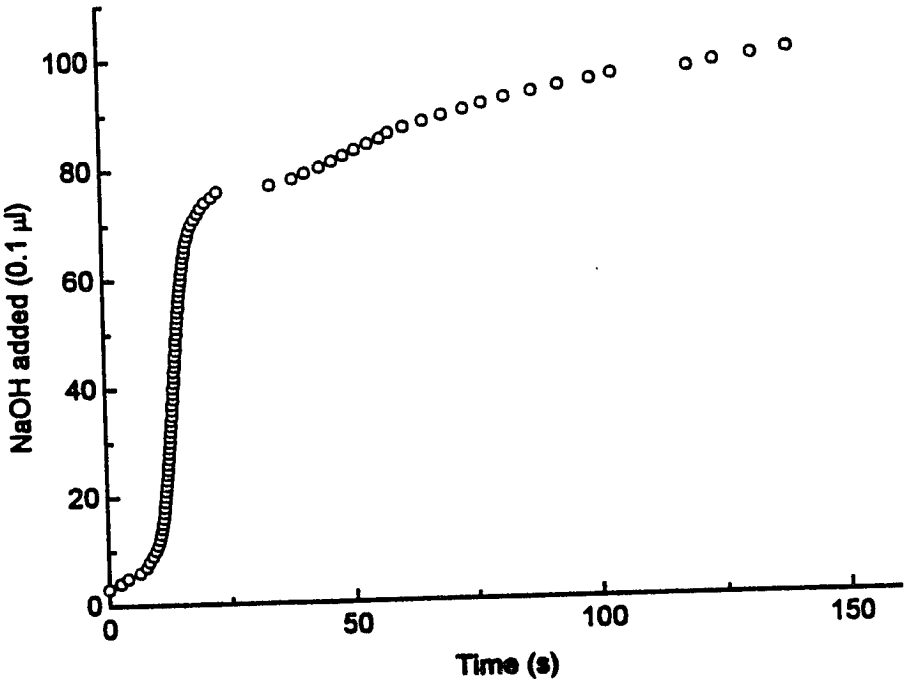

Figure A.8: Hydrolysis reaction of t-butyl-chloride in water. Conditions are the same as Figure A.7 except the PB is set at 0.2. (File name: 02210794.dig)

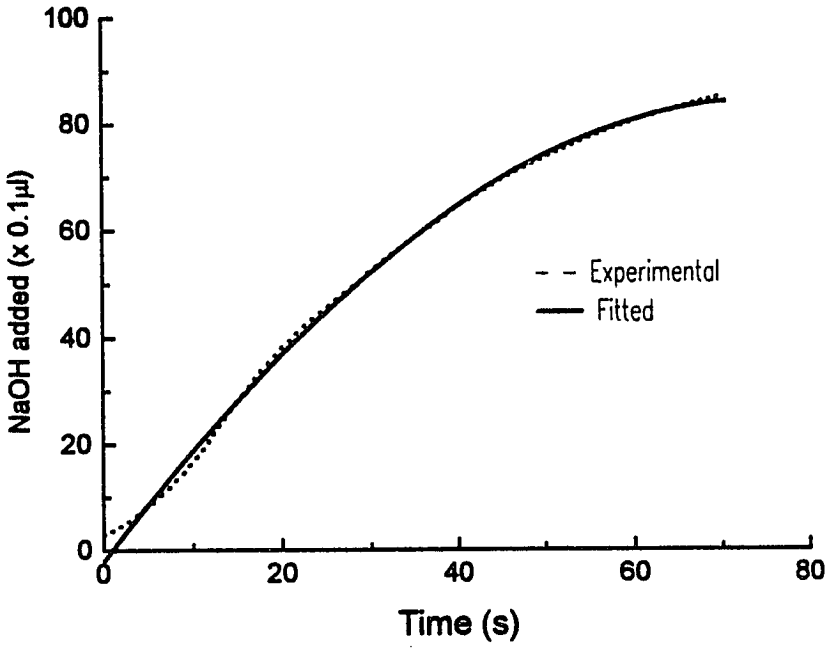

Rate Constant, K = 0.037 S^{-1}

Polynomial Regression on A02170694.DIG_A
y = A0 + A1 x + A2 x^2 + A3 x^3 +...

Parameter	Value	sd
A0	-1.9296021	0.50943
A1	2.1848125	0.06539
A2	-0.011878782	0.0023
A3	-2.7894187E-5	0.00002

R =0.99887
R^2=0.99774
SD =1.15393

Figure A.9: Hydrolysis reaction of t-butyl-chloride in water. Conditions are the same as Figure A.7 except the PB is set at 0.5. (File name: 02170694.dig)

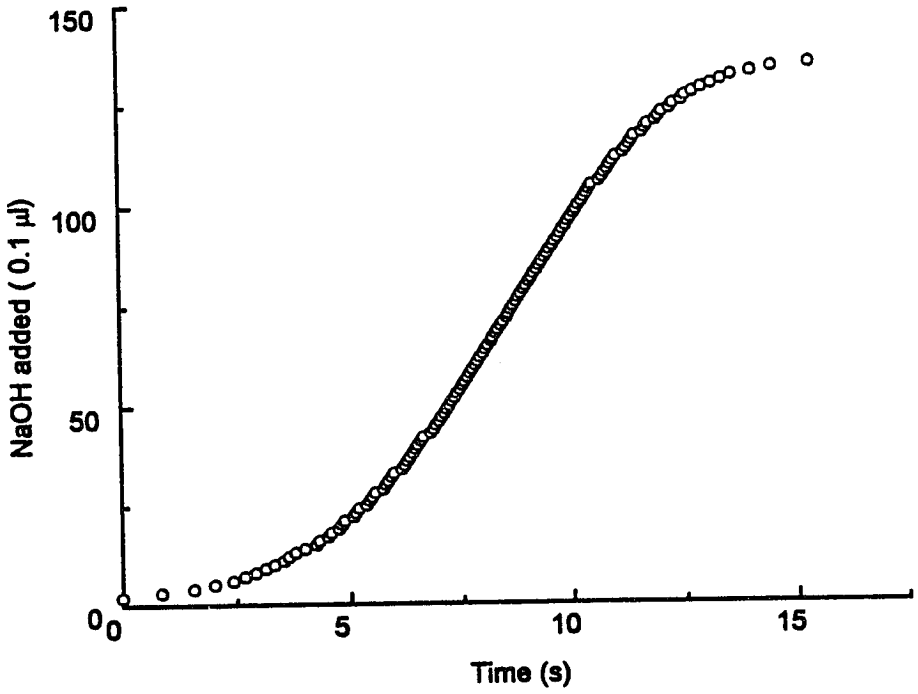

Figure A.10: Hydrolysis reaction of t-butyl-chloride in water. Conditions are the same as Figure A.5 except the speed is set at 40. (File name: 02211394.dig)

(Figure A.10, Speed = 40). In most cases, a setting of 40 - 60 will be efficient for the iron oxidation reaction. If the speed is too fast, a slight pH exceeding the proportional band setting will cause a large amount of base delivered in too short a period of time for the pH electrode to response (Figure A.11, speed 120). The resulting over delivery of base will not only stop titration periodically due to the pH readings exceeding the end point, but it may also alter the reaction pH to affect the actual reaction rate.

Choose Base and Reactant Concentrations

Base concentration is chosen based upon the reaction speed and the amount of proton released during the reaction. The base concentration should be as concentrated as possible to reduce the amount of base delivered therefore reducing the dilution of the sample. However, there should be enough digital pulses (proton produced) to compensate for the inaccurate base delivery rate caused by the initial drop in pH drop to the lag in the response of the pH electrode. In general, a pulse number of 50 or above (5 μl for VOLUME at a 1/10 setting) is recommended. On the other hand, if the base used is too concentrated, one pulse (0.1 μl base) will cause too large a pH increase resulting in the sample pH exceeding the end point causing the inconsistent measurement of the actual reaction.

If the reaction itself is too fast for the auto titrator

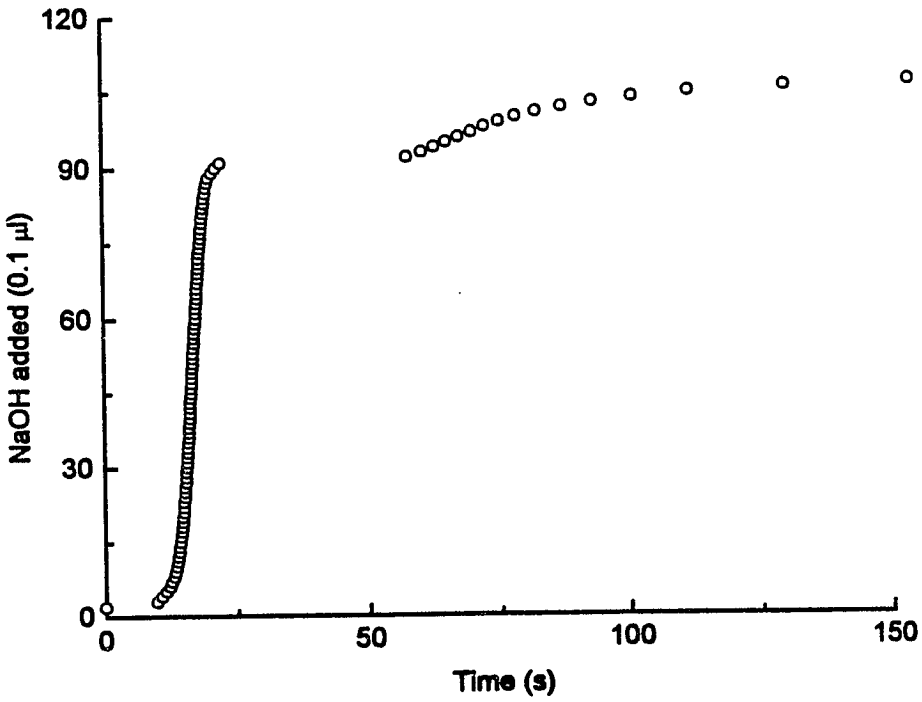

Figure A.11: Hydrolysis reaction of t-butyl-chloride in water. Conditions are the same as Figure A.7 except the speed set at is 120. (File name: 02170794.dig)

to follow, reactant concentrations such as the Fe(II) concentration or enzyme concentration (ferritin concentration in this case) should be reduced to fit the instrumental conditions. For the iron oxidation reaction catalyzed by horse spleen ferritin, 5 μM or less apoferritin is required for an accurate hydrolysis rate measurement. Fe(II) concentration of 270 μM is generally the upper limit since the oxygen concentration dissolved in 20 °C water solution is 280 μM.

Comparison of pH Stat and Buffer Effect to Iron Oxidation

To verify that the iron oxidation reaction carried out under pH stat conditions is the same with that using buffer to control pH, a set of experiments monitoring the Fe(II)-NTA oxidation reaction rate was conducted. The results are listed in Table A.1. The reaction constant k is calculated as: $k = (-d[O_2]/dt)/([Fe^{2+}]_0[O_2]_0)$, where $d[O_2]/dt$ is obtained from the A_1 term of the 3rd order polynomial fit to the curve of oxygen consumption over time.

Table A.1: Iron oxidation under different pH control

Conditions: [NTA] = 4 mM, [NaCl] = 0.15 M, pH 7.04, 20 °C.

File name	Method	[MOPS] (mM)	$[Fe^{2+}]_0$ (mM)	Rate constant k (M^{-1} S^{-1})
12090593.O2	pH STAT	0.5	0.6	41
12090493.O2	pH STAT	0.5	0.4	47
12090393.O2	pH STAT	0.5	0.4	49
Average	pH STAT			46 $\pm$ 4
12150293.op	Buffer	50	0.6	56
12150393.op	Buffer	50	0.4	47
12150193.op	Buffer	50	0.2	46
Average	Buffer			50 $\pm$ 6

Difference in rate constant, k = 8%

APPENDIX B

PROCEDURES FOR APOFERRITIN PREPARATION (Bauminger et al., 1991)

Preparing apoferritin

All steps are performed at room temperature, all chemicals are reagent grade or higher unless otherwise stated. Since the autoxidation of sodium hydrosulfite (dithionite) (J.T. Baker, technical grade) is reported to give colloidal sulfur at low pH (pH < 4.6) (Crichton, 1973), all relevant dialysis steps are kept anaerobic and at pH > 5.0.

Step 1. Ferritin (3x crystallized, cadmium free, Boehringer Mannheim) is transferred into a dialysis tube with molecular weight cutoff of 6000 - 8000 (Spectrum) using a B-D® syringe (Becton Dickinson).

Step 2. The dialysis apparatus is shown in Figure B.1. A 0.1 M sodium acetate (Aldrich) buffer solution (pH 5.0 - 5.2) is deaerated in an Amicon 5L reservoir by purging nitrogen gas for one hour. A 3 g/100 ml sodium dithionite solution is then added to the deaerated buffer. One liter of the above dithionite solution is transferred anaerobically into a nitrogen gas purged dialysis bottle (Nalgene®), containing the ferritin dialysis bag. The dialysis solution is changed twice a day and a total of 5 changes are performed at this dithionite concentration. In the case of human or

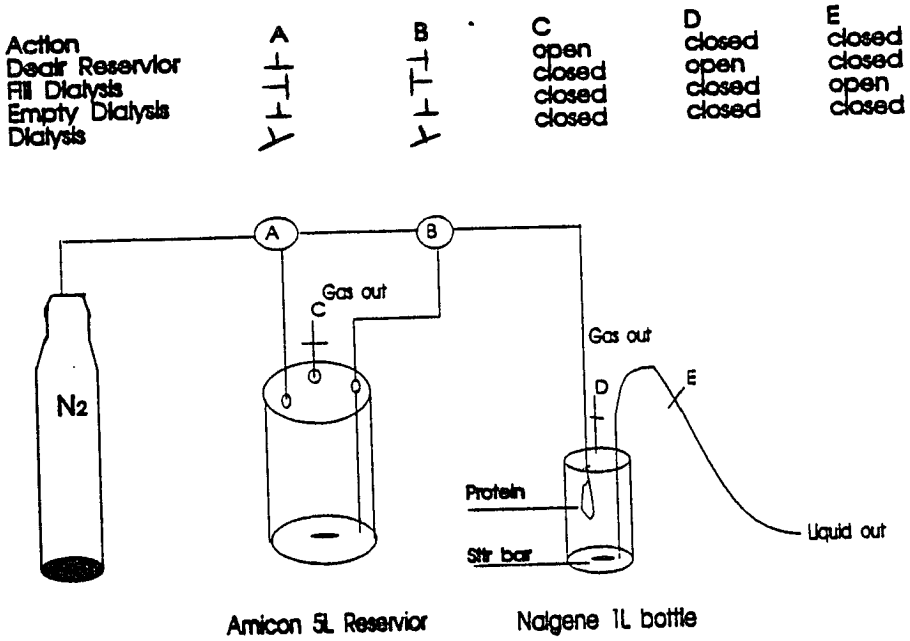

Figure B.1: Experimental setup for apoferritin preparation

mutant ferritin, 0.1 M MES of pH = 6.2 (Research Organics) buffer is used instead of acetate buffer to avoid the denaturation of human ferritin at lower pH.

Step 3. Step 2 is repeated except the dithionite concentration used is 0.3 g/100 ml dithionite. Five dialysis changes are made at this concentration. At the end of the fifth dialysis, a small quantity of dialysate is tested for iron content using 2,2-dipyridyl (Sigma Chemical) or 1,10-phenanthroline (Eastman Kodak Co.). If a pink (for dipyridyl) or orange color (for phenanthroline) is observed, step 3 is repeated.

Step 4. Deaerate a solution of 0.1 M sodium acetate and 1 mM 2,2-dipyridyl (to chelate residual iron and wash out dithionite) as described in step 2. Three to five changes are made with this solution.

Step 5. The apoferritin dialysis bag is then removed from the dialysis bottle and placed into a clear 1 L Nalgene bottle containing 0.15 M NaCl (Aldrich), pH ~7.5 at 4 °C, in order to wash out the dipyridyl and buffer. In general, 6 changes are recommended for this step.

Step 6. The apoferritin concentration is measured using $\epsilon 280$ = 19,500 $subunit^{-1}$ cm^{-1} for horse spleen ferritin and BioRad assay for other proteins. All protein solutions are stored in plastic bottles at 4 °C.

Step 7. The amount of residue iron in apoferritin is analyzed following the published procedures (Percival, 1991).

a. A 100 - 200 μl volume of apoferritin solution (~0.8 mM subunit) is added to 1 ml solution containing 250 μl 30% trichloracetic acid (Aldrich) and deionized distill water.

b. Centrifuge (microcentrifuge, Fisher Scientific) the above mixture for 1 minute. Transfer 650 - 750 μl of the supernatant to a clean tube, in which 100 μl ammonium acetate (Aldrich), 62.5 μl of 0.12 M ascorbic acid (Sigma Chemical), 62.5 μl 0.25 M Ferrozine (Aldrich) and water are added to make a final solution volume of 1 ml.

c. The iron content is then determined based on the absorbance at 562 nm with $\epsilon_{Fe\text{-}ferrozine}$ = 27,900 M^{-1} cm^{-1}.

The whole apoferritin preparation procedure takes less than 2 weeks. The iron content in apoferritin is normally less than 0.5 Fe/24-mer.

Comparison of the rate of iron oxidation reaction catalyzed by apoferritin prepared using dithionite and thioglycolic acid (TGA) method (Chasteen & Theil, 1982)

The 2-port acrylic reaction cell holding a micro oxygen electrode (Microelectrode, Inc.) interfaced with a PC (Spectra 486) is used for this experiment. The horse spleen apoferritin concentration is 8.3 μM (24-mer) with 0.15 M NaCl and 50 mM MOPS (Research Organics) buffer at pH 7.0 and 20 °C. The 0.26 mM Fe(II) solution (pH < 2) is added to initiate the reaction (Fe(II)/protein = 31). The recombinant human ferritin (rHF) concentration is 1.96 μM (24mer) with 0.15 M

NaCl and 50 mM MOPS, pH 7.0, 20 °C. A 67 μM Fe(II) solution is used to repeatedly initiate the iron oxidation reactions with the same ferritin solutions (Fe(II)/protein = 34). Iron oxidation rate is measured as the average oxygen consumption during the initial 12 seconds of the reaction using the software package, Origin (MicroCal Scientific, Inc.). The results are shown in Tables B.1 & B.2.

Table B.1 Results of iron uptake catalyzed by horse spleen ferritin prepared by dithionite and TGA method.

File Name (*.oph)	protein prep method	O_2 consumtion rate (μM/s)
02150294	TGA	2.528
02150394	TGA	2.555
02160194	TGA	2.461
02160294	TGA	2.758
Average rate:	TGA	2.575 $\pm$ 0.128
02150594	Dithionite	3.772
02150694	Dithionite	3.299
02150794	Dithionite	3.718
Average rate:	Dithionite	3.596 $\pm$ 0.258

$$\text{Average rate difference} = \frac{2.575 - 3.596}{3.086} = -33\%$$

Table B.2. Results of iron oxidation rates catalyzed by recombinant human H chain ferritin prepared by dithionite and TGA methods.

File Name (*.oph)	Fe(II) additions	Protein prep. (rHF)	O_2 consumption rate (μM/s)
03110894	1st	TGA	1.671
03110894	2nd	TGA	1.203
03110994	3rd	TGA	1.333
03110994	4th	TGA	1.112
03110994	5th	TGA	1.102
03111094	1st	Dithionite	2.059
03111094	2nd	Dithionite	1.444
03111094	3rd	Dithionite	1.279
03111094	4th	Dithionite	1.298
03111194	5th	Dithionite	1.282

The rate difference between dithionite preparation and TGA preparation after 1st iron addition:

$$\text{The rate difference} = \frac{1.671 - 2.059}{1.865} = -21\%$$

The average oxygen uptake rate from 2nd to 5th iron addition:

TGA prep. $= 1.188 \pm 0.107$

Dithionite Prep. $= 1.325 \pm 0.079$

$$\text{The rate difference} = \frac{1.188 - 1.325}{1.256} = -11\%$$

APPENDIX C

PROCEDURES FOR ISOLATION OF SHEEP SPLEEN FERRITIN (Mertz & Theil, 1983)

Testing Iron Content in Spleen

Before any isolation steps are performed, the total iron content in each sheep spleen is tested. Ferritin is isolated from high iron content spleen as follows:

1. Slice 0.1 g of spleen tissue (Mapelli Brothers Food Distribution Co.) from each spleen and boil in 5 ml 1 N HCl for 1 hour. After cooling for 20 minutes, the mixture was centrifuged using IEC B20A at 18,000xg.

2. Add excess hydroxylamine (~1 ml, 0.5 M) (J.T.Baker) to above supernatant to reduce Fe(III) to Fe(II).

3. Add 0.8 ml solution from step 2 to 1 ml 0.01 M Ferrozine (Aldrich) solution. Adjust to pH ~5.0 with 4 M NaOH, adjust total volume to 2.0 ml with d.d.w. Measure iron concentration of the solution by absorbance at 562 nm (Cary 219) against standard curve.

4. Pick the highest iron content spleen to perform isolation procedures since the amount of ferritin in spleen is regulated by the amount of iron present.

Isolation of Ferritin

All isolation steps should be performed at 4 °C unless

otherwise stated. All chemicals are reagent grade.

1. Weigh frozen spleen tissues, record age and sex of animal and the date the spleen was obtained.

2. Homogenize spleen tissue with 1.5 x volume/weight distilled water added using 14-speed Blender (Hamilton Beach) at highest speed.

3. Heat the homogenate at 70 °C for 10 minutes to denature proteins in the spleen other than ferritin. Place the mixture on ice for 10 minutes then centrifuge at 18,670 x g for 20 minutes (or 16,000 x g for 30 minutes) (IEC B20A). Collect the clear red-brown supernatant.

4. Add β-mercaptoethanol (Sigma) to a final concentration of 1 mM to the supernatant collected in step 3.

5. Precipitate protein from the supernatant with 313 mg/ml $(NH4)_2SO_4$ (J.T.Baker). The resulting suspension should be kept at 0 °C (on ice) over night.

6. Centrifuge the mixture from step 5 at 47,000 x g (Beckman L2-65B with SW 27.1 roter, polyallomer centrifuge tube, 16x102 mm, Seton Scientific) for 30 minutes, collect the pellet and dissolve in a 20 mM Na_2HPO_4 solution (Fisher), pH 6.8, with stir bar stirring for 1 hour.

7. Centrifuge the solution obtained from step 6 at 100,000xg for 2.5 hours (Beckman L2-65B), collect the pellet, dissolve and dialyze against a 20 mM Na_2HPO_4 with 1 mM β-mercaptoethanol at pH 6.8.

8. Run the dialyzed solution through a Sepharose 6B

(Sigma) column using a fraction collector with UV detector (wavelength 280 nm) (ISCO UA-5). Collect the fluid with absorbance at 280 nm. (Ferritin also has a distinctive yellow color).

9. Run 5% non-denatured PAGE and 15-17% SDS PAGE to verify purity and molecular weight of the isolated ferritin.

10. Final yield is ~1 mg ferritin per gram spleen used.

APPENDIX D

INTERFACING pH-STAT AND OXYGEN ELECTRODE TO A PC

Pin out for ADA 2000 to pH stat and O_2 electrode

P8 (Analog Input)	P14 (Digital Input)	DB25 Connector	Barrier strip	O_2 meter	pH stat
Pin 1		13	O_2 in + (red)	red	
Pin 3		11	O_2 in - (black)	white	
Pin 5		9	pH in + (blue)		black
Pin 7		7	pH in - (yellow)		white
	Pin 1	14	digital ground (white)		red
	Pin 19	15	Pulse input + (green)		green

A differential analog input of 0 - 10 V is used to reduce noise pickup. When using only one of the analog inputs, short the other at the barrier strip to prevent erroneous readings.

Program O2.EXE will collet pulses continually and without limit, storing them in the file "*.dig" in the form:
Pulses count (space) elapsed time (in seconds)

The analog data are collected by dividing the length of the run into 1000 equal parts and taking one sample for each

time period. This is then stored in the file "*.oph" in the form:

O_2 value (in %) (space) pH value (space) elapsed time (in sec)

Source code for data acquisition program

```
/*************************************************************************
*    o2.c   program to acquire and display O2 concentration, PH, and
*    number of titration pulses from "Radiometer" PHM 82 ph meter,
*    TTT80 titrator, and ABU80 autoburette system. using the Analog
*    Devices ADA2000 a/d card (12 bit) compiled with Borland C ver 3.1
*    Copyright 1993,  Robert W. Curry
*                     Durham, NH  03824-2604
*************************************************************************/

#include <graphics.h>
#include <stdio.h>
#include <stdlib.h>
#include <conio.h>
#include <string.h>
#include "tctimer.h"
#include "adc.h"
#include "mux.h"
#include "gain.h"
#include "init.h"
#include "dda.h"


int main()
{
        unsigned int x;
        int board, channel1, channel2, range, z;
        int     gdriver = DETECT, gmode, errorcode;
        int newa, newb, newx, newy, pulse, index, bindex;
        int tot, lastpulse, olda, oldb, oldx, oldy, junk, displa;
        int minrun, thisrun, tmpresult3, tmptmpresult;
        double *time_ptr;
        float start, thistime, elapsed, lasttime, looptime, dindex;
        float tmpresult1, tmpresult2, result2, result1;
        char btime[20], totstr[10], decstr[5], thisstr[10], pstr[10];
        char name[9], name1[13], name2[13], comment[80];
        FILE *fp1;
        FILE *fp2;
        board = 0x340;
        channel1 = range = 1;
        channel2 = 2;
        tmpresult1 = tmpresult2 = 0.0;
        olda = oldx = 1;
        oldb = 478;
        oldy = 128;
        pulse = tot = index = dindex = 0;
        displa = bindex = 1;
        time_ptr=(double *)malloc(sizeof(double));
        clrscr();

        printf("Input name for files. \n");
        gets(name);
        strcpy(name1, name);
        strcpy(name2, name);
        strcat(name1, ".oph");
        strcat(name2, ".dig");

        if ((fp1 = fopen(name1, "r+"))  != NULL){   /* check for duplicate filen
           fclose(fp1);
           fprintf(stderr, "\nFile currently exists by that name.\n");
           fprintf(stderr, "Press any key to start over.\n");
```

```
   getch();
   return 1;
}

if ((fp1 = fopen(name1, "w+"))  == NULL){       /* open analog data file
   fprintf(stderr, "\nCannot open analog output file.\n");
   return 1;
}
if ((fp2 = fopen(name2, "w+"))  == NULL){       /* open digital data fil
   fprintf(stderr, "\nCannot open pulse output file.\n");
   return 1;
}

printf("\nInput comments for this file (80 char max): \n");     /* allow
gets(comment);                                                 /* of file a
fprintf(fp1, "%s\n", comment);

printf("\n\nEnter time experiment is to run in minutes:   ");   /* get l
scanf("%d", &minrun);
thisrun = (minrun * 60);


initgraph(&gdriver, &gmode, "");
errorcode = graphresult();      /* assert graphics mode */
   if (errorcode != grOk){  /* an error occurred */
                printf("Graphics error: %s\n", grapherrormsg(errorcode)
                printf("Press any key to halt:");
                getch();
                exit(1);             /* return with error code */
   }
outtextxy(2,0, "Press any key to begin data acquisition");
getch();

setcolor(EGA_LIGHTGRAY);        /* outline graph */
moveto(0,99);
lineto(0,479);  lineto(500,479);        lineto(500,99); lineto(0,99);

setcolor(EGA_DARKGRAY);

/* first the horizontal grid */
moveto(0,137);  lineto(500,137);        moveto(0,175);  lineto(500,175);
moveto(0,213);  lineto(500,213);        moveto(0,251);  lineto(500,251);
moveto(0,289);  lineto(500,289);        moveto(0,327);  lineto(500,327);
moveto(0,365);  lineto(500,365);        moveto(0,403);  lineto(500,403);
moveto(0,441);  lineto(500,441);

/* now the vertical grid */

moveto(50,99);  lineto(50,479);         moveto(100,99); lineto(100,479);
moveto(150,99); lineto(150,479);        moveto(200,99); lineto(200,479);
moveto(250,99); lineto(250,479);        moveto(300,99); lineto(300,479);
moveto(350,99); lineto(350,479);        moveto(400,99); lineto(400,479);
moveto(450,99); lineto(450,479);

/* set up graphics display and text headings for display */

setcolor(EGA_BLACK);
outtextxy(2,0, "Press any key to begin data acquisition");
setcolor(EGA_LIGHTCYAN);
outtextxy(2,85, "ááá O2");

setcolor(EGA_LIGHTMAGENTA);
outtextxy(62,85, "ááá PULSES");

setcolor(EGA_LIGHTRED);
outtextxy(2,0, "Press any key to halt data acquisition.");
setcolor(EGA_WHITE);
outtextxy(2,25, comment);
outtextxy(375,0, "This run is:");
itoa(thisrun, thisstr, 10);
outtextxy(475,0, thisstr);
outtextxy(520,0 , "seconds.");
outtextxy(350,50, "Data will be stored in these files");
outtextxy(350,65, "Oxygen/PH data         Pulse data");
outtextxy(350,80, name1);
outtextxy(540,80, name2);
```

```
init(board);            /* initialize the board */
initializetimer();      /* initialize the timer */
start = readtimer();
lasttime = start;
thistime = 0;

        while(!kbhit()){                /* begin data acquisition loop *

                thistime = readtimer();
                elapsedtime(start, thistime, time_ptr);
                elapsed = *time_ptr;
                ltoa((elapsed/1000.0), btime, 10);
                looptime = (thistime - lasttime);
                lasttime = thistime;
                dindex = dindex + looptime;


                pulse = dda(board);             /* get digital pulse */
                        if(pulse == 1 && lastpulse == 0){       /* check
                                tot++;
                                fprintf(fp2, "%d %2.2f\n", tot, elapsed/
                        }
                lastpulse = pulse;

                mux(channel1,board);    /* select input channel */
                gain(range,board);
                result1 = (adc(board) * 2.4414);        /* get reading c
                mux(channel2,board);    /* select input channel */
                result2 = (adc(board) * 2.4414);        /* get reading c
                tmpresult1 = tmpresult1 + result1;
                tmpresult2 = tmpresult2 + result2;
                index++;

                        if((dindex/1185) >= thisrun){
                                tmpresult1 = tmpresult1/index;  /* compu
                                tmpresult2 = tmpresult2/index;  /* cycle
                                fprintf(fp1, "%2.2f  %2.2f %2.2f\n", (tm

/* plot every other point to xy graph display in real time */

                                if(displa == 2){
                                        setcolor(EGA_LIGHTCYAN);
                                        newx = oldx;
                                        newy = (428 - tmpresult1);

                                        if(newy < 101){
                                                newy = 101;
                                        }
                                        moveto(oldx, oldy);
                                        lineto(newx, newy);
                                        oldx++;
                                        oldy = newy;
                                        setcolor(EGA_LIGHTMAGENTA);
                                        newa = olda;
                                        newb = (479 - (tot/2));
                                        moveto(olda, oldb);
                                        lineto(newa, newb);
                                        olda++;
                                        oldb = newb;

/* print total number of pulses so far  */

                                        setcolor(EGA_BLACK);
                                        outtextxy(105,67, pstr);
                                        itoa(tot, pstr, 10);
                                        setcolor(EGA_LIGHTMAGENTA);
                                        outtextxy(0,67, "Total Pulses: "
                                        outtextxy(105,67, pstr);
```

```
        /* compute ph from mvolt reading and display approx value */

                                            setcolor(EGA_BLACK);
                                            outtextxy(95,50, totstr);
                                            outtextxy(119,50, decstr);

                                            setcolor(EGA_YELLOW);
                                            tmpresult2 = (tmpresult2/510.0);
                                            tmptmpresult = (tmpresult2 * 10.
                                            tmpresult3 = tmptmpresult%10;
                                            itoa(tmpresult3, decstr, 10);
                                            itoa(tmpresult2, totstr, 10);

                                            outtextxy(0,50, "Current PH: ");
                                            outtextxy(95,50, totstr);
                                            outtextxy(110,50, ".");
                                            outtextxy(119,50, decstr);

                                            displa = 1;

                                    }
                                else
                                displa++;
                                tmpresult1 = 0.0;
                                tmpresult2 = 0.0;
                                index = 0;
                                dindex = 0;
                                bindex++;
                                }
                    /* collect an arbitrary number of data points (1000 per NDC) *

                          if(bindex == 1001){
                                  setcolor(EGA_LIGHTGREEN);
                                  outtextxy(510,470, "RUN COMPLETED");

                                   break;

                           }
                  }
        /*  clean up your mess and go home     */
        getch();
        setcolor(EGA_BLACK);
        outtextxy(2,0, "Press any key to halt data acquisition.");
        setcolor(EGA_LIGHTGREEN);
        outtextxy(2,0, "Press any key to exit program.");
        getch();
        restoretimer();
        closegraph();
        fclose(fp1);
        fclose(fp2);
        return 0;

}
```

APPENDIX E

POWER DISTRIBUTION OF CAVITY I IN E-9 SPECTROMETER

EXPERIMENTS

I. No dewar in any cavities

Amplitude	Strong pitch	0.1% Pitch
Cavity I	80	34.5
Cavity II	73.5	31.5

II. Strong pitch in cavity I, 0.1% pitch in cavity II, no dewar in cavity II

Amplitude	Strong pitch	0.1% Pitch
w/ dewar in I	222.4	20.5
w/o dewar in I	80	31.5

III. Strong pitch in cavity I with dewar, 0.1% pitch in cavity II w/o dewar

Amplitude	Strong pitch	0.1% Pitch
w/ sample in II	222.4	20.5
w/o sample in II	212.8	N/A

CALCULATIONS

Power distribution in cavity I

with dewar cavity I, w/o dewar in cavity II.

A. w/ sample in cavity II

$$\text{Power in cavity I (P1)} = \frac{\text{Dial} * 222.4^2}{222.4^2 + (20.5*80/34.5)^2}$$

$$= \text{Dial} * 0.956$$

B. w/o sample in cavity II

$$\text{Power in cavity I (P2)} = \frac{212.8^2 * P1}{222.4^2}$$

$$= 0.915 * 0.956$$

$$= 0.875$$